LOW-NOISE ORGANIC PHOTODIODES WITH NEAR-INFRARED SENSITIVITY

A Dissertation
Presented to
The Academic Faculty

by

Victor Alfonso RODRIGUEZ TORO

In Partial Fulfillment
of the Requirements for the Degree
Doctor of Philosophy
in the
School of Electrical and Computer Engineering

Georgia Institute of Technology
December 2021

LOW-NOISE ORGANIC PHOTODIODES WITH NEAR-INFRARED SENSITIVITY

Approved by:

Dr. Bernard Kippelen, Advisor
School of Electrical and Computer Engineering
Georgia Institute of Technology

Dr. P. Douglas Yoder
School of Electrical and Computer Engineering
Georgia Institute of Technology

Dr. Andrew F. Peterson
School of Electrical and Computer Engineering
Georgia Institute of Technology

Dr. Rosario Gerhardt
School of Materials Science and Engineering
Georgia Institute of Technology

Dr. Juan-Pablo Correa-Baena
School of Materials Science and Engineering
Georgia Institute of Technology

Date Approved: Aug. 27th, 2021

ACKNOWLEDGEMENTS

This work has been finalized because of the immeasurable support of colleagues, friends, and my family. I would like to thank Dr. Bernard Kippelen for his guidance, advice, and patience. His efforts have provided the infrastructure required for the development of my work. I also have learned important life lessons which I believe will be helpful for my professional future.

I would like to acknowledge to Dr. P. Douglas Yoder, Dr. Juan-Pablo Correa-Baena, Dr. Andrew F. Peterson, and Dr. Rosario Gerhardt for taking the time to serve on my committee. I appreciate the feedback they have provided to my research.

My gratitude to all the former and current members of the Kippelen group: Dr. Canek Fuentes-Hernandez for his guidance which helped further develop my scientific skills and for sharing his vision of our field and life; Dr. Vladimir Kolesov for his mentorship (even today) and friendship. Dr. Felipe A. Larrain for being a great friend who taught me how to see things from a very different angle (I have missed, and I will miss our coffee breaks and conversation about life). My gratitude as well to Dr. Silja Abraham, Dr. Michael Gaj, Dr. Talha Khan, Dr. Sangmoo Choi, Dr. Cheng-Yin Wang, Dr. Xiaoqing Zhang, Dr. Wen-Fang Chou, and Dr. Xiaojia Jia. I also want to thank the current members of the Kippelen lab: Oliver Moreno, Gunhee Kim, Youngrak Park, Yi-Chien Chang, and Jingwei Yang for their time, friendship, and support with the many activities that are involved in running the lab. I also want to thank our previous and current administrative staff I had the opportunity to interact with: Tina Mosely, Desta Davison, Dana Foster, and Siri Melkote.

I also want to thank some of the funding agencies and organizations that have made possible my research: Air Force Office of Scientific Research (AFOSR), the Office of Naval Research, the Department of Energy, Fulbright-Colciencias, and LASPAU. I acknowledge many other agencies that provided a legacy of resources (even before my time in the lab) that benefited my work and training.

I would like to thank our School of Electrical and Computer Engineering and all the support I found in the academic office staff: Dr. Daniela Staiculescu (for her endless support and for listening to me during the hard times), Tasha M. Torrence, Andrew Stargill, Shay Robinson, and Olivia Kulisz for their guidance at the different stages of my grad school adventure. I also want to thank former and current graduate chairs of our school: Dr. George Riley, Dr. Benjamin Klein, and Dr. Matthieu R. Bloch for their advice and support; former chairs of the School of Electrical and Computer Engineering: Dr. Steven W. McLaughlin, Dr. Raheem Beyah, and Dr. Magnus Egerstedt for listening to new ideas and showing interest for students' welfare. I also want to thank some of our faculty members: Dr. Thomas K. Gaylord, Dr. Vincent J. Mooney, Dr. Bonnie H. Ferri, Dr. Shimeng Yu, Dr. Timothy J. Brothers, Dr. Azad Naeemi, Dr. John D. Cressler, Dr. Joy Harris, and Dr. Gregory Durgin for many lessons I learned at professional level from our interactions. I have great memories of some of my fellow grad students in the School of Electrical and Computer Engineering during my adventure in grad school: Dr. Sagarika Mukesh, Dr. Divya Prasad, Dr. Abdullah Al-Shehri, Dr. Hommood Alrowais, Patrick S. Golay, Sathish Jayaraman, Ibrahim Khalil, Andrew Tam, Aishwarya Natarajan, and Shruthi Kumar.

At Georgia Tech, I want to thank Center for Engineering Education and Diversity (CEED): Valentina de la Fe, Jackie Cox, Cedric Trice, and Dr. Felicia Benton-Johnson and all the rest of the team; and the Office of Hispanic Initiatives (OHI): Jorge Breton for so many helpful resources I found, especially, during the difficult times. I also want to thank faculty members: Dr. Julian Rimoli, Dr. Patricio Vela, Dr. Francesco Fedele, Analia Rao, and Dr. Daniel Castro-Lacouture for being receptive of new ideas. My gratitude is also with all the past and current members from the Center for Organic Photonics and Electronics (COPE). I have grown as an engineer and a scientist from the interactions within this community and I have also made great friends. Especially, Dr. Ian Pelse and Abigail Advincula. I also have an enormous gratitude with Georgia Tech Alumni who have been always open to have conversations regarding professional paths in Electrical and Computer Engineering. Especially, Greg Hendry and Paul Palonsky.

As my internship was also part of my grad experience, I want to thank Micron Technology for the opportunity learn and work on NAND memories. To the HR team: Jordan Atnip, Lilly Boggan, Jessica Pollard, Melanie Lewis, Dmitry Zhmurkin, Kate Bebee. To members of different technical teams: Falgun Trivedi, Chase Mecham, Shin-Hung Tsai, Sandeep Kadasani, Motao Cao, Monj Monje, Nicholas Clore, Roland Awusie, Che Chen, and Tony Veches. To the STEM team: Cathy Ammirati and Laurie Anderson. It was a great professional experience to have been part of the Micron family.

I also want to thank my colleagues and friends in the US. Specially to Prakash Chourasia, Dr. Andres Caballero, Daniela Estrada, Ana Henriquez, Ingrid Hernandez, Rozhan Tajik, Dr. Lina Mancipe, Juliana Caballero, Dr. Juliana Soto, Dr. Arnoldo Castro, Dr. Diego Dumani, Dr. Ana Maria Estrada, Camilo Pulido, Dr. Adriana Lozoya, Dr.

Camila Apablaza, Dr. Carlos Borca, Dr. John Sherwood, Rachel Sherwood, Rachel Buck, Shiva Bahrami, Yulizza Henao-Barragan, Daniel Martinez, Luis Rosa, Enrique Saurez, Natalia Millan, Lee Pasackow, Dr. Pedro Monje-Arias, and Dr. Francisco Quintero (big thanks!). Your friendship and love have made me feel I was never alone.

I feel gratitude with many mentors I met through professional networks (IEEE, SPIE, OSA, MRS, ACS, SHPE, and NSBE) and academic institutions. In particular, Dr. Fernando Guarin who encouraged me to pursue grad school in the US and at the Georgia Institute of Technology. My big thanks go as well to the LOGRAS, SHPE, the (GT) Salsa community for keeping me healthy, connected, and happy.

También a mis amigos, colegas y a las nuevas generaciones en Colombia. Por ustedes trabajo y me preparo cada día. Especialmente al Dr. José Darío Perea por permitirme trabajar con tantos proyectos en nuestro país. A mis colegas y amigos (cuya lista sería interminable) de las instituciones académicas de las que he hecho parte y he interactuado. A los profesores de UniValle (Dr. Jaime Velasco-Medina, Dr. Julio Cesar Arce), ICESI (Dr. Carlos Arango), UPTC (Dr. Wilson Javier Perez and Dr. Liliana Fernandez), UniAndes (Dr. Alba Ávila) y la Universidad Javeriana (Dr. Andres Jaramillo-Botero), por todo su apoyo, tiempo, orientación, y mentoría a lo largo de varios años.

Finalmente, quiero dedicarle este trabajo a mi familia. A mis padres Luis Enrique Rodriguez Parra y Teresa Toro, mi hermano Luis Fernando Rodriguez Toro, mi sobrina Maria Isabel Rodriguez y mi cuñada Ana Maria Saa. También mis agradecimientos se hacen extensivos a las familias Rodriguez y Toro (tíos, tías, primos y primas). En especial

a Ismael Rodriguez, quien fue un ejemplo a seguir en muchos sentidos y a quien extrañaremos hasta el final de nuestros días.

Thank you all !!!

TABLE OF CONTENTS

LIST OF TABLES

LIST OF FIGURES

LIST OF RELEVANT SYMBOLS AND ABBREVIATIONS

3D	Three dimensions
A	Photoactive Area
Ag	Silver
Au	Gold
Al	Aluminum
AlSb	Aluminum Antimonide
ALD	Atomic Layer Deposition
AZO:PDIN	ZnO nanoparticles:2,9-bis(3-(dimethylamino)propyl)anthra[2,1,9-def:6,5,10-d′e′f′]diisoquinoline-1,3,8,10(2H,9H)-tetraone
B	Bandwidth
Ba	Barium
BCP	2,9-dimethyl-4,7-diphenyl-1,10-phenanthroline
BHJ	Bulk Heterojunction
BL	Bilayer
C	Carbon
C	Capacitance
C_{60}	(C60-Ih)[5,6]fullerene
Ca	Calcium
CB	Chlorobenzene
CCN	Charge-Collection Narrowing
CdSe	Cadmium Selenide
CdTe	Cadmium Telluride
CdTe-QD(s)	Cadmium Telluride Quantum Dot(s)
CH_3	Methyl
CH_4	Methane
CS	Charge-Separated State
CT	Charge-Transfer State
Cu_2S	Copper Sulfide
D^*	Specific Detectivity
DR	Dynamic Range

DC	Direct Current
DCB	1,2-Dichlorobenzene
DIO	1,8-Diiodoctane
DoS	Density of States
DUT	Device under test
E	Energy
E_{B_solid}	Binding Energy in a Solid
E_C	Conduction Band Energy Level
E_F	Fermi Level Energy
E_{fund}	Fundamental gap energy
E_g	Energy Gap Energy
$E_{optical\_solid}$	Optical Bandgap Energy of a Solid
$E_{transport}$	Transport Bandgap Energy
E_V	Valence Band Energy Level
E_{vac}	Energy of Reference for Measurements with the Kelvin Probe
EA	Electron Affinity
EA_{solid}	Electron Affinity of a Solid
ECE	Electron-Collecting Electrode
EQE	External Quantum Efficiency
Φ	Optical Power Density
f_c	Cut-off frequency
f_{mod}	Frequency of Modulation
G_i	Transfer Function between Input Current and Output Current (Frequency Domain)
$G_{i,max}$	Maximum Value of the Transfer Function between Input Current and Output Current (Frequency Domain)
G_{vi}	Transfer Function between Input Current and Output Voltage (Frequency Domain)
G_{max}	Maximum Value of the Transfer Tunction
GaAs	Gallium Arsenide
Ge	Germanium
Ge PD	Germanium Photodiode
H_2O	Water

HCE	Hole-Collecting Electrode
HOMO	Highest Occupied Molecular Orbital
HOPG	Highly Ordered Pyrolytic Graphite
i	Current as a Function of Time
i_{DARK}	Current under Dark Condition as a Function of Time
i_{LIGHT}	Current under Light Condition as a Function of Time
i_{out}	Output Current (Time Domain)
$i_{out,thermal}$	Output Current due to Thermal Noise (Time Domain)
$i_{out,thermal,R}$	Output Current due to Thermal Noise in a Circuit with a Resistor as Front-End Electronics (Time Domain)
i_{PG}	Photogenerated Current as a Function of Time
I_o	Reverse Saturation Current
I_{DARK}	Current under Dark Condition
I_{eq}	Current in Equilibrium
I_{LIGHT}	Photocurrent
I_{LIGHT_SM}	Photocurrent for the Shockley Model
I_{LIGHT_PM}	Photocurrent for the Prince Model
I_{non-eq}	Current in Non-Equilibrium
$\mathcal{I}_{in}$	Input Current (Frequency Domain)
$\mathcal{I}_{out}$	Output Current (Frequency Domain)
I_{ph}	Photogenerated Current
I_{PG}	Photogenerated Current after Parasitic Effects
I_{rms}	Measured RMS Noise Current
$I_{rms,dark}$	Measured RMS Noise Current under Dark Condition
$I_{rms,light}$	Measured RMS Noise Current under Light Condition
$I_{rms,pg}$	Measured RMS Noise Current Associated to the Photogenerated Current Density after Parasitic Effects
$I_{rms,shot,}$	Shot RMS Noise Current
$I_{rms,shot,dark\_SM}$	Shot RMS Noise Current under Dark Condition in the Shockley Model
$I_{rms,shot,light\_PM}$	Shot RMS Noise Current under Light Condition in the Prince Model
$I_{rms,thermal,}$	Thermal RMS Noise Current
$I_{rms,white,}$	White RMS Noise Current

ICBA	Indene-C_{60} Bisadduct
IE	Ionization Energy
IE_{solid}	Ionization Energy in a Solid
InP	Indium Phosphide
IPD(s)	Inorganic Photodiodes(s)
IPES	Inverse Photoemission Spectroscopy
ITO	Indium Tin Oxide
j	Complex Unit
J	Current Density
J_0	Reverse Saturation Current Density
J_{DARK}	Current Density under Dark Condition
J_{DARK_SM}	Current Density under Dark Condition in the Shockley Model
J_{LIGHT}	Photocurrent Density
J_{LIGHT_PM}	Photocurrent Density in the Prince Model
J_{LIGHT_SM}	Photocurrent Density in the Shockley Model
J_{ph}	Photogenerated Current Density before Parasitic Effects
J_{SC}	Short Circuit Current Density
k	Boltzmann Constant
KP	Kelvin Probe
LiF	Lithium Fluoride
LASER	Light Amplification by Stimulated Emission of Radiation
LDR	Linear Dynamic Range
LED	Light Emitting Diode
MoO_3	Molybdenum Trioxide
MoO_x	Molybdenum Oxide
MHP PD	Metal-Halide Perovskites Photodiode
n	Ideality Factor
N_2	Nitrogen
ND(4)	Neutral Density (4 is the attenuation)
NEP	Noise Equivalent Power
NIR	Near-Infrared
N_{ph}	Photon Flux Density

NW(s)	Nanowire(s)
O	Oxygen
OH	Hydroxyl
OPV	Organic Photovoltaic
OPD(s)	Organic Photodiode(s)
OSC(s)	Organic Solar Cell(s)
P.M.	Prince Model
PAL	Photoactive Layer
P3HT	Poly(3-hexylthiophene-2,5-diyl)
PCBM	Phenyl-C61-butyric acid methyl ester
$PC_{71}BM$	[6,6]-Phenyl-C71-butyric acid methyl ester
PCE	Power Conversion Efficiency
PCE10, PTB7-Th, PBDTTT-EFT or PBDTT-FTTE	Poly[4,8-bis(5-(2-ethylhexyl)thiophen-2-yl)benzo[1,2-b;4,5-b']dithiophene-2,6-diyl-alt-(4-(2-ethylhexyl)-3-fluorothieno[3,4-b]thiophene-)-2-carboxylate-2-6-diyl))
PEDOT:PSS	Poly(3,4-ethylenedioxythiophene) polystyrene sulfonate
PEIE	Polyethylenimine Ethoxylated
PFBT	2,3,4,5,6-pentafluorothiophenol
PFN	poly[(9,9-bis(3′-(N,Ndimethylamino)propyl)-2,7-fluorene)-alt-2,7-(9,9-dioctylfluorene)]
PFN-Ox	Poly[(9,9-bis(60-(N,N-dimethylamino)-propyl)-2,7-fluorene)-alt-2,7-(9,9-bis(3-ethyl(oxetane-3-ethyloxy)-hexyl)fluorene)]
PVK	poly(N -vinyl-carbazole)
PPy	Polypyrrole
P_{opt}	Optical Input Power
PV	Photovoltaics
q	Fundamental Electric Charge
Q	Charge Stored
$\Re$	Responsivity
RMS	Root-Mean-Square
R_Ω	Resistance in Calculation of Thermal Noise
R_P	Shunt Resistance
R_S	Series Resistance

S.M.	Shockley Model
S1133	A type of Silicon Photodiode with an Optical Filter (Responsivity in the Visible Range)
S2386-44K	A type of Silicon Photodiode
S_0	Ground State
S_1	Singlet Excited State
Si	Silicon
S_{i_in}	Spectral Noise Power Density for an Input` Current
$S_{i,others}$	Spectral Noise Power Density for Current due to Other Noise Sources
$S_{i,thermal}$	Spectral Noise Power Density for Current due to Thermal Noise
$S_{i,shot}$	Spectral Noise Power Density for Current due to Shot Noise
$S_{i,shot,dark\_SM}$	Spectral Noise Power Density for Current due to Shot Noise under Dark Condition in the Shockley Model
$S_{i,shot,dark\_PM}$	Spectral Noise Power Density for Current due to Shot Noise under Dark Condition in the Prince Model
$S_{i,shot,light}$	Spectral Noise Power Density for Current due to Shot Noise under Illumination Condition
$S_{i,shot,light\_SM}$	Spectral Noise Power Density for Current due to Shot Noise under Illumination in the Shockley Model
$S_{i,shot,light\_PM}$	Spectral Noise Power Density for Current due to Shot Noise under Illumination in the Prince Model
S_{v_in}	Spectral Noise Power Density of an Input Voltage in a Coupling Circuit
S_{v_out}	Spectral Noise Power Density of an Output Voltage in a Coupling Circuit
Si PD	Silicon Photodiode
SnO_2	Tin (Di)Oxide
$SNR_{current}$	Signal-to-noise Ratio for Current
SNR_{power}	Signal-to-noise Ratio for Power
SMU	Source monitor/measurement unit
T	Temperature
T_x	Optical Transmission
t	Time
TFB	poly(9,9-dioctylfluorene-alt-N-(4-butylphenyl)-diphenylamine)

TMA	Trimethylaluminum
UV	Ultraviolet
V	External Applied Voltage
V_{CPD}	Contact Potential Different
V_{BIAS}	External Voltage Applied in Kelvin Probe Measurements
V_{in}	Input Voltage (Frequency Domain)
V_{OC}	Open Circuit Voltage
v_{out}	Output Voltage (Time Domain)
$v_{out,thermal,R}$	Output Voltage due to Thermal Noise in a Circuit with a Resistor as Front-End Electronics (Time Domain)
$v_{out,thermal,RC}$	Output Voltage due to Thermal Noise in a Circuit with an RC Circuit as Front-End Electronics (Time Domain)
V_{out}	Output Voltage (Frequency Domain)
V_T	Thermal Voltage
Vis-NIR	Visible and Near-Infrared
ω	Angular Frequency
WF	Work Function
WF_{ECE}	Work Function of the Electron-Collecting Electrode
WF_H	High Work Function Value
WF_{HCE}	Work Function of the Hole-Collecting Electrode
WF_L	Low Work Function Value
WF_{sample}	Work Function of the Sample of a Kelvin Probe
WF_{tip}	Work Function of the Tip of a Kelvin Probe
ZnO	Zinc Oxide
λ	Wavelength

SUMMARY

The objective of this dissertation is to create and develop approaches for the fabrication of organic photodiodes (OPDs) with near-infrared (NIR) response. This is achieved by (i) using organic materials as the absorber or photoactive layer (PAL) of organic solar cells (OSCs) with high power conversion efficiencies (*PCE > 10%*) and that have NIR responsivity; and (ii) implementing two fabrication approaches which reduce the noise of OPDs.

The materials used in the absorber or PAL for both fabrication approaches are the polymer PCE10, which acts as an electron donor, and the fullerene $PC_{71}BM$, which acts as an electron acceptor. The absorber or PAL is sandwiched between two different electrodes whose work function (WF) difference is 1.3 eV, enabling the asymmetry required in the OPDs for the extraction of carriers.

In the first approach, the PAL thickness is tuned to reduce the electronic noise. Two specific PAL thicknesses (700 nm and 1150 nm) are studied in depth. OPDs with these thicknesses reach low root-mean-square (RMS) noise current values in the order of tens of fA at a bandwidth B = 1.5 Hz. However, the sensitivity of the OPDs with PAL thickness of 700 nm is observed to be broadband, in contrast to OPDs with PAL thickness of 1150 nm, whose sensitivity is more narrowband. Some relevant reverse bias conditions are evaluated to measure the impact of an external bias in the responsivity and the noise, and simulations using an equivalent circuit are presented to understand the different contributions to the electronic noise. The noise equivalent power (*NEP*) and the specific detectivity (D^*) are measured and benchmarked to literature values for other OPDs.

Procedures to evaluate these properties are contrasted with typical assumptions made in the literature.

In the second approach, the thickness of the PAL is reduced to 170 nm. For this thinner layer, it is observed that the RMS noise current values can be in the order hundreds of fA (B = 1.5 Hz). Then, it is proposed that, for the same PAL thickness, the RMS noise currents can be reduced to tens of fA (B = 1.5 Hz) through a passivation process of the interface between the PAL and the hole-collecting electrode (HCE) based on atomic layer deposition (ALD) using the trimethylaluminum and water precursors. This passivation is done at 75 °C making it compatible with materials that require processing at low temperatures (e.g., < 100 °C) to avoid degradation of the materials and/or change of their morphology. The passivated thin OPDs (PAL thicknesses of 170 nm) have higher responsivity values with respect to values reached in the first approach using OPDs with thicker PALs (PAL thicknesses of 700 nm and 1150 nm). As before, relevant bias conditions are evaluated, and the *NEP* and D^* are measured considering the measured RMS noise current values and the light-intensity dependence of the responsivity.

Finally, we discuss how the proposed novel approaches might be easily applied to other organic-based optoelectronic devices for better detection, especially for applications in which certain properties of organic materials, such as semitransparency, large photodetection area, and processing at low temperature values are desirable or required.

CHAPTER 1. INTRODUCTION

1.1 Photodetectors: Definition and Market Segments for Sensing and Imaging

Photodetectors or optical sensors transform the optical power of a detectable/measurable signal into a voltage or a current signa. Such devices are used in various market segments such as defense and aerospace, industrial, medical, automotive, and mobile and consumer electronics. The usage of photodetectors is expected to grow in the upcoming years driven mainly by the automotive and mobile and consumer electronics segments. **Figure 1** illustrates the projected growth in 2025 specifically for 3D imaging and sensing applications.

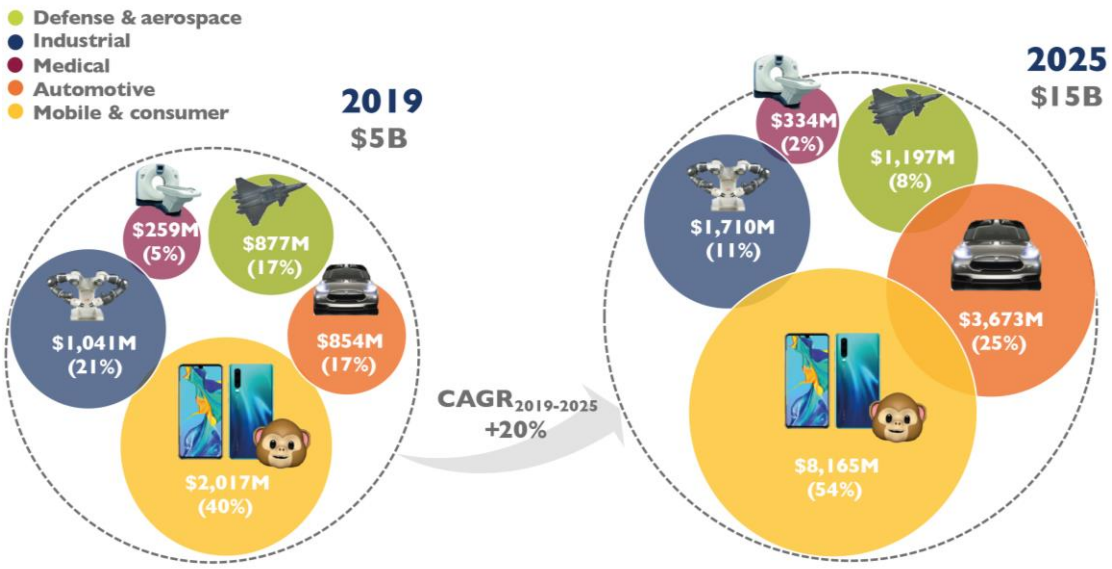

Figure 1. 3D imaging and sensing forecast (2019 – 2025). Source: 3D imaging and sensing 2020 report. Yole Developpement, 2020.

The successful deployment of photodetectors in these market segments as well as their inclusion in new applications will depend to a large extent on attaining affordable costs, improving their detection capabilities (e.g., tunability, detection area size, etc.), and enabling new physical features (e.g., flexibility, semi-transparency, conformability, etc.). Next-generation materials (e.g., polymers, fullerenes, perovskites, nanocrystals, quantum dots, etc.) might help meet these expectations and needs once integrated in devices, extending the current capabilities of photodetectors based on traditional inorganic materials.

1.2 Devices for Photodetection: Contrast of Some Commercial Technologies

Photodetectors can be roughly classified depending on their constituting materials (i.e., inorganic, organic, hybrid, etc.), which defines their region of detection in the electromagnetic spectrum (i.e., X-ray, ultraviolet, visible, infrared, microwave, etc.) and optical selectivity (i.e., narrowband or broadband), among other features. The mixture of materials and their interactions combined through various layer architectures and processing conditions yield different types of photodetector devices.

The selection of photodetectors depends on intrinsic factors such as the spectral response, the limit of detection, and the response time; market factors such as the price; design aspects such as the size; and operation conditions such as the temperature sensitivity, external voltage supply availability, and mechanical robustness. A summary of some commercially available inorganic photodetectors, which use photocurrent as a typical output signal to measure optical power, is shown in **Table 1**.

Table 1. Stand-alone traditional photodetectors commercially available. Adapted from [1-3].

	Photomultipliers	**Silicon Photomultipliers**	**Avalanche Photodiodes**	**Photodiodes**	**Photo transistors**
Price (stand-alone)	$$$$	$$$	$$	$	N/A
Readout Circuit	Simple	Simple	Complex	Complex	Complex
Spectral coverage (nm)	115-1700	320-900	190-1700	190-13000	400-1100
Gain	Yes	Yes	Yes	No	Yes
Response Time	Very Fast	Very Fast	Fast	Slow	Fast
Bias Voltage	~1000 V	~50 V	~200 V	-	N/A
Large active area	Yes	Scalable	No	No	No
Compact	No	Yes	Yes	Yes	Yes
Temperature Sensitivity	Low	Medium	High	Low	Low
Ambient light immunity	No	Yes	Yes	Yes	Yes
Magnetic resist	No	Yes	Yes	Yes	Yes
Mechanical Robustness	Good	Rugged	Rugged	Rugged	Rugged

The most affordable photodetector is the photodiode, which is a two-terminal device whose current-voltage (*I*-*V*) characteristic can be approximately quantified with the Prince diode equation (Shockley equation with parasitic effects). For this work, photodiodes will be the main reference type of photodetector.

1.3 Photodiodes: Some Current and Next-Generation Materials

Typical photodiodes with detection capabilities in the visible and the near-infrared region of the electromagnetic spectrum are based on inorganic materials, such as silicon (Si) and Germanium (Ge). Among these inorganic photodiodes (IPDs), Si IPDs are often preferred because of their spectral coverage in the visible and the near-infrared (cut-off wavelength around 1100 nm), their high detectivity (metric to quantify the ability of a photodetector to distinguish the signal from the noise), and their compatibility with existing Si-based industries (i.e., Silicon photonics).

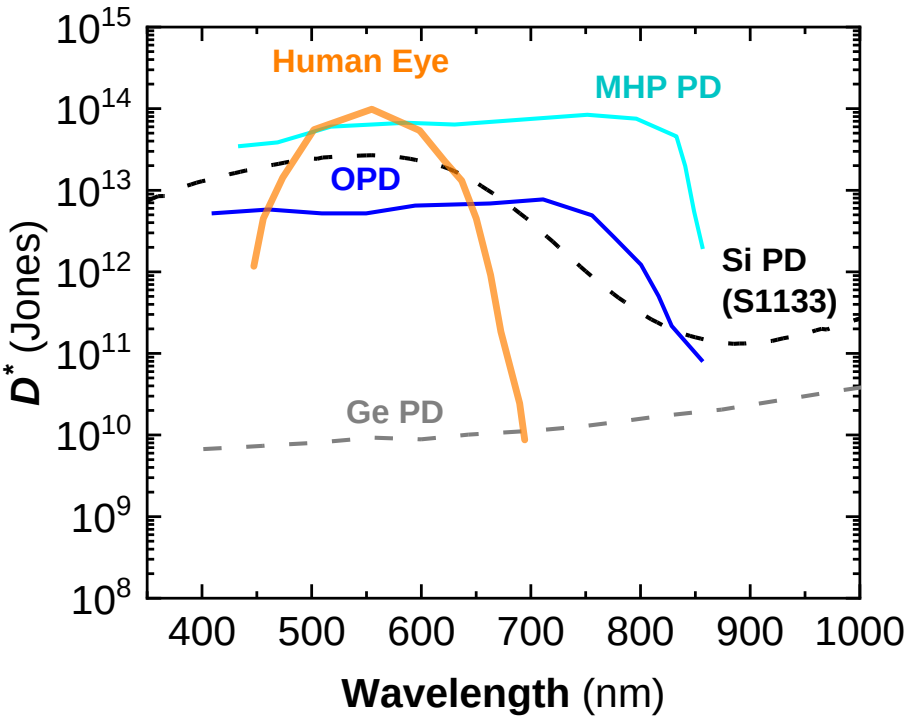

Figure 2. Detectivity values. Adapted from [4].

Despite Si IPDs being low-cost compared to other photodetector technologies, their processing characteristics (e.g., high temperatures, expensive clean room infrastructure, etc.) might scale up rapidly their costs, hindering their ubiquitous usage. Furthermore, the performance of an IPD is affected when its active area is increased because of defects produced during its fabrication and processing.

In contrast, materials processed from solution such as quantum dots, metal halide perovskites, nanocrystals, and organic (carbon-based) materials, have emerged as an alternative to those based on inorganic materials (see **Figure 2**): Photodiodes with comparable detectivity values in the visible (organic photodiodes) and the near-infrared (perovskites) region of the electromagnetic spectrum have been reported (see **Figure 2**). Some of the advantages of photodiodes processed from solution are their low-temperature processability (compatible with flexible substrates) and their compatibility with a variety of affordable methods (roll-to-roll, spray, inkjet printing, etc.) for large-area deposition with arbitrary shapes. All these processing characteristics imply a reduction of costs for photodiodes processed from solution, suggesting their usage in ubiquitous sensing.

1.4 Organic Photodiodes (OPDs) – Review of Essentials

Organic photodiodes (OPDs) are based on organic materials which consist of diverse types of low-dimension π-conjugated structures (e.g., molecules, polymers, fullerenes, etc.) that permits the electronic transport despite their lack of crystallinity. OPDs contain the following three layers: 1) an absorber or a photoactive layer (PAL), 2) an electron-

collecting electrode (ECE), and 3) a hole-collecting electrode (HCE) as shown in **Figure 3**.

OPDs can be classified according to their photoactive layer (PAL), electron-collecting electrode (ECE), hole-collecting electrode (HCE) properties as follows:

- PAL spectral sensitivity: Panchromatic (broadband) or selectively tuned for specific frequencies (narrowband)
- PAL chemical composition: Unary, binary, ternary, etc.
- PAL deposition method: Vacuum-processed PAL or solution-processed PAL (e.g., ink-jet printing, blade coating, spray coating, drop casting, etc.)
- PAL constituting materials: Small molecules (e.g., fullerenes or non-fullerene molecules), polymers, and crystals. Hybrid mixtures with inorganic materials as sensitizers (low concentrations in the PAL) are also found in the literature
- PAL junction type: Bi-layer (BL) or planar heterojunction, multi-layer or tandem, co-deposited, or bulk heterojunction (BHJ)
- Device architecture: Conventional (targeted light entering from the HCE) or inverted (targeted light entering from the ECE)

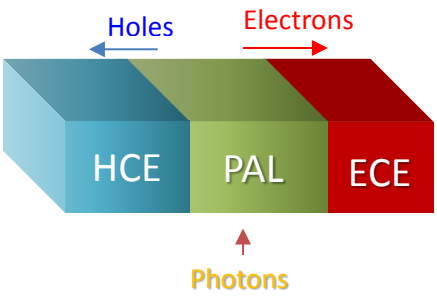

Figure 3. General parts of an OPD. HCE: Hole-collecting electrode. PAL: Photoactive layer. ECE: Electron-collecting electrode.

Recently, the Kippelen group at Georgia Tech has shown that photodiodes based on organic materials such as the polymer P3HT and the fullerene ICBA can attain performance metrics comparable to Si IPDs in the visible, except for the response time [5]. Furthermore, when the area of the PAL is increased, detection capabilities of OPDs are preserved. In contrast, Si IPDs drastically reduce their detection capabilities because increment in area is detrimental to the performance. Despite these desirable characteristics of OPDs, the P3HT:ICBA OPD only has response in the visible range limiting their potential applications of photodiodes in other regions like the near-infrared region.

The near-infrared (NIR) region (wavelengths from 700 nm to 1100 nm) is of special interest because of its potential impact in biomedical fields, short-distance communications, and night vision. Wavelengths between 800 nm and 900 nm present the lowest attenuation of electromagnetic signals.

1.5 Thesis Objectives

This work builds on the recent results of P3HT:ICBA OPDs [5]. In order to extend the sensitivity of OPDs based on polymer and fullerene materials to NIR response (i.e., beyond 700 nm), novel materials and processing techniques are explored and formulated. Specifically, the main objectives of this dissertation are listed as follows:

- Optimize the photoactive layer thickness of OPDs, targeting the minimization of noise in the device under dark condition and the maximization of the detectivity (D^*)
- Implement a passivation method at low temperatures based on atomic layer deposition (ALD) for OPDs with thin photoactive layer thicknesses, targeting the minimization of noise in the device under dark condition and the maximization of the detectivity (D^*)
- Contrast the detectivity of the different approaches with state-of-the-art OPDs

1.6 Thesis Structure

This Ph.D. dissertation is organized as follows: **Chapter 2** presents the literature review and background on photodetectors and photodiodes. Specifically, the working principles of inorganic photodiodes (IPDs) and organic photodiodes (OPDs) are introduced and compared. A literature survey is also presented on state-of-the-art OPDs with near-infrared response at commercial and lab scale (special selection on OPDs based on the

polymer PCE10 and fullerene $PC_{71}BM$, which are the materials used for the devices in this dissertation). Energetic aspects involved in OPDs at materials level for the photoactive layer (PAL), electron-collecting electrode (ECE), hole-collecting electrode (HCE), and their respective interfaces are also discussed. The energetic aspects at the device level are also described through a simple model. Then, a description of OPDs using an equivalent circuit model is introduced by defining their key quantities and metrics. The model of the equivalent circuit (Prince model) for OPDs is also discussed and related to the noise in OPDs.

Chapter 3 presents the methods for the fabrication and characterization of OPDs based on the PCE10:$PC_{71}BM$ absorber or PAL. First, equipment, principle of operations, and procedures used for the characterization of materials are described. Some of the experimental setups and/or equipment are spectroscopic ellipsometry, profilometry, and Kelvin probe measurements. Second, the process to fabricate organic photodiodes (OPDs) is described. Details on the deposition and growth of the electrodes (ECE) and the absorber (PAL) are described as well as the passivation based on atomic layer deposition (ALD). Finally, the different in-house characterization stations used to measure the performance of OPDs are presented, including measurement of electric characteristic curves, responsivity as a function of wavelength, and light intensity experiments.

Chapter 4 presents simulation results for OPDs based on an equivalent circuit and two approaches to achieve OPDs with low noise and NIR sensitivity. The first one is based on the thickness adjustment of the PAL, which produces narrow-band OPDs. The second approach is based on the passivation of the PAL of OPDs through atomic layer deposition.

In both cases, measured noise is comparable to state-of-the-art OPDs with sensitivity in the visible region.

Chapter 5 presents conclusions achieved through this dissertation and future steps to take for capitalizing on this research.

CHAPTER 2. BACKGROUND

This chapter is divided into four sections. **Section 2.1** contrasts the working principle of inorganic photodiodes (IPDs) to the working principle of organic photodiodes (OPDs). **Section 2.2** presents a review of state-of-the-art OPDs with near-infrared response at commercial and lab scales. Materials used in OPDs relevant for this research are highlighted as well as devices' performance. **Section 2.3** summarizes aspects of the physics of OPDs at the materials level with an emphasis on the materials' energetics. The energetics of the parts that form OPDs, namely, the absorber (PAL) and the electrodes (ECE and HCE) as well as their interfaces are presented. Changes in the description of the electronic properties of atoms, molecules, and solid-state thin films are summarized and the energetics involved in devices introduced in the final part of this section. **Section 2.4** presents the definitions of the electrical signals associated to OPDs, some relevant performance metrics, and the equivalent circuit model used in this research. The relation of this circuit with the types of noise in OPDs is also discussed with the mathematical formalism that enables to describe changes in noise after its interaction with coupling or front-end electronics.

2.1 Introduction to Photodiodes: Contrasting Aspects between Inorganic Photodiodes (IPDs) and Organic Photodiodes (OPDs)

In optical sensing, a typical inorganic photodiode (IPD) consists of a p-n junction. When the device is exposed to a light signal, the absorbed photons create weakly bound electron-hole pairs which are easily dissociated into free carriers due to thermal energy

room temperature. Free carriers are routed in a specific direction due to the internal asymmetry produced by p-n junction. Holes produced by the absorption of photons are transported towards the p-doped side of the junction, while electrons are transported towards the n-doped region. The transport of charges leads to a photocurrent, while the accumulation of extra carriers in the spatially separated p-doped and n-doped regions leads to a photovoltage. In the absence of external light, under steady-state conditions an average current may flow through the device under reverse bias because carriers can be generated thermally. In an ideal diode, the latter is called the reverse saturation current.

In OPDs, the internal asymmetry is generated differently than in IPDs. In OPDs, the asymmetry is generated by the difference in work function (WF) values of the electrodes or the charge collection layers that are in contact with the opposite sides of the PAL.

In both types of devices, it is critical that the carrier diffusion length is larger than the thickness of the PAL to extract carriers efficiently before they recombine. The thickness of the PAL is generally chosen to be thick enough to absorb the incident light efficiently. OPDs are comprised of semiconductors that have charge mobility values that are lower than those used in IPDs, reducing the carrier diffusion length. However, the higher absorption coefficients of organic semiconductors allow for the fabrication of OPDs with PAL layers with a thickness still larger than the carrier diffusion lengths, despite the lower diffusion length values.

Another feature that makes OPDs different from IPDs is the strength of the Coulomb interaction of the bound electron-hole pairs or excitons. In an organic semiconductor, within the Bohr model for an exciton, the binding energy in the electron-hole pair is larger

than the thermal energy at room temperature (26 meV), leading to bound electron-hole pairs or stable exciton that are likely to recombine before they dissociate into free carriers and can contribute to the generation of current. Therefore, dissociation of the exciton is essential for the correct operation of OPDs. An additional driving force needed to dissociate photogenerated excitons (bound electron-hole pairs) can be provided through the interaction of two different organic semiconductors with different frontier orbitals. Organic semiconductors can be designed to be either π–electron rich (or donor-like) or π–electron deficient (or acceptor-like). When such materials are put in contact, their electronic coupling leads to the formation of a weak charge-transfer complex (CT complex) that provides an efficient way for exciton dissociation. At these interfaces, the excitons dissociate efficiently with the electron being transferred to the most electron deficient material (acceptor) and the hole transferred to the most electron rich material (donor). These interfaces can be created in a device by having a multilayer architecture with layers of donor-like materials and acceptor-like materials, or by blending two or more such organic semiconductors to form what the community refers to as a bulk heterojunction (donor:acceptor).

Note, that the exact description of the dissociation of excitons still remains a subject of ongoing studies [6], but the process can divided into the following steps 1) the formation of the exciton (optical transition) in an organic semiconductor, 2) the formation of the charge-transfer (CT) state at the donor/acceptor interface, and 3) the formation of the charge-separation state (CS state), where the electron becomes a free charge in the acceptor material, and the hole becomes a free charge in the donor material, 4) the extraction and collection of carriers by the electrodes.

2.1.1 General Design Aspects of Near-Infrared (NIR) IPDs – Qualitative Description

In the design of NIR IPDs, an optical bandgap of at least 1.12 eV (1100 nm) and at most 1.77 eV (700 nm) is required for the absorber. Examples of these bulk absorbers are the unary silicon or Si (1.12 eV, 1100 nm), and the binary copper sulfide or Cu_2S (1.2 eV, 1033 nm), indium phosphide or InP (1.34 eV, 925 nm), gallium arsenide or GaAs (1.42 eV, 873 nm), cadmium telluride or CdTe (1.5 eV, 827 nm), and aluminum antimonide or AlSb (1.6 eV, 775 nm). Other absorbers are based on nanostructures (quantum dots) of binary compositions such as cadmium selenide or CdSe (1.74 eV, 713 nm) and bulk binary, ternary, and quaternary semiconductor alloys.

Once the material with the desired NIR optical bandgap has been selected for the absorber, IPDs are designed by stacking heterojunctions (when the lattice constant enables it) or homojunctions with different levels of doping (e.g., Si P-N junction). The design is constrained by the doping trade-off between the response time of the IPDs (achieved by wide depletion regions and then high doping levels) and the tolerable noise levels (as dopants become points of scattering for carrier transport) for a specific application.

Since the asymmetry p-n junction devices is induced by regions with a different type of electrical doping, electrodes in IPDs are not required to have different WF values, and they can be from the same conductive material (e.g., aluminum a.k.a. Al). Electrodes are typically passivated by thin dielectrics such as silicon oxide or SiO_2, and high doping levels are present in the absorber close to the interface. The passivation and doping enable (quasi) ohmic contacts for transferring free carriers between the absorber and the electrodes with a reduced electrical power dissipation.

2.1.2 General Design Aspects of NIR OPDs – Qualitative Description

In the initial stage of the design of OPDs, one considers four energetic properties when selecting the materials from which the device will be fabricated. The first one is the optical bandgap of the PAL, which enables the absorption of NIR photons by the donor material, the acceptor material, or both, for proper detection of the optical signal. The second property impacts the dissociation of the exciton and relates to the difference in energy of the frontier orbitals between the donor and acceptor materials that form the PAL. The third relevant energetic property relates to the disorder and the distribution of frontier orbitals within each material as it impacts charge transport. The fourth property relates to the work function of the electrodes and their relative value compared with the frontier orbitals of the D and A materials. These values impact the required asymmetry in the device as well as the extraction of the photogenerated carriers. All the relevant energetic aspects will be discussed in detail in **Section 2.3**.

2.2 Literature Survey on Organic Photodiodes (OPDs) with Near-Infrared Response

This section compiles and classifies state-of-the-art OPDs that have been reported along with various of their performance metrics. First, a summary is presented of companies that have commercialized OPDs in the past and/or that are offering OPD products and solutions currently. Second, state-of-the-art NIR OPDs based on polymer:fullerene materials at a lab scale are summarized and highlights on the main strategies to attain high performance are discussed.

2.2.1 OPDs with NIR Response at Commercial Level: Companies, Products and Solutions

During the last decade, various companies have taken advantage of the properties of organic materials (e.g., large area, flexibility, thin thickness, etc.) for photodetection purposes. Some of the efforts have been developed at research and development levels in large companies which do not offer necessarily commercial products and/or solutions based on OPD. However, it is possible to find companies, some of them startups, which offer photodetection solutions based on OPDs in applications in which inorganic materials properties are limiting.

A summary of some of the past and current efforts in the commercialization of OPD, their fields of application and the intended specific solutions are presented in **Table 2.** Although the specific materials (e.g., type of polymer or small molecule) used by these companies are not disclosed, this summary is presented to provide evidence of the potential of OPDs as a commercial alternative in photodetection.

Table 2. Examples of commercially available applications and solutions based on OPDs

Company (Partner)	Location (Year)	Application	Solutions	Ref.
Isorg	France (2010)	• Smartphones and wearables • Access control • Border control • Automatic inventory management • Touchless display • Xray image sensor	• Fingerprint sensor on display • Biometrics – fingerprint • Smart logistics	[7]
Flexenable	England (2015)	• Smartphones and wearables • Access control	• Optical fingerprint sensors	[8]
NikkoIA (Siemens)	France (2011)	• Medical interfaces • Security interfaces • Interactive interfaces	• Visible and NIR photodetectors • Image sensors	[9]
Orthogonal	USA (2009)	• Smartphones and wearables	• Fingerprint sensor	[10]

2.2.2 State-of-the-Art OPDs with NIR Response at Lab Scale

While the materials used in OPDs at a commercial level are not fully disclosed, OPDs with NIR response at lab scale are characterized by PALs that use a vast variety of materials as evidenced from research articles (see **Table 3**). Only a few of the donor and acceptor organic materials used in the PAL of OPDs are available from chemical manufacturers, complicating their usage when capabilities in chemical synthesis are limited. This lack of wide access to donor and acceptor materials prevents further optimization of NIR OPDs with high detectivities.

2.2.2.1 Scope of the Literature Survey of OPDs with NIR Response at Lab Scale

Table 3 presents a chronological list of NIR OPDs with panchromatic (broadband) spectral sensitivity and a binary composition (donor:acceptor = polymer:fullerene) in the PAL. **Table 3** is divided into two main parts: OPDs' fabrication highlights and performance.

In the OPDs' fabrication highlights in **Table 3**, it is noted that selected OPDs summarizes the PAL materials which are combined in a BHJ or bilayer (BL) configuration and processed from solution (PAL deposition through spin coating, spray coating, etc.). Details of the architecture (i.e., electrodes and interlayers) and the thickness and thermal annealing for PAL used are specified for each OPD.

In the OPDs' performance part in **Table 3**, three performance metrics have been selected for comparison purposes: The responsivity $\Re$, the noise equivalent power (*NEP*), and the specific detectivity (D^*). $\Re$ is the metric that quantifies the photogenerated current density by the OPD for a given optical power density Φ. The sub index for $\Re$ represents the external quantum efficiency (*EQE*). When *EQE* = 100%, a photon generates an electron (hole) that is extracted from the PAL and collected at the ECE (HCE) and then $\Re_{100\%}$. At a specific wavelength λ, it is desirable to maximize $\Re$ for high-performance OPDs. *NEP* and D^* are discussed next.

Table 3. Polymer:Fullerene NIR OPDs. Adapted from [11-13].

FABRICATION HIGHLIGHTS					PERFORMANCE			REF
PAL (Deposition Method)	**Architecture ECE HCE**	**Thick-ness (nm)**	**Thermal Annealing**		**Spectral Region (nm)**	**$\Re$ (A/W) V (V) λ (nm)**	***NEP* (W or W/Hz$^{-1/2}$) *D** (Jones) f_{mod} & *B* (Hz)**	
			T **(°C)**	***t*** **(min)**				
PTT: PCBM (Spin Coating)	Conventional Ca ITO/PEDOT	100	-	-	400-970	$\Re_{38\%}$= 0.26 -5 850	1.35*10^{-11} - 4*10^{3} & -	[14] 2007
LBPP-1: PCBM (Spin Coating)	Conventional LiF/Al ITO/PEDOT	100	-	-	300-1200	$\Re_{10\%}$= 0.08 0 950	2*10^{-19} - - & -	[15] 2007
PDDTT: PCBM (Spin Coating)	Conventional Al ITO/PEDOT	150	-	-	300-1450	- -0.1 800	- 2.3*10^{13} - & -	[16] 2009
	Inverted ITO/ZnO-NWs MoO_3/Au	150	80	10	400-1450	$\Re_{27\%}$= 0.18 0 800	- 2*10^{11} - & -	[17] 2012
PDTTP: PCBM (Drop Casting)	Conventional Ca/Al ITO/PEDOT	320	-	-	400-1100	$\Re_{50\%}$= 0.32 -5 800	- - 10^{6} & 4*10^{6}	[18] 2011
P4: PCBM (Spin Coating)	Conventional Al ITO/PEDOT	-	150	20	400-1000	$\Re_{12\%}$= 0.07 -4 750	- 2*10^{10} - & -	[19] 2012
PCPDTBT: PCBM (Spin Coating)	Conventional Ca/Al ITO/CdTe-QDs	200	70	10	350-900	$\Re_{25\%}$= 0.14 -0.5 700	- 1*10^{11} - & -	[20] 2012
	Inverted ITO/ZnO MoO_3/Ag	200	100	10	400-850	$\Re_{37\%}$= 0.24 -0.5 800	- 2.5*10^{12} - & -	[21] 2013
PCPDTBT: PCBM (Spray Coating)	Conventional Ca/Ag ITO/PEDOT	500	140	5	400-1000	$\Re_{45\%}$= 0.27 -5 750	- - 170 Hz & -	[22] 2013
PBDTTT-C: $PC_{71}BM$ (Spin Coating)	Inverted ITO/PEIE PEDOT/Ag	280	100	2	300-800	$\Re_{30\%}$= 0.17 -2 700	- 10^{13} - & 12*10^{3}	[23] 2013
PTZBTTT-BDT: PCBM (Spin Coating)	Conventional PFN-OX/Al PEDOT/ MoO_3	70	-	-	400-1100	$\Re_{16\%}$= 0.10 0 800	- 1.75*10^{13} - & -	[24] 2013
	Inverted ITO/PFN MoO_3/Ag	70	-	-	350-1100	$\Re_{18\%}$= 0.12 0 800	- 10^{13} - & -	[25] 2014
DDTT(P4): $PC_{61}BM$ (Spin Coating)	Conventional BCP/Al ITO/PEDOT	120	-	-	400-1200	$\Re_{\%}$= 0.06 -0.1 800	- 1.4*10^{12} 160 & -	[26] 2014
PBD(EDOT): $PC_{71}BM$ (-)	Conventional PFN/Al ITO/PEDOT	100	-	-	400-900	$\Re_{30\%}$= 0.19 -0.2 800	1.1*10^{-13} 8*10^{12} 100 Hz & -	[27] 2015
P1: PCBM (Spin Coating)	Conventional BCP/Al ITO/PEDOT	190	-	-	300-1000	$\Re_{25\%}$= 0.16 -0.1 800	- 1.4*10^{13} 25 Hz & -	[28] 2015
PCE10: $PC_{71}BM$ (Spin Coating)	*Conventional Al ITO/PEDOT*	*290*	-	-	*300-800*	$\Re_{51\%}$= *0.31* *-10* *750*	- *8.6*10^{11}* - & -	*[29] 2015*
Table Continues in Next Page								

PDTP-DFBT: $PC_{71}BM$ (Drop Casting)	Inverted ITO/SnO_2/PEIE MoO_3/Ag	4000	-	-	300-900	$\Re_{15\%}$= 0.11 -7 890	$6.1*10^{-12}$ $1*10^{11}$ 35 & $1.1*10^3$	[30] 2016
PDPP3T: $PC_{71}BM$ (Spin Coating)	Conventional PFN/Al ITO/PVK	240	-	-	400-900	$\Re_{40\%}$= 0.27 -1 840	- $2.1*10^{12}$ - & -	[31] 2016
CPDT-alt-BSe:PC71BM (Spin Coating)	Inverted ITO/PEIE MoO_3/Ag	175 Or 310	-	-	600-1200	$\Re_{4\%}$= 0.03 0 800	- $4*10^{11}$ 390 & -	[32] 2016
PMDPP3T: PCBM (Spin Coating)	Inverted ITO/PEIE PEDOT	150	-	-	300-1000	$\Re_{48\%}$= 0.33 -0.2 850	- $1*10^{13}$ - & -	[33] 2016
PDT: PCBM (Spin Coating)	Conventional BCP/Al ITO/PEDOT	-	-	-	300-1600	$\Re_{5\%}$= 0.04 -0.1 900	- $2*10^{12}$ - & -	[34] 2017
PBDTT-DPP: $PC_{71}BM$ (Spin Coating)	Inverted ITO/lysine MoO_3/Al	200	110	60	350-900	$\Re_{20\%}$= 0.12 -2 780	- $3.6*10^{12}$ - & -	[35] 2017
CPDT(P3): $PC_{71}BM$ (Spin coating)	Inverted ITO/PEIE MoO_3/Ag	385	-	-	600-1400	$\Re_{10\%}$= 0.12 0 800	- $8*10^{12}$ - & -	[36] 2017
PBD-TS1 $PC_{71}BM$	Conventional Al ITO/PEDOT	230	-	-	300-800	$\Re_{100\%}$= 0.6 -10 750	- $1*10^{12}$ - & -	[37] 2017
PCE10: $PC_{71}BM$ (Spin coating)	*Inverted ITO/PEIE PCE10/MoO_3/Ag*	-	-	-	-	$\Re_{28\%}$= *0.15 -0.1 680*	*$15*10^{-12}$ $2.3*10^{12}$ 35 &* -	*[38] 2017*
PDPP3T: PC71BM (Spin coating)	Inverted ITO/PEIE PDPP3T/MoO_3/Ag	-	-	-	-	- - -	- - - & -	[38] 2017
PBBTPD: Tri-PCBM (Spin Coating)	Inverted ITO/PPy Ba/Al	120	80	30	350-2500	$\Re_{10\%}$= 0.07 0 900	- - - & -	[39] 2018
PTTBAI: $PC_{71}BM$ (Spin Coating)	Inverted ITO/PEIE MoO_3/Ag	300	-	-	300-1200	$\Re_{30\%}$= 0.19 -2 800	- 10^{12} $3*10^3$ & -	[40] 2018
P3: $PC_{71}BM$ (Spin Coating)	Inverted ITO/AZO:PDIN MoO_3/Al	-	-	-	300-1700	$\Re_{10\%}$= 0.06 -2 800	- $2*10^{12}$ (-0.1 V) 30 & -	[41] 2018
PIPCP: PCBM (Spin Coating)	Inverted (Su-8/Parylene/) ITO/ZnO MoO_3/Ag	200	-	-	300-900	$\Re_{60\%}$= 0.38 -1 790	- $1.3*10^{11}$ - & -	[42] 2018
CPTD-TQ: $PC_{71}BM$ (Spin Coating)	Inverted ITO/ZnO:PEIE MoO_3/Ag	150 or 350	-	-	600-1400	$\Re_{10\%}$= 0.09 - 1100	- $5*10^{11}$ 400 & -	[43] 2018
PDPP3T: $PC_{71}BM$ (Spray Coating)	Conventional Al ITO/TFB	520	100	10	400-950	$\Re_{30\%}$= 0.21 -5 875	- $3.3*10^{12}$ - & $64*10^3$	[44] 2018
PCE10: $PC_{71}BM$ (Spin Coating)	*Conventional Al ITO/PFN-OX*	*3000*	*100*	*1*	*300-900*	$\Re_{45\%}$= *0.25 -20 700*	- - - & -	*[45] 2018*
PCE10: $PC_{71}BM$ (Spin Coating)	*Inverted ITO/ZnO PCE10/MoO_3/Ag*	*150*	-	-	*350-800*	$\Re_{50\%}$= *0.28 -0.5 700*	*$2.6*10^{-14}$ (vis) $1*10^{13}$ - & $700*10^3$*	*[46] 2018*

Table Continues in Next Page

CPhCDT-co-PSe:PCBM (Spin Coating)	Conventional ZnO/Al ITO/PEDOT	160	-	-	600-1400	$\mathfrak{R}_{6\%}$= 0.06 -2 1000	- $3*10^{10}$ 400 & -	[47] 2019
PNTT-H: $PC_{71}BM$ (Spin Coating)	Conventional PNDIT-PF_3N-Br/Al ITO/PEDOT	260	-	-	300-850	$\mathfrak{R}_{60\%}$= 0.36 -0.1 750	$1*10^{-13}$ $1*10^{13}$ $2*10^3$ & $1.2*10^3$	[48] 2019
PCDTPT: $PC_{71}BM$ (Inkjet Printing)	Inverted PEDOT/PFN PEDOT	300	135	60	400-1100	$\mathfrak{R}_{1\%}$= 0.00 -1 950	- $3.2*10^{10}$ $2*10^3$ & $1.2*10^3$	[49] 2019
PCPDTBT: $PC_{70}BM$ (Spin Coating)	Inverted ITO/Pentacene/C60 MoOx/Al	90	-	-	300-950	$\mathfrak{R}_{22\%}$= 0.13 -1 750	- - 200 & -	[50] 2019
P1: $PC_{70}BM$ (Spin Coating)	Inverted ITO/ZnO MoO_3/Ag	200	-	-	300-1200	$\mathfrak{R}_{8\%}$= 0.06 0 900	- $3*10^{10}$ 400 Hz & -	[51] 2020

NEP is the optical power in which the magnitude of the photogenerated current (or its associated electrical power) equals the noise current (or its associated electrical power). For high-performance OPDs, it is desirable to minimize *NEP*; *D** is the reciprocal of the normalized *NEP* with respect to the root square of the product between the photoactive area *A* and the bandwidth *B.* It is desirable to maximize *D** for high-performance OPDs. A more formal discussion of these parameters will be given in the **Section 2.4** of this chapter.

NIR OPDs have been selected such that one of their $\mathfrak{R}$ peaks (local or absolute) is within the NIR range (700 – 1100 nm), and it is at least ten percent of its ideal value ($\mathfrak{R} \geq \mathfrak{R}_{10\%}$). Exceptions of NIR OPDs with very low responsivity ($\mathfrak{R} < \mathfrak{R}_{10\%}$) are included when fabrication methods different to spin coating are reported and/or panchromatic spectral response beyond the NIR region is observed.

2.2.2.2 Highlights of OPDs with NIR Response at Lab Scale

Materials (PAL, ECE, HCE)

Table 3 shows that the PAL uses fullerenes (e.g., $PC_{71}BM$ or $PCE_{70}BM$, $PC_{60}BM$ or PCBM), whose optical absorption is mainly in the visible part of the electromagnetic spectrum and then the NIR absorption is defined by the polymers used in the PAL (e.g., PTT, PCE10, etc.). **Table 3** also summarizes the PAL thicknesses, which can range from the hundreds of nm up to the order of fewer than ten μm. Thickness adjustment has been the optimization route for having OPDs that rivals many of the performance metrics of Si PD in the visible part of the spectrum [5]. It is also noted that most of the devices do not require thermal annealing. When required, the highest temperature of the thermal annealing is 150 °C for 20 min; the longest time is 60 min at 135 °C.

The specific electrodes used in the reported OPDs depend on the chosen architecture (conventional and inverted). Some highlights in each architecture are described next.

For the inverted architecture, the ECE (bottom electrode) uses typically ITO on top of a glass substrate and a second oxide material (e.g., ZnO, ZnO nanowires or ZnO-NWs, etc.), an organic material or a succession of two organic materials (e.g., PEIE, PFN-OX, lysine, pentacene/C_{60}, etc.), or a hybrid composed of oxide materials and organic materials (e.g., SnO_2/PEIE, ZnO:PEIE, etc.). All these materials are expected to reduce the WF of the pristine ITO. On the other hand, the HCE (top electrode) is typically composed by a succession of an oxide material and a metallic material (e.g., MoO_x/Al or MoO_3/Al,

MoO_3/Ag, MoO_3/Au, etc.) or simply an organic layer (e.g., PEDOT:PSS). All these materials have a higher effective WF compared to the ECE.

For the conventional structure, the HCE (bottom electrode) typically uses the glass/ITO as the substrate for the fabrication of OPDs as the inverted structure. However, different organic layers (e.g., PEDOT, PFN-OX, TFB, PVK), some nanoparticle-based layers (e.g., CdTe-QDs), or a hybrid of organic and oxide materials (e.g., PEDOT:PSS/MoO_3) are typically used to increase the WF of ITO. The ECE (top electrode) range a variety of metallic materials (e.g., Ca, Ca/Al, Ca/Ag, Al, LiF/Al, etc.), and hybrids between organic and metallic materials (e.g., PFN/Al, BCP/Al, PNDIT-PF3N-Br/Al, etc.). These electrodes are expected to have a lower WF with respect to the WF of the HCE.

Performance Metrics

The literature review shows that statistical information related to the performance metrics ($\Re$, *NEP*, *D**) discussed next is rarely reported, suggesting that the results are obtained from the best performing OPD.

According to **Table 3,** responsivities higher than 0.25 A/W are reached when the responsivity is at least 38% of its ideal value ($\Re_{38\%}$) and typically are enabled by an external voltage (*V*) applied to the device. For very negative applied voltages and very unbalanced binary compositions (e.g., donor:acceptor = 100:1) [45], higher responsivity values than the ideal limit ($\Re > \Re_{100\%}$) can be attained (not shown in **Table 3**).

Table 3 also shows that detectivity values (*D**) for polymer:fullerene (donor:acceptor) NIR OPDs range between 10^{10} and 10^{13} Jones. However, this compiled information evidences the difficulty of comparing NIR OPD technologies in terms of *NEP* or *D**, which are not always reported. Furthermore, many reported values of *D** are calculated under the assumption that dark current (sometimes interchangeably defined as average current I_{DARK} or the reverse saturation current I_o) is the main source of noise. This assumption ignores other noise sources relevant at low frequencies as the Flicker noise, which are dominant when the modulation frequency (f_{mod}) of the targeted light signal is not high enough. Therefore, a major effort in the correct characterization of OPDs and next-generation thin-film photodetectors is required to determine accurately their performance metrics [52].

2.2.2.3 The PCE10:$PC_{71}BM$ NIR OPD

Among the reported OPDs summarized in **Table 3**, the ones based on the PCE10 polymer (a.k.a. PTB7-Th or PBDTT-FTTE) combined with the acceptor fullerene material $PC_{71}BM$ stand out among the OPDs with the highest responsivities in the NIR region. PCE10 is also commercially available from various chemical manufacturers [53-58] and it can be paired with non-fullerene acceptors which are the driving materials for the dramatic increments in the power conversion efficiencies of organic solar cells [59].

In the context of organic solar cells, PCE10:$PC_{71}BM$-based devices have been able to achieve 7% [60], 9% [61, 62] and 11% [63, 64] of power conversion efficiency after optimization processes (e.g., donor:aceptor composition, thickness, additives, selection of

electrodes, etc.). It has been shown that the thermal annealing (> 70 °C) of PCE10:$PC_{71}BM$ devices induces degradation in the current-voltage (*I-V*) characteristic curves (by decreasing the shunt resistance) and reduces the external quantum efficiency (affecting the responsivity and the power conversion efficiency) [65].

On the other hand, in the context of photodiodes, the PCE10:$PC_{71}BM$ system is attractive not only for the high responsivities that can attain in the NIR, but also as a model system to apply optimization strategies when thermal annealing (> 70 °C) is not required (as evidenced from various reported OPDs in **Table 3**), or beneficial to increase $\mathfrak{R}$, reduce the noise and the *NEP*, and ultimately maximize *D**.

Some of the alternative strategies to reduce the noise and/or improve the responsivity (assisted by an external voltage) of PCE10:$PC_{71}BM$ OPDs have been explored through the tuning of the thickness of the PAL and its chemical composition (ratio of donor and acceptor materials) [29, 45]. Noise in PCE10:$PC_{71}BM$ OPDs has been reduced by the addition of a layer of PCE10 (polymer buffer) at the interface between the PAL and the HCE [38, 46]. This latter strategy has the disadvantage of diminishing $\mathfrak{R}$ as part of the light is absorbed at this polymer buffer without necessarily dissociating the excitons generated by the absorbed photons as efficiently as in a BHJ.

2.3 Physics of Organic Photodiodes (OPDs) – Description of the Device at the Material Level

This section discusses the energetic properties involved in the electrodes as well as in the PAL at atomic, molecular, and solid-state scales (e.g., thin films), to point out their origins and inter-relations [66, 67].

2.3.1 Energetic Properties of OPDs: Absorber or Photoactive Layer (PAL)

The typical molecular components present in the PAL of an OPDs are "large" polymeric molecules and/or "small" molecules (e.g., fullerene and non-fullerene molecules). A PAL can be deposited either by the evaporation of organic materials (typically small molecules) or by solution-based techniques (e.g., spin coating, spray coating, etc.). For these solution-based techniques, the organic materials are dissolved in an organic solvent (e.g., chlorobenzene, dichlorobenzene, etc.) and exposed to drying conditions that transform the solution into a film. The thickness of the films typically ranges from the nanometric to micrometric scale. When a binary composition of organic materials is selected to build the PAL, the two materials can be independently stacked in two sequential layers (bilayers) within a two-step deposition approach. Alternatively, they can be first mixed in their solid state and then dissolved in a solvent to form a single layer (bulk heterojunction or BHJ) within a one-step deposition approach. In this research, the latter approach is used for the fabrication of NIR OPDs.

2.3.1.1 Generalities of the Energetics in Nanosystems

Any nanosystem can be described by a mathematical operator known as the Hamiltonian $\widehat{H}$, which expresses mathematically all the interaction between the subatomic particles in the system (mainly electrons and nuclei). The $\widehat{H}$ operator, acting on the system's state wavefunction φ (a mathematical object that describes the state of the nanosystem), provides the total energy value E of the nanosystem through an expression known as the time-independent Schrödinger equation [68]:

$$\widehat{H}\varphi = E\varphi \tag{1}$$

An analytical solution of the Schrödinger equation is generally difficult to obtain with existing analytical tools beyond the simplest nanosystems such as the atom of H and the molecule of H_2^+. Approximations (e.g., Born-Oppenheimer where nuclei are quasi stationary) and numerical methods are required for larger systems with a computational trade-off between different levels of precision and the number of electrons (size of the nanosystem)[68]. Computational packages (e.g., Q-chem 5.0) can approximately solve the Schrödinger equation to calculate energetic (band)gaps of candidate molecules (materials) to be used in NIR OPDs, and they can be also obtained experimentally.

2.3.1.2 The Energetics in Sub-Nanometric Systems: Atoms and "Small" Molecules

In the context of organic materials, although other atoms, such as H, S, N, F, Cl, and O, can also be present, the backbone of "large" molecular systems (e.g., polymers, fullerenes, etc.) is mostly based on carbon (C) atoms. Therefore, most of the energetic aspects are dominated by the C atoms and the form in which they bond and interact with others.

The electronic properties of an isolated C atom can be described through atomic orbitals: one-electron wavefunctions derived from the Schrödinger equation. The *s* and *p* atomic orbitals are of major relevance as C atoms contain only six electrons (see **Figure 4.A**). These atomic orbitals can lead to more complex molecular orbitals which are commonly used to describe bonding and charge transport in molecules.

Electronic energies associated with atomic orbitals in a C atom can be calculated by using the Schrödinger equation with an approximated Hamiltonian and measured experimentally through spectroscopy. In **Figure 4**, the C atom is surrounded by its atomic orbitals ($2p_x$ and $2p_z$, or $2p_y$ and $2p_z$), and the symbols ↑↓ represent the electronic occupation and indicate the value of the spin. **Figure 4.A** shows that although the atomic orbitals $2p_x$ and $2p_y$ are occupied with a defined spin, the occupations in the atomic orbitals ($2p_x$ and $2p_z$, or $2p_y$ and $2p_z$) with the same or opposite spin are equivalent and possible.

The Analytical Energetic Gap for "Small" Molecules in the Gas Phase:

Molecular orbitals (e.g., σ, π, π^*, etc.), a linear combination of atomic orbitals, can be used to describe the state of a molecule. For example, when two or more carbon atoms interact through a conjugated bonding (alternating single and double bonds) in a linear-like array (e.g., ethene, butadiene, hexatriene, etc.), the highest occupied molecular orbitals have a *p*-orbital-like shape with nodes in the plane of the molecule in their contributing atomic orbitals. These are known as π molecular orbitals (see **Figure 4.B**). The longer a linear-like carbon array, the higher the number of electrons, and the higher the number of nodes in the orbitals perpendicular to molecular plane, which resembles the behavior of the wavefunctions of a free particle (see **Figure 4.B**). It is the overlap of p_z atomic orbitals or equivalently extended π molecular orbitals that provides the efficient transport of carriers within molecules (i.e., that delocalizes the electronic density), as in conjugate rings or aromatic groups.

Each molecular orbital of conjugated chains or aromatic groups has an associated energy (see **Figure 4.B**). The occupied π molecular orbital with the highest energy is called the highest occupied molecular orbital (HOMO), and its associated energy is E_{HOMO}. The next π molecular orbital with energy E_{LUMO} is unoccupied and is called the lowest unoccupied molecular orbital, LUMO. Despite approximations involved in the calculation of E_{HOMO} and E_{LUMO} (including the assumption of 0 K and the Born-Oppenheimer approximation), these values are in many cases the only design guidelines for the selection of materials that form a PAL.

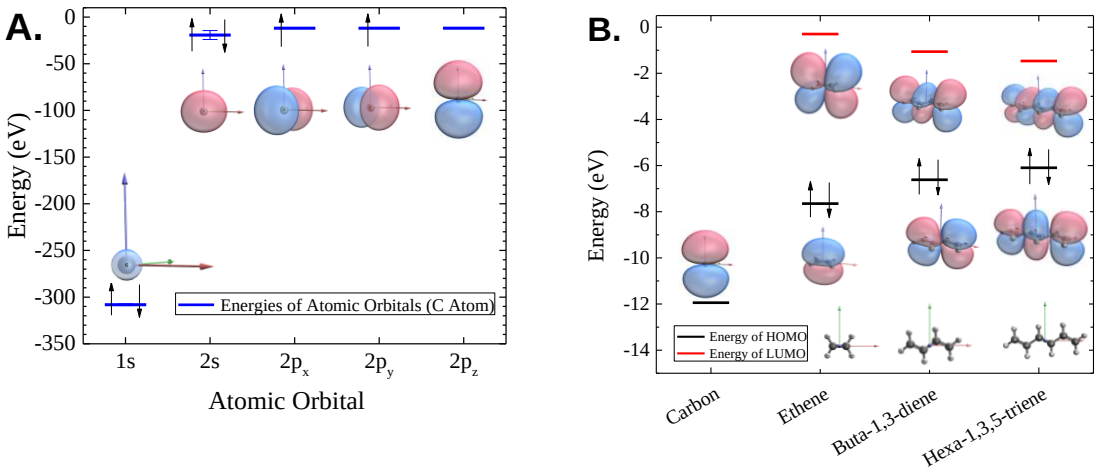

Figure 4. Energy diagrams and atomic/molecular orbitals calculated using the computational package Q-Chem 5.0. A. Carbon atom. Method: coupled cluster or CC. Basis set: correlated-consistent triple-zeta aug-cc-pVTZ at the level of explicit single and double and perturbative triple excitations. B. Ethene, butadiene and hexatriene molecules. Method: CC. Basis set: correlated-consistent triple-zeta aug-cc-pVTZ basis set at the level of explicit single and double and perturbative triple excitations. Red lines represent E_{LUMO} is marked for each molecule with a red horizontal line. E_{HOMO} is marked for each molecule with a black horizontal line. Simulations were done at the Georgia Institute of Technology by the author of this dissertation.

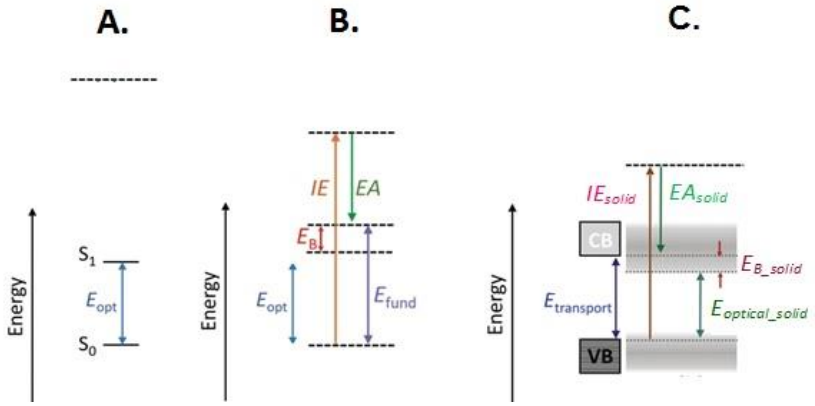

Figure 5. Energy diagrams. A. Ground state (S_0), first excited state (S_1), and optical gap (E_{opt}) in molecules. B. Ionization potential (IE), Electron affinity (EA), exciton energy (E_B), optical gap (E_{opt}), and fundamental gap (E_{fund}) in molecules in a gas phase. C. Ionization potential (IE_{solid}), Electron affinity (EA_{solid}), exciton energy (E_{B_solid}), optical bandgap (E_{opt_solid}), and transport bandgap (E_{fund}) in molecules in a solid-state phase. Adapted from [66].

LUMO-HOMO gap (molecule): The gap defined by the difference between the LUMO and the HOMO energies ($E_{LUMO\text{-}HOMO} = E_{LUMO} - E_{HOMO}$). This is in general different from experimental gaps such as the optical gap E_{opt} and the fundamental gap E_{fund}.

Experimental Energetic Gaps of "Small" Molecules in the Gas Phase:

Figure 5.A illustrates the total energetic state of a molecule rather than the energies for each independent molecular orbital (e.g., the HOMO and LUMO energies). This lack of detail in the energetic description is reflected in the absence of ↑↓ symbols because individual electrons are no longer represented. This description can represent two different scenarios: 1) when a molecule is excited optically or 2) when the charges are added or removed. These scenarios enable the definition of two energetic gaps: the optical gap and the fundamental gap [66].

Optical gap (molecule): In this picture (see **Figure 5.A**), the fundamental state is described by the molecular state S_0 and the first accessible optically excited state is defined as S_1. It is typically measured by gas-phase absorption spectroscopy. The optical gap can be defined as $E_{opt} = E_{S1} - E_{S0}$, and in either case (in the fundamental or excited state), the molecule remains neutral (with a net charge of null).

Fundamental gap (molecule): A second scenario (**Figure 5.B**) is related to those levels where a charge transfer has occurred (e.g., oxidation and reduction). This scenario creates a different energetic (and bandgap) with respect to the previously defined gaps where a molecule is in neutral state. Therefore, the fundamental bandgap E_{fund} is defined

as $E_{fund} = IE - EA$, where *IE* is the ionization energy or ionization potential (measured by gas-phase ultraviolet photoelectron spectroscopy or UPS) and *EA* is the electron affinity (measured by gas-phase electron attachment spectroscopy).

Relating the optical gap and the fundamental gap: The *IE* is the difference between the total energy of a molecule in the S_0 state (E_{S0}) and the total energy of the ionized molecule or the molecular anion (E_{S0}^-) and can be written as $IE = E_{S0} - E_{S0}^-$. The *EA*, on the other hand, is the difference between the total energy of the reduced molecule or the molecular cation (E_{S0}^+) and the total energy of a molecule in the S_0 state (E_{S0}), which can be written as $EA = E_{S0}^+ - E_{S0}$. Both resulting energies *IE* and *EA* are redrawn in a new energy diagram system (see **Figure 5.B**) with S_0 and *IE* re-aligned. In general, $E_{LUMO-HOMO} \neq E_{opt} \neq E_{fund}$.

Exciton binding energy (molecule): The exciton binding energy in a molecule can be defined as $E_{B\_molecule} = E_{fund} - E_{opt}$.

2.3.1.3 The Energetics in Nano/Micrometric Systems: "Large" Molecules and Thin Films

Nanosystems in the Solid-State Phase: Experimental Energetic Bandgaps

The high number of C atoms in a very long conjugated chain, as in polyacetylene, favors the delocalization of the electrons. The electronic density is more spread out, and the electronic energetic landscape transitions from quantum levels to quasi-continuous

bands. Aromatic systems in one direction (e.g., pentacene) and two directions (e.g., graphene) can also display energy bands rather than quantized energy levels.

Not only extended molecular systems such as polyacetylene, graphene or pentacene can form energetic bands as a result of their intramolecular interactions. Through intermolecular interactions (e.g., Van der Waals), "small" and "large" molecules can also form solids, broadening the energy levels of the independent molecules and transitioning to energy bands (see **Figure 5.C**). The formation of energetic bands may be understood as the result of the high number of molecules (~10^{21} molecules/cm^3) that can interact, and then the high probability of overlap among π molecular orbitals as they are spatially close in a solid, which favors energetic interactions. The same film contains many types of orderings reflected in the fact that crystalline, polycrystalline, and amorphous domains are possible, and the relevant domain depends on the processing conditions of the organic thin film (e.g., deposition method, annealing condition, etc.). In solids, energetic bandgaps, unlike simple energetic gaps, can be defined as discussed below [66].

Optical bandgap (solid): The optical bandgap in a solid is the difference between the energy of a solid in the ground state and its first optical excitation. The solid remains with neutral charge even when it is optically excited.

Relating the optical bandgap (molecules in the solid phase) and the optical gap (molecules in the gas phase): The optical bandgap of the solid is lower than the gap of molecules in the gas phase ($E_{optical\_solid} < E_{optical}$).

Transport bandgap (solid): As with molecules, key energetic values can be defined and measured. Ionization energy (IE_{solid}) measured through UPS can quantify the energy

required to remove an electron from a solid. Electron affinity (EA_{solid}), through inverse photoemission spectroscopy (IPES), quantifies the energy to add an electron in a solid. A transport bandgap $E_{transport}$ in a solid can be defined as $E_{transport} = IE_{solid} - EA_{solid}$.

Relating the transport bandgap (molecules in the solid phase) and fundamental gap (molecules in the gas phase): The transport bandgap in a solid is lower than the fundamental gap of the same type of molecules in $E_{transport} < E_{fund}$.

Exciton energy (solid): The binding energy of the exciton in the solid can also be defined as $E_{B\_solid} = E_{transport} - E_{optical\_solid}$.

2.3.2 Energetic Aspects of OPDs: Electrodes and Electrode/PAL Interfaces

2.3.2.1 The Energetics in Electrodes (ECE and HCE)

The most relevant energetic aspect of the electrodes is their WF. WF quantifies the minimum energy required to extract the first electron from the electrode. As per the working principle of OPDs, proper operation requires two electrodes with a contrast of the WF values of 1 eV (or more) between the two electrodes. Therefore, ECE and HCE are typically two different materials and they are chosen according to the equipment capabilities (e.g., thermal evaporator, sputtering, etc.), material availability, and the energetics of the PAL. The WF depends not only on the type of material, but also on its surface characteristics. Shallow nanometric materials as well as surface treatments such as oxygen plasma or UV radiation can modify the material's WF (see **Figure 6.A**).

2.3.2.2 The Energetics in Electrode/PAL Interfaces

When the electrode (ECE or HCE) interacts with the PAL [69, 70], the thermal equilibrium is reached naturally in the absence of an electrical or optical excitation. Thermal equilibrium means that the WF of the electrode aligns with the Fermi energy of the semiconductor. Fermi energy is typically defined as the average between the ionization potential and the electron affinity for an undoped PAL.

If the WF of the electrode and the Fermi level of a semiconductor are different, the vacuum level of the PAL will shift up or down with respect to the vacuum level of the electrode to attain thermal equilibrium. This generates an energetic transition at the electrode/PAL interface, which, depending on the nature of the electrode and the density of states (DoS), can be abrupt (step) or smooth (p-n junction).

The type of energetic transition (abrupt or smooth) for a given PAL can be established through the Z curve (see **Figure 6.B**). This curve relates the changes in the PAL's Fermi level when the PAL is deposited on various electrodes with different WF values. Three regions can be identified: two Fermi level pinning regions, where the PAL's Fermi level is independent of the substrate's WF (slope = 0), and a Schottky-Mott region, where the PAL's Fermi level increases/decreases linearly (slope > 0) with the substrate's WF.

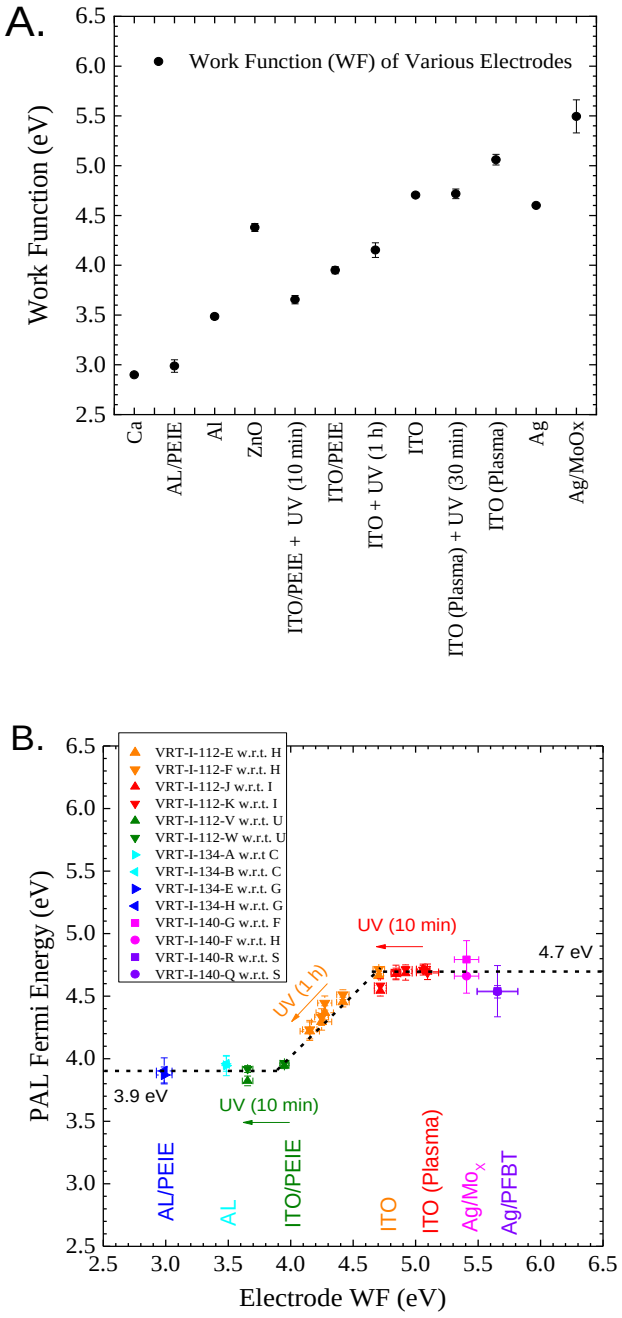

Figure 6. A. Work function (WF) of several types of electrodes. B. The Z curve for a P3HT:ICBA (donor:acceptor) PAL deposited on different electrodes. The Schottky-Mott region is identified when the slope of the dashed line is close to one. The Fermi level pinning region is identified when the dashed line is constant (slope = 0). Measurements were done at the Georgia Institute of Technology by the author of this dissertation.

In the Schottky-Mott region, if the slope < 1 (e.g., clean electrode/PAL interface), transitions are abrupt, implying a DoS with a Lorentzian form, in which case a charge transfer might not occur or occur at only distances very close to the interfaces (one or two layers). The value of such abrupt transitions can be quantified and modeled by dipoles coming from different physical origins, such as dangling bonds, physisorption, and/or chemisorption of neutral and/or charged heteroatoms (including noble gases) and molecules. This energetic step might be accentuated when the molecular species have an internal dipole. In contrast, if the slope = 1 (e.g., passivated electrode/PAL interface), the energetic bending at the interface is similar to an inorganic p-n junction in that the transition is smooth, the DoS has a Gaussian shape and, as a result, a charge transfer between the electrode and several layers of the PAL is possible.

In addition to select NIR PAL/electrode interfaces where the Schottky-Mott region displays a slope of one, electrodes close to the Fermi level pinning region are desirable for creating (quasi) ohmic contacts.

2.3.3 Energetic Aspects of OPDs: Devices

The presence of electrodes determines the energetic alignment along the OPDs in thermal equilibrium and influences the energetics at the interface between the A and D materials. Because describing the energetics as a function of space in a BHJ configuration is so complex (compared to a bilayer configuration), for simplicity this research will describe BHJ PAL as a single semiconductor. This single semiconductor is an effective material that has the conduction band or CB (with electron affinity energy as the bottom

edge value of the conduction band) of the acceptor material, and the valence band or VB (with ionization potential energy value as the top edge of the valence band) of the donor material. The energetics of the device will be described in the presence and absence of the targeted signal when no external voltage has been applied to the device.

The Energetics of OPDs in the Absence of a Targeted Signal (Dark Condition)

The energy diagram in **Figure 7** shows a PAL with electron affinity *EA* energy (bottom of the CB), and ionization potential *IP* energy (top of the VB), and a Fermi energy E_F in the middle denoting no doping. This PAL is sandwiched between two different pairs of electrodes before (BC) and after (AC) they come in contact and reach thermal equilibrium. The details at the ECE/PAL and PAL/HCE interfaces are omitted.

For the first pair of electrodes (**Figure 7.A** and **Figure 7.B**), the electrodes' WFs (WF_{ECE} and WF_{HCE}) are within the PAL's transport bandgap and have a low WF contrast ($WF_{ECE} \approx WF_{HCE}$), indicating the Schottky-Mott region. For the second pair of electrodes (**Figure 7.C** and **Figure 7.D**), the WF of both electrodes (WF_L and WF_H) are close to the PAL's CB ($WF_L \approx EA$) and VB ($WF_H \approx IE$), indicating the Fermi level pinning region. Vacuum levels (VL) are expected to be continuous everywhere in the OPD.

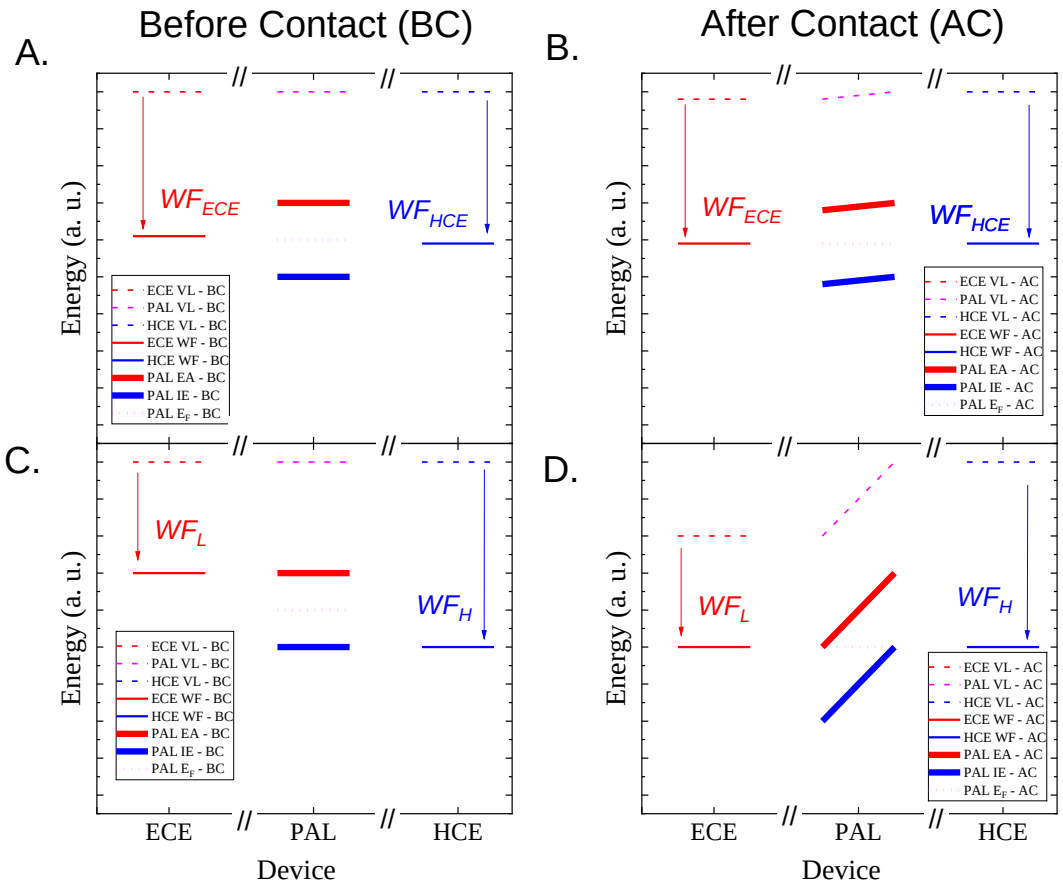

Figure 7. Energy diagram for an OPD in dark condition. Dashed lines represent the vacuum level (VL) energies for ECE (red), PAL (pink) and HCE (blue). Thin continuous lines represent the work function (WF) of the ECE (red) and HCE (blue) electrodes. Thick continuous lines represent the bottom edge of the conduction band (CB) or electron affinity (EA) and the top edge of the valence band (VB) or ionization energy (IE) of the PAL (red and blue). The dotted line represents the Fermi level (E_F) energy of the PAL (pink). Electrodes in the Schottky-Mott region: A. Before contact (BC). B. After contact (AC). Electrodes in the Fermi level pinning region: A. Before contact (BC). B. After contact (AC).

The pair of electrodes resembling the Schottky-Mott region shows a lower energetic slope in the PAL (**Figure 7.B**), compared to the region where the Fermi level pinning is (almost) achieved (**Figure 7.D**), indicating that the electric field will be stronger in the Fermi level pinning region. The Fermi level pinning region has other important consequences beyond attaining (quasi) ohmic contacts at the PAL/electrode interfaces. A stronger electric field prevents the undesired injection of carriers from the electrodes to the PAL and favors the extraction of charges before they recombine, but it also enables the extraction of thermally generated carriers in the PAL, which contributes to the dark current.

Beyond the type of electrodes selected (either in the Schottky-Mott region or in the Fermi level pinning region), this scheme also illustrates that when the PAL is spatially very thin, a higher probability of charge transfer between the electrodes by tunneling than is found in a thick PAL contributes to the noise in the device.

The Energetics of OPDs in the Presence of an Optical Signal

In the presence of an optical signal, the Fermi level will no longer be flat and will be split into quasi-Fermi levels for electrons and holes depending on the operation point. In short-circuit conditions, the photovoltage will be null, the quasi-Fermi levels will be indistinguishable but the transport and collection of photogenerated carriers lead to a photocurrent. In open-circuit conditions, the current will be zero, but the electron and hole quasi-Fermi levels will be split and yield a photovoltage. In forward bias, when a voltage is applied the device can exhibit both a photovoltage and a photocurrent. The device is said to operate in the photovoltaic mode. In reverse bias, the OPD is said to operate in the

photoconductive mode. In an ideal device, the current under illumination in revers bias with be proportional to the irradiance of the optical signal and independent of the bias voltage.

2.4 Physics of Organic Photodiodes (OPDs) – Description of the Device at the Circuit Level

Two typical operation scenarios for photodetectors, when the input variable is the optical power and the output variable is the current, are shown in **Figure 8**. Under illumination condition or in presence of the optical signal (**Figure 8.A**), an incident optical signal with optical power $P_{opt}(t)$ is absorbed by the photodetector, generating a current $i_{LIGHT}(t)$, which is also referred to as a photocurrent; under dark condition or in absence of the optical signal (**Figure 8.B**), a current at the output $i_{DARK}(t)$ is measurable. This current is generated by the thermal excitations of carriers, and parasitic effects.

2.4.1 Definitions Related to the Output Variable (Current)

From the temporal behavior of the currents under illumination $i_{LIGHT}(t)$ (current in the presence of the optical signal also known as photocurrent), and dark conditions $i_{DARK}(t)$ (current in the absence of the optical signal), which are both output variables, various quantities can be defined in order to establish the performance metrics of photodetectors.

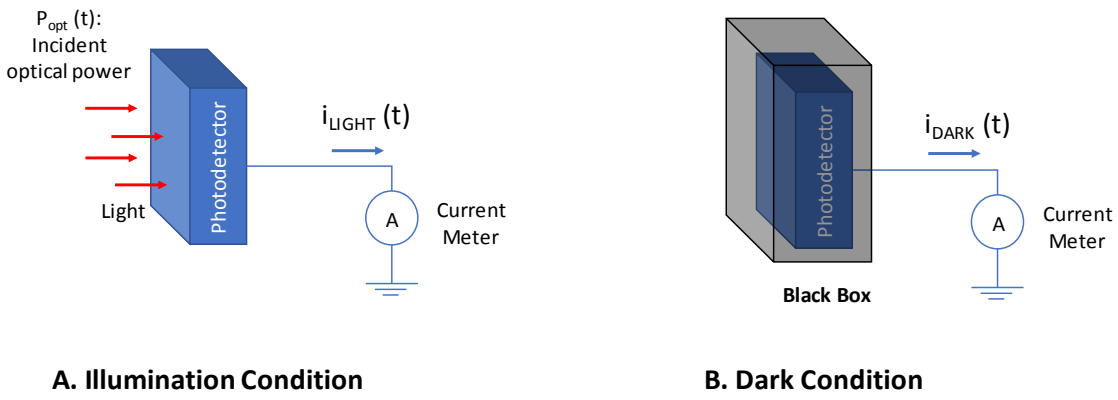

Figure 8. Input and output variables of a photodetector.

The definitions of signals and equations in the subsequent subsections follow the guidelines in [71].

2.4.1.1 Current under Light Condition (Presence of the Optical Signal) - Photocurrent

Average Photocurrent

Under light condition, a measured and discretized current in steady state can be numerically described as a scalar through an average as

$$I_{LIGHT} = \langle i_{LIGHT}(m) \rangle = \sum_{m=0}^{M-1} \frac{i_{LIGHT}(m)}{M}, \qquad m = 0, 1, 2, \ldots, M-1 \tag{2}$$

where M is the total number of measurement points taken during a time period. The steady state can be defined as the condition in which average values taken at consecutive time periods remain almost at a constant value I_{LIGHT}. In practice, when a set of measurement

points include a transient, it is possible to focus on the time window in which the steady state seems to have been reached and evaluate the stability condition (I_{LIGHT} quasi-constant for consecutive time periods). If the steady state has not been achieved, the set of measurement points of the photocurrent, $i_{LIGHT}(m)$, can be used to find an analytical expression (mathematical fitting), $\hat{\imath}_{LIGHT}(m)$, and estimate the steady-state photocurrent (value at longer times) through mathematical extrapolation.

RMS Current under Light Condition (RMS Photocurrent)

On the other hand, the root-mean-square (RMS) value, associated to the measured photocurrent in steady state, can be defined as

$$I_{rms,light} = \sqrt{\frac{\sum_{m=0}^{M}(i_{LIGHT}(m) - I_{LIGHT})^2}{M-1}}, \qquad m = 0, 1, 2, \dots, M-1 \tag{3}$$

Under light condition, $I_{rms,light}$ will be used to quantify the amount of noise generated when the optical signal is present. When the steady state has not been attained, the photocurrent $i_{LIGHT}(m)$ can be approximated to an analytical expression $\hat{\imath}_{LIGHT}(m)$ and the residuals of the fitting process are used to calculate the RMS value of the current.

2.4.1.2 Current under Dark Condition (Absence of the Optical Signal)

Average Current under Dark Condition

As under light condition, a similar scalar can be defined for the measured and discretized current under dark condition:

$$I_{DARK} = \langle i_{DARK}(m) \rangle = \sum_{m=0}^{M-1} \frac{i_{DARK}(m)}{M}, \qquad m = 0, 1, 2, \dots, M-1 \tag{4}$$

where M is the total number of measurement points, which is not necessarily the same number of measurement points under illumination. In practice, if a transient region is present in the measured signal, focus and evaluation of the average values can be done at the final points of the measurement set in which the steady state has been attained. Otherwise, a mathematical extrapolation can be done to estimate the steady-state value (at longer times) of the current under dark condition.

RMS Current under Dark Condition

The root-mean-square (RMS) values for the measured current in steady state can be defined as

$$I_{rms,dark} = \sqrt{\frac{\sum_{m=0}^{M} (i_{DARK}(m) - I_{DARK})^2}{M-1}}, \qquad m = 0, 1, 2, \dots, M-1 \tag{5}$$

Under dark condition, $I_{rms,dark}$ will be used to quantify the amount of noise present in the device when there is no optical signal. When the steady state has not been attained, $i_{DARK}(m)$ can be approximated to an analytical expression, $\hat{\imath}_{DARK}(m)$, and the residuals can be used to calculate the RMS value.

2.4.1.3 Photogenerated Current

The detected signal can be quantified in terms of the photogenerated current, $i_{PG}(t)$. The photogenerated current, $i_{PG}(t)$, is the difference between the current in absence of the signal, [$i_{DARK}(t)$], and the current in presence of the signal or photocurrent [$i_{LIGHT}(t)$]. A discretized expression for the photogenerated current can be written as $i_{PG}(m) = i_{DARK}(m) - i_{LIGHT}(m)$. In practice, the photocurrent, $i_{LIGHT}(m)$, and the dark current, $i_{DARK}(m)$, are recorded separately and the photogenerated current, $i_{PG}(m)$, is then calculated. Next, the calculations of the average of the photogenerated current and its RMS value are described.

Average Value of the Photogenerated Current

In steady state, average values may be used to have an average expression for the photogenerated current as

$$I_{PG} = I_{DARK} - I_{LIGHT} \tag{6}$$

Note that I_{PG} is zero in absence of the optical signal and becomes greater than zero according to the magnitude of the P_{opt} of the signal. Typically, the relationship between P_{opt} of the I_{PG} is linear P_{opt} in the order of nW or higher. However, this does not always hold, particularly at low P_{opt} in the order of fW as discussed later in the results section of this dissertation.

RMS Value of Photogenerated Current

When the signals $i_{DARK}(m)$ and $i_{LIGHT}(m)$ recorded at different time windows are used to calculate the photogenerated currents through

$$i_{PG}(m) = i_{DARK}(m) - i_{LIGHT}(n) \tag{7}$$

the total RMS value is increased as

$$I_{rms,pg}{}^2 = I_{rms,dark}{}^2 + I_{rms,light}{}^2 \tag{8}$$

This expression shows that the RMS value of the photogenerated current will be higher than RMS values of the dark current and the photocurrent. In practice, it is expected that $I_{rms,dark} \approx I_{rms,light}$ at low optical powers and then $I_{rms,pg} \approx \sqrt{2}\, I_{rms,dark} \approx \sqrt{2}\, I_{rms,light}$. However, this is an algebraic consequence rather than an actual phenomenon taking place at the device and circuit level, where these two signals [$i_{DARK}(m)$ and

$i_{LIGHT}(m)$] are not physically subtracting. An alternative strategy to quantify the RMS value of the photogenerated current is described next.

The discretized version of the current under dark condition $i_{DARK}(m)$ can be approximated (including transient effects) with an analytical expression $\hat{\imath}_{DARK}(m)$. Then, the photogenerated current $i_{PG}(m)$ can be expressed as

$$i_{PG}(m) = \hat{\imath}_{DARK}(m) - i_{LIGHT}(n) \tag{9}$$

The average of photogenerated current $I_{PG}(m)$can be written as

$$I_{PG} = \langle i_{PG}(m) \rangle = \sum_{n=0}^{N-1} \frac{i_{PG}(m)}{M}, \qquad m = 0, 1, 2, \dots, M-1 \tag{10}$$

where the minimum I_{PG} will be zero under dark condition if an appropriate analytical approximation [$\hat{\imath}_{DARK}(m)$] of the dark current [$i_{DARK}(m)$] has been made. This approach is especially helpful to subtract any slow dynamics that can be present in the absence of light, and then $i_{PG}(m) = 0$ under dark condition and $i_{PG}(m) > 0$ in presence of light.

The RMS current value associated to the photogenerated current $i_{PG}(m)$ can be written as

$$I_{rms,pg} = \sqrt{\frac{\sum_{m=0}^{M}(i_{PG}(m) - I_{PG})^2}{M-1}}, \qquad m = 0, 1, \dots, M-1 \tag{11}$$

2.4.2 Some Relevant Performance Metrics

2.4.2.1 Response, Rise and Fall Time

When the targeted optical signal is modulated through a pulse train, the response rise time can be defined as the time that the photogenerated current in the OPD takes to go, for example, from 10% to 90% of the maximum current in steady state. Conversely, the response fall time is the time that the photogenerated current takes to go from 90% of its maximum value to 10%.

2.4.2.2 Linear Dynamic Range (LDR)

Several definitions of the linear dynamic range (*LDR*) have been reported not only in the context of OPDs [16, 72], but also in other thin-film photodetector technologies [73, 74]. This is an important metric for photometry applications. In all the cases, the *LDR* is defined in decibels (dB) and is proportional to the ten-base logarithmic ratio between current or power (density) values. A general expression can be written as

$$LDR = k_{LDR} \log \frac{Max}{Min} \tag{12}$$

where k_{LDR} is a pre-factor defined as 10 or 20, and *Max* and *Min* are the maximum and minimum current or power (density) values, respectively. *LDR* can be simply named as

dynamic range (*DR*) when no strict criterion of linearity is defined. **Table 4** presents a summary of definitions.

Table 4. Definitions of DR and LDR

Metric	k_{LDR}	***Minimum (Min)***	***Maximum (Max)***	***Ref.***
LDR	-10 or -20	Min. current (in linear regime)	Max. photocurrent (in linear regime)	[72]
DR	20	Dark current density	Photocurrent (measured at 1 mW/cm^2)	[16]
DR	20	Min. detectable optical power (no linear regime mentioned)	Max. optical power (in linear regime)	[12, 13]
DR	20	Lower photocurrent resolution	Max. photocurrent (in linear regime)	[75]

2.4.2.3 Responsivity ($\Re$)

It is the responsivity $\Re$ that enables the transduction between the incident optical power (P_{opt}) and the measured photogenerated current (I_{PG}) in the OPD**.** $\Re$ is dependent on the wavelength λ of the optical signal. In the ideal case of 100% absorption of photons and 100% photogeneration and collection of carriers, an ideal responsivity $\Re_{100\%}$ for an OPD with no gain can be defined for λ_{nm} in nm as

$$\Re_{100\%} = \lambda_{nm}/1240 \tag{13}$$

In many NIR OPD, $\Re$ depends not only on the wavelength λ, but also on the external bias (V) of the NIR OPD, which typically improves the value of $\Re$. $\Re$ can be independent of P_{opt} (constant responsivity) or dependent on P_{opt}. **Figure 9** highlights the ideal case of the responsivity, i.e., $\Re = \Re_{100\%}$ (upper line), and additional cases $\Re_{90\%}$, $\Re_{75\%}$, $\Re_{60\%}$, $\Re_{45\%}$, $\Re_{30\%}$, and $\Re_{10\%}$.

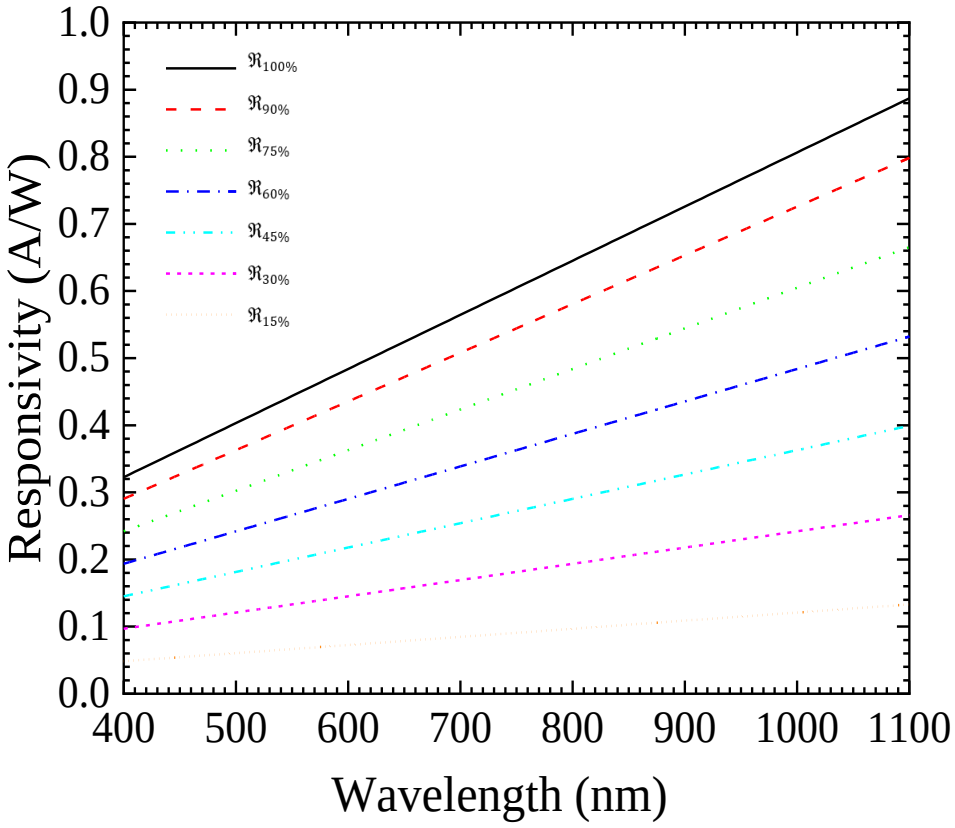

Figure 9. Various responsivity values as a function of wavelength λ: $\Re_{100\%}$ (ideal condition), cases $\Re_{90\%}$, $\Re_{75\%}$, $\Re_{60\%}$, $\Re_{45\%}$, $\Re_{30\%}$, and $\Re_{10\%}$. The responsivity is calculated based on equation (13).

2.4.2.4 Signal-to-Noise Ratio (SNR)

The signal-to-noise ratio (*SNR*) quantifies the relative amount of the targeted signal with respect to the amount of noise. *SNR* can be defined as a ratio of current or power values. For currents, $SNR_{current}$ [76] can be defined as

$$SNR_{current} = \frac{I_{PG}}{I_{rms,pg}} \tag{14}$$

where I_{PG} is the photogenerated current and $I_{rms,pg}$ is the root-mean-square (RMS) of I_{PG}. It is also possible to define SNR_{power} [76] as

$$SNR_{power} = \frac{{I_{PG}}^2}{{I_{rms,pg}}^2} \tag{15}$$

where ${I_{rms,PG}}^2$ is equal to the total summation of noise sources [77] as ${I_{rms,pg}}^2 = {I_{rms,shot}}^2 + {I_{rms,thermal}}^2 + \dots$. Analytical forms of the noise sources as described in the section of noise (section **2.4.4**).

2.4.2.5 The Noise Equivalent Power (*NEP*) and the Specific Detectivity (*D**)

The specific values of *SNR* depend both on the type of noise sources and on the power intensity of the targeted signal. $SNR_{power} = SNR_{current} = 1$ is attained at a specific optical power, which is defined as the noise equivalent power (*NEP*). One quantity related to *NEP* is the specific detectivity *D** [78], which normalizes *NEP* with respect to the area (*A*) of the OPD and the effective bandwidth (*B*) of the instruments involved in the measurement as

$$D^* = \frac{\sqrt{AB}}{NEP} \quad (16)$$

The specific detectivity is the ultimate metric that can be used to compare photodiode technologies. In the context of OPD, many disagree about how to define *NEP* and *D**, mainly regarding the omission of some noise sources dependent of frequency (Flicker noise). This issue has been recently pointed out in [52].

2.4.3 The Prince Equivalent Circuit Model for OPDs in the Steady State

The current-voltage (*I*-*V*) curve, which describes the different operation points of a device, is a consequence of the energetics, and in general of the physics in the system. **Figure 10.A** and **Figure 10.B** shows the current density vs. voltage curves for an OPD (dark and light condition, respectively) in linear and logarithmic scale. The yellow area highlights the sensing region, and the blue area highlights the power supply region. This latter region is helpful for the circuit modeling of OPD.

Figure 10.C presents the equivalent circuit typically used for organic solar cells (OSCs) [79], but it is extendable to OPD. In dark conditions (the black curves in **Figure 10**), the non-ideal single-diode equivalent circuit has four main parameters (Prince equivalent circuit model): the ideality factor *n*, the reverse saturation current density J_0, the series resistance R_S, and the shunt resistance R_P. A current density source J_{ph} is added to the circuit in the presence of light (the red curves in **Figure 10**) and it represents the

photogenerated current before parasitic effects. The circuit in **Figure 10.C** can be used to describe the photocurrent of the Prince model, J_{LIGHT_PM}, as:

$$J_{LIGHT\_PM} = \frac{1}{\frac{R_S}{R_P} + 1}\left[J_O\left(e^{\frac{V - R_S A J_{LIGHT\_PM}}{nV_T}} - 1\right) - \left(J_{ph} - \frac{V}{AR_P}\right)\right] \quad (17)$$

where A is the OPD area, V is the applied voltage to the OPD, and V_T is the thermal voltage defined by kT/q with k as the Boltzmann constant, T as the temperature, and q as the elementary charge of an electron. J_{DARK_PM} is obtained when $J_{ph} = 0$. Please note that from **Figure 10.C**, $J \rightarrow J_{LIGHT\_PM}$.

An ideal OPD is one in which $R_S \rightarrow 0$ and $R_P \rightarrow \infty$. In this case, the Prince model [80] becomes the Shockley model [81], which is an explicit equation, as

$$J_{LIGHT\_SM} = J_O\left(e^{\frac{V}{nV_T}} - 1\right) - J_{ph} \quad (18)$$

In this case, $J_{DARK\_SM} = 0$ when external bias is not applied ($V = 0$).

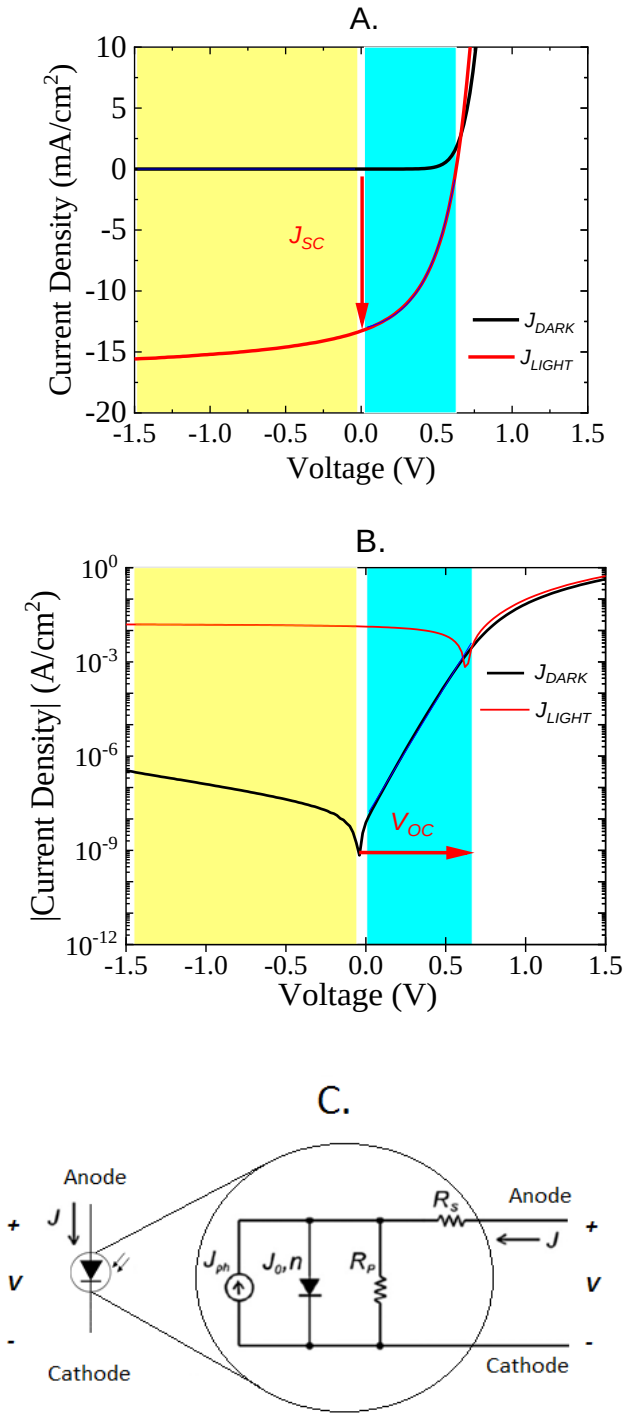

Figure 10. *J-V* curves of a PCE10:PC$_{71}$BM (*D*:*A*) OPD in the absence of a targeted signal (black) and in the presence of a targeted signal (red) and its equivale circuit. A. *J-V* curves in linear scale. B. *J-V* curves in logarithmic scale. C. The electrical symbol and the Prince equivalent circuit model of an OPD (adapted from [80]). Measurements were done at the Georgia Institute of Technology by the author of this dissertation.

2.4.4 Noise

Noise can be defined as any unwanted disturbance that obscures or interferes with a desired signal and noise mathematical formalisms to describe noise have been developed extensively [82-85]. In this dissertation, the main relevant results for the purpose of the discussion of results for OPDs are highlighted. The temporal "continuous current" $i(t)$ and the "discrete current" $i(m)$ will be treated as random variables that account not only for the measurable signal itself but also for its fluctuations (noise). Equivalent circuits, as the Shockley [81] and the Prince model [80] for average currents, will assist the description of the noise in photodiodes.

The random variables of interest (dark current I_{DARK}, photocurrent I_{LIGHT}, photogenerated current I_{PG}, etc.), are expected to have stationary and ergodic statistical properties. These are reasonable practical assumptions that simplify the analysis. In particular, the ergodic property allows to equal the averages of the random variable in ensembles (done for calculations in mathematical analysis and description) with the temporal averages of one entity of the ensemble (done for measurements in practical lab work).

2.4.4.1 Noise in Signals – Frequency Domain

The statistical properties above can be combined with the Fourier transform to evaluate mean square values (related to the noise magnitude) assisted by circuits theory. In

this direction, the photogenerated current $i_{PG}(t)$ is measured and constrained to a finite time interval for its Fourier transform to exist.

$$i_{PG}(t) \leftrightarrow \mathcal{I}_{PG}(f) \tag{19}$$

Once the Fourier transform of $i_{PG}(t)$, $\mathcal{I}_{PG}(f)$, is known, the power spectral density can be defined as

$$S_i(f) = \lim_{T\to\infty} \frac{1}{2T} \int_{-T}^{T} {\mathcal{I}_{PG}}^2(f)\, dt' = \langle {\mathcal{I}_{PG}}^2(f) \rangle \tag{20}$$

Then the power spectral density can be calculated from the time average of the squared Fourier transform of $i_{PG}(t)$. On the other hand, the variance $<{i_{PG}}^2(t)> = {I_{rms,pg}}^2$ can be calculated as

$$\langle {i_{PG}}^2(t) \rangle = {I_{rms,pg}}^2 = \int_{-\infty}^{\infty} S_i(f)\, df = \int_{-\infty}^{\infty} \langle {\mathcal{I}_{PG}}^2(f) \rangle\, df \tag{21}$$

This last equation suggests that the total area under the temporal ${i_{PG}}^2(t)$ signal is equal to the area of its power spectral density $S_i(f)$ in the frequency domain. This is consistent with the general power definitions of electrical circuits dissipated by an electrical resistance R_Ω in which $P(t) = R_\Omega i^2(t)$.

2.4.4.2 Noise in Coupling and/or Front-End Circuits – Frequency Domain

As current $i_{PG}(t)$ is measured through an electronic circuit (coupling and/or front-end circuit), this interaction will impact $i_{PG}(t)$. The instrument can be a simple load resistor which transform the photogenerated current into a voltage (making the output signal compatible with front end electronics), an electric network with two or more component (e.g., a parallel RC circuit) or a more complex electronic system such as an amplifier (it can contain many transistors).

RC Parallel Circuit – Transfer Function between Input Current and Output Current

As an example, let us consider a noiseless RC parallel circuit which transforms the photodiode's photogenerated $i_{PG}(t)$ current into a voltage measured at the resistor R_Ω. This photogenerated current in the frequency domain will be referred as $\mathcal{I}_{in}(f)$ and the output current and voltage will be referred as $\mathcal{I}_{out}(f)$ and $V_{out}(f)$, respectively. All these signals are assumed to be real. The first step is to correlate the input $\mathcal{I}_{in}(f)$ and output currents $\mathcal{I}_{out}(f)$ through a current divider

$$\mathcal{I}_{out}(f) = \frac{\frac{1}{j2\pi fC}}{R_\Omega + \frac{1}{j2\pi fC}}\mathcal{I}_{in}(f) = \frac{1}{j2\pi fCR_\Omega + 1}\mathcal{I}_{in}(f) \tag{22}$$

where $G_i(f) = (j\omega CR_\Omega + 1)^{-1}$

RC Parallel Circuit – Transfer Function between Input Current and Output Voltage

The current and voltage at the output (resistor) can be expressed as

$$\mathcal{I}_{out}(f) = \frac{V_{out}(f)}{R_{\Omega}} \tag{23}$$

The transfer function $G_{vi}(f)$ can be written as

$$\frac{V_{out}(f)}{I_{in}(f)} = G_{vi}(f) = \frac{R_{\Omega}}{j2\pi f R_{\Omega} C + 1} \tag{24}$$

to relate this expression with the noise, an equation can be written as

$$S_{v\_out}(f) = \langle {V_{out}}^2(f) \rangle \tag{25}$$

Relating $S_{v\_out}(f)$ to the transfer function $G_{vi}(f)$ originates a new equation as

$$S_{v\_out}(f) = |G_{vi}(f)|^2 \langle {\mathcal{I}_{in}}^2(f) \rangle \tag{26}$$

This last equation can be related to the spectral power density of the input

$$S_{v\_out}(f) = |G_{vi}(f)|^2 S_{i\_in}(f) \tag{27}$$

Taking the integral on both sides with respect to frequency

$$\langle {v_{out}}^2(t)\rangle = \int_{-\infty}^{\infty} \frac{{R_\Omega}^2}{(2\pi f)^2 {R_\Omega}^2 C^2 + 1} S_{i\_in}(f)\, df \tag{28}$$

Then if $i_{PG}(t)$ is known and its Fourier transform $\mathcal{I}_{in}(f)$ exists, $S_{i\_in}(f)$ can be calculated [see Eq. (20)]. The characteristics of $\langle {v_{out}}^2(t)\rangle$ will depend on the sources of noise associated to $i(t)$ and the frequency characteristics of the coupling and front-end circuits.

Effective Bandwidth

Even when coupling or front-end electronic components/circuits/systems (e.g., resistor, amplifier, measurement instrument, etc.), are idealized as noiseless circuits, they have a limited frequency response. This means that the signal and/or noise connected at the input will be attenuated at certain frequencies. In the example of the parallel RC circuit, let us consider the squared magnitude of the transfer function $G_i(f)$ between the $\mathcal{I}_{in}(f)$ and $\mathcal{I}_{out}(f)$

$$|G_i(f)|^2 = \frac{1}{(2\pi f C R_\Omega)^2 + 1} \tag{29}$$

From Eq. (29), the squared magnitude of $G_i(f)$ converges to zero for high frequencies, similar to the frequency response of a low-pass band filter. An important parameter that helps to identify the characteristics of transfer functions is the corner frequency, which is obtained when Eq. (29) is equal to 0.5. For the RC circuit described

previously, $f_c = 1/(2\pi C R_\Omega)$ and then, for higher frequency values than f_c, the square magnitude will be less than 0.5 till converge to zero.

Some noise sources have a frequency-independent behavior (e.g., white noise). This means that the noise will be constant at any frequency. When a signal carries this type of noise and interacts with coupling or front-end electronic components/circuits/systems (for example as the one in Eq. (29) when the output signal is a current or in Eq. (24) when output signal is voltage), the noise and the signal will be greater than zero only for the frequencies where the respective squared transfer function is greater than zero.

For the specific case of the noise current, Eq.(28) can be generalized depending on the type of output variable. For an output voltage

$$\langle {v_{out}}^2(t)\rangle = \int_{-\infty}^{\infty} |G_{vi}(f)|^2 S_{i\_in}(f)\, df \tag{30}$$

For an output current

$$\langle {i_{out}}^2(t)\rangle = \int_{-\infty}^{\infty} |G_{i}(f)|^2 S_{i\_in}(f)\, df \tag{31}$$

The squared transfer functions $|G_{vi}(f)|^2$and $|G_i(f)|^2$ can have relatively complex forms (e.g., trapezoid-like forms for many practical circuits). As white noise $S_{i\_in}(f)$ is expected to be a constant, it is possible to map the area under the squared transfer function $|G(f)|^2$ into a simple square with these features: 1) the height equal to the maximum value

of $|G(f)|^2$, G_{max}, and 2) a width B which is tuned for the area under the square to equal the area under the squared transfer function $|G(f)|^2$.

$$B = \frac{1}{|G_{max}|^2} \int_{-\infty}^{\infty} |G(f)|^2 \, df \tag{32}$$

where f_o is the frequency at which $G(f_o) = G_{max}$

2.4.4.3 White Sources of Noise

For a constant noise source, like white noise (e.g., thermal or shot noise), the noise current at the output can be calculated as

$$\langle {i_{out}}^2(t) \rangle = \left|G_{i,max}\right|^2 S_{i\_in}(f_o) B \tag{33}$$

where f_o is the frequency at which $G_i(f_o) = G_{i,max}$. Analogously, the noise voltage at the output can be calculated as

$$\langle {v_{out}}^2(t) \rangle = \left|G_{vi,max}\right|^2 S_{i\_in}(f_o) B \tag{34}$$

where f_o is the frequency which $G_{vi}(f_o) = G_{vi,max}$.

Thermal Noise

It has been shown that the spectral density $S_{i\_in,thermal}$ due to thermal noise can be expressed as a constant

$$S_{i,thermal} = \frac{4k_B T}{R_\Omega} \tag{35}$$

Thermal noise is present only in resistors and it is caused by vibration of charge carriers that have been thermally excited and that move in a Brownian fashion [83].

Thermal Noise - Resistor as Front-End Electronics

Then the standard deviation of $i_{out,thermal}$ due to thermal noise can be found from Eq. (33)

$$\langle {i_{out,thermal,R}}^2(t)\rangle = \left|G_{i,max}\right|^2 \frac{4k_B T}{R_\Omega} B = \frac{4k_B T}{R_\Omega} B \tag{36}$$

where $\left|G_{i,max}\right|^2 = 1$.

Similarly, standard deviation of $v_{out,thermal}$ due to thermal noise can be found using Eq. (34) and then

$$\langle {v_{out,thermal,R}}^2(t)\rangle = \left|G_{vi,max}\right|^2 \frac{4k_B T}{R_\Omega} B = 4k_B T R_\Omega B \tag{37}$$

where $G_{vi,max} = R_\Omega$

Thermal Noise - Parallel RC Circuit as Front-End Electronics

To find the standard deviation of $i_{out,thermal,RC}$, Eq. (29) is used in conjunction with Eq. (33)

$$\langle {i_{out,thermal,RC}}^2(t)\rangle = \left|G_{i,max}\right|^2 \frac{4k_BT}{R_\Omega} B \tag{38}$$

where $\left|G_{i,max}\right|^2$ is equal to 1. For a one-pole system, as the RC circuit, $B = \frac{\pi}{2} f_c = \frac{\pi}{2} \frac{1}{2\pi C R_\Omega}$, then Eq. (38)

$$\langle {i_{out,thermal,RC}}^2(t)\rangle = \frac{4k_BT}{R_\Omega} \frac{1}{4CR_\Omega} = \frac{k_BT}{4C{R_\Omega}^2} \tag{39}$$

Similarly, for G_{vi}, Eq. (24) can be used

$$\langle {v_{out,thermal,RC}}^2(t)\rangle = \left|G_{vi,max}\right|^2 \frac{4k_BT}{R_\Omega} B = 4k_BTR_\Omega B \tag{40}$$

where $\left|G_{vi,max}\right|^2$ is equal to ${R_\Omega}^2$. Taking $B = \frac{\pi}{2} f_c = \frac{\pi}{2} \frac{1}{2\pi C R_\Omega}$, it can be shown that

$$\langle {v_{out,thermal,RC}}^2(t)\rangle = \frac{kT}{C} \tag{41}$$

Shot Noise

The shot noise does not take place into resistors. Instead, this is related to random uncorrelated discrete events. For example, when current flows through a potential barrier [84]. For shot noise, the power frequency density can be expressed as

$$S_{i,shot} = 2q\langle i \rangle = 2qI \tag{42}$$

where q is the elementary charge and I is a continuous current flowing through the device. The number 2 in the equation is a consequence of the Nyquist sampling theorem. For photodiodes (using the Shockley [81] model rather than the Prince [80] one), this current is actually the sum of two contributions: 1) current in equilibrium ($I_{eq} = I_o$) which is the reverse saturation current and 2) current out of equilibrium ($I_{non-eq} = I_{LIGHT\_SM} + I_o$). For photodiodes then the power frequency density

$$S_{i,shot} = 2q\left(I_{eq} + I_{non-eq}\right) = 2qI_{LIGHT\_SM} + 4qI_o \tag{43}$$

2.4.4.4 Other Sources of Noise

Sources of noise which are dependent on frequency are also present in photodiodes. Specially at low frequencies, Flicker noise is present and can be dominant. Some previous work associates this source of noise to traps and defects [84]. The Flicker noise is not connected directly related with the presented circuit models, so it is included through $S_{i,others}$

$$I_{rms,pg}{}^2 = (S_{i,thermal} + S_{i,shot} + \sum S_{i,others})B \quad (44)$$

CHAPTER 3. METHODS FOR THE FABRICATION AND CHARACTERIZATION OF PCE10:$PC_{71}BM$-BASED ORGANIC PHOTODIODES

This chapter is divided into three sections. **Section 3.1** summarizes the equipment used to characterize optical properties of organic semiconductor materials like the absorption, as well as physical properties such as the thickness and the work function of the metallic and semiconductor films. **Section 3.2** describes the materials, equipment and processes involved in the fabrication of NIR OPDs reported in this dissertation. **Section 3.3** describes the probe stations and procedures to characterize NIR OPDs discussed along this dissertation.

3.1 Characterization of Materials

For the characterization of materials, standard equipment is used, and then only relevant aspects will be discussed regarding its operation and usage. References with more detailed information on equipment's usage and capabilities are provided along the text.

3.1.1 Optical Absorption and Thickness Estimation through Ellipsometry

Equipment: A spectroscopic ellipsometer (Woollam M-2000) [86] is used to measure the optical properties of organic films at wavelengths that range between 245 nm and 1690 nm. The ellipsometer is equipped with two robotic arms: One of them possesses the optical sources that enable to tune the wavelength of the light beam, whereas the other one has the photodetection system to measure the optical intensity of these light sources and their polarization features as a function of the wavelength. The robotic arms can be controlled so various incident light angles can be attained, from a perpendicular incidence in the film to evaluate the transmission through the organic film (and then the material absorption), up to an oblique incidence to evaluate the reflection of the organic film as a function of the wavelength and the incident angle.

Principle of Operation – Perpendicular Incidence to Determine the Absorption of Organic Films: The absorption of a material depends on its chemical composition as well as on its thickness, among other features. A light beam with perpendicular incidence in the sample can be used to quantify the amount of optical power that is transmitted through the film as a function of wavelength. At a given wavelength, the absorption of the film is approximated as a difference between the optical power measured in absence of the organic film (first measurement), and the optical power transmitted through the organic film (second measurement). Reflection is then typically neglected, and transmission and absorption are reported in percentile form.

Procedure – Perpendicular Incidence to Determine the Absorption of Organic Films: Organic films are deposited on glass substrates. The robotic arms are placed in a reference position for the sensor to receive the maximum optical power from the source. A first measurement is done in absence of the organic film to establish the optical power at each wavelength. A second measurement of the optical power is done in presence of the organic film deposited in substrate, which is placed in a holder. Different regions in the film can be chosen to verify repeatability of the measurement.

Principle of Operation – Oblique Incidence to Estimate the Thickness and Optical Constants of Organic Films: This equipment is also used to estimate the thickness, the optical constants (refraction index and absorption), and the roughness of organic films. This is done through shinning a light beam on the organic film at different incident angles and measuring the polarization parameters (Psi and Delta) of the reflected beam from the film [87-89]. A mathematical model (e.g., the Cauchy model) enables to correlate the measured polarization parameters with an estimation of the thickness, roughness and optical constants of the organic films through a fitting process in which the Levenberg-Marquardt algorithm is used as an optimization path to minimize the error between the model and the measured quantities.

Principle of Operation – Oblique Incidence to Estimate the Thickness and Optical Constants of Organic Films: Organic films are deposited in a non-fully transparent known substrate (e.g., ITO or Si), whose thickness and optical constants are previously known or estimated. The sample and the robotic arms are positioned to attain incident angles of 65º, 70º, and 75º. After data is recorded for each angle, the fitting process is done offline by

selecting a simple model (e.g., the Cauchy model) and integrating the different layers (e.g., substrate and air) involved. If convergence is not attained, a more complex model is used.

3.1.2 Thickness Measurement with Profilometry

Equipment: Equipment required to measure the thickness of organic films is a profilometer (Veeco Detktak 150) [90].

Principle of Operation: Typically, a diamond-based stylus profilometer is a type of instrument used in surface metrology to measure the thickness and roughness of a film. In contrast to optical profilometry, stylus profilometry enables the measurement of films whose optical characteristics (e.g., transparency) may cause errors in the measurement. The resolution is defined by the stylus size, whose tip is approximately 10 μm of radius. Although a higher resolution can be achieved through smaller tips, this can be detrimental to the film as a smaller area would increase the pressure on the film. The stylus is mechanically coupled to a displacement sensor known as a linear variable differential transformer. This sensor generates an analogous electrical signal as a function of the vertical displacement (related to the topography of the sample's surface) of the stylus, when it moves along a linear trajectory on the film. The analogous signal is transformed into a digital signal, which is recorded and visualized in a computer to extract the topographic information of the measured sample [91, 92].

Procedure: To measure the thickness of an organic film, which has been deposited on a glass substrate, a trench is created by scratching the film with a scalpel blade. The

profilometer stylus is driven to mechanically contact the film surface and positioned few millimeters away from the trench. An optical microscope is used to assist the positioning of the tip on the surface. A scan routine is programmed for the stylus to run over few millimeters in a trajectory perpendicular to the direction of the trench and record the data obtained from the position sensor. For this, in the software the "hills and valleys mode" is selected, and some parameters are defined: stylus force is 3 mg, measurement range is 6.5 μm, and length and duration are tuned according to the trench obtained (width). Typically, five scan trajectories perpendicular to the direction of the trench are run to cover different zones of the film and confirm repeatability of the thickness measurement.

3.1.3 Work Function Measurements of Metallic and Organic Films with a Kelvin Probe

Equipment: Equipment required to measure the WF of semiconducting and metallic films is a Kelvin Probe (Besocke) [93].

Principle of Operation: The principle of the WF measurement is illustrated in **Figure 11**. When the sample is contacted to the Kelvin probe (**Figure 11.B**), electrons in the material with lower WF (for this example the sample) are be transferred to the material with higher WF (for this example the tip of the Kelvin probe), generating a charge distribution as the one in a charged capacitor. This generates an internal electric field (**Figure 11.C**) to which a voltage can be associated and it is typically named as the contact potential difference (V_{CPD}). This voltage is related to the difference of the WF of the materials.

The contact potential difference (V_{CPD}) can be measured indirectly through changes in the capacitance, which is formed between the probe and the sample. If an external voltage V_{BIAS} is applied, then the charge stored Q will depend on the capacitance C as

$$Q = CV \tag{45}$$

where $V = V_{CPD} + V_{BIAS}$. If a piezoelectric is connected to the tip of the Kelvin probe, a current i will be generated, and its temporal dependence will be related to the driving source of the piezoelectric element. As the voltage V does not depend on time, the current generated through the capacitor

$$i = \frac{dQ}{dt} = V\frac{dC}{dt} \tag{46}$$

This current can be electrically sensed and for the specific case in which $V = 0$ ($V_{BIAS} = -V_{CPD}$), the current will be zero (**Figure 11.D**) and the work function difference $\Delta WF = qV_{CPD}$, where q is the fundamental charge of the electron.

Procedure - Calibration: To account for deviations from ideal measurement conditions, the WF of a highly ordered pyrolytic graphite (HOPG, SPI supplies [94], grade ZYH, 12 mm × 12 mm × 2 mm), whose value is known to be 4.6 eV, is measured in four different points. Any offset from the WF nominal value of HOPG is to correct value from the WF value measured from a metallic film or the organic film (deposited on top of a metallic film). This correction is done by adding or subtracting the offset obtained from HOPG measurement to the WF measurement of the sample.

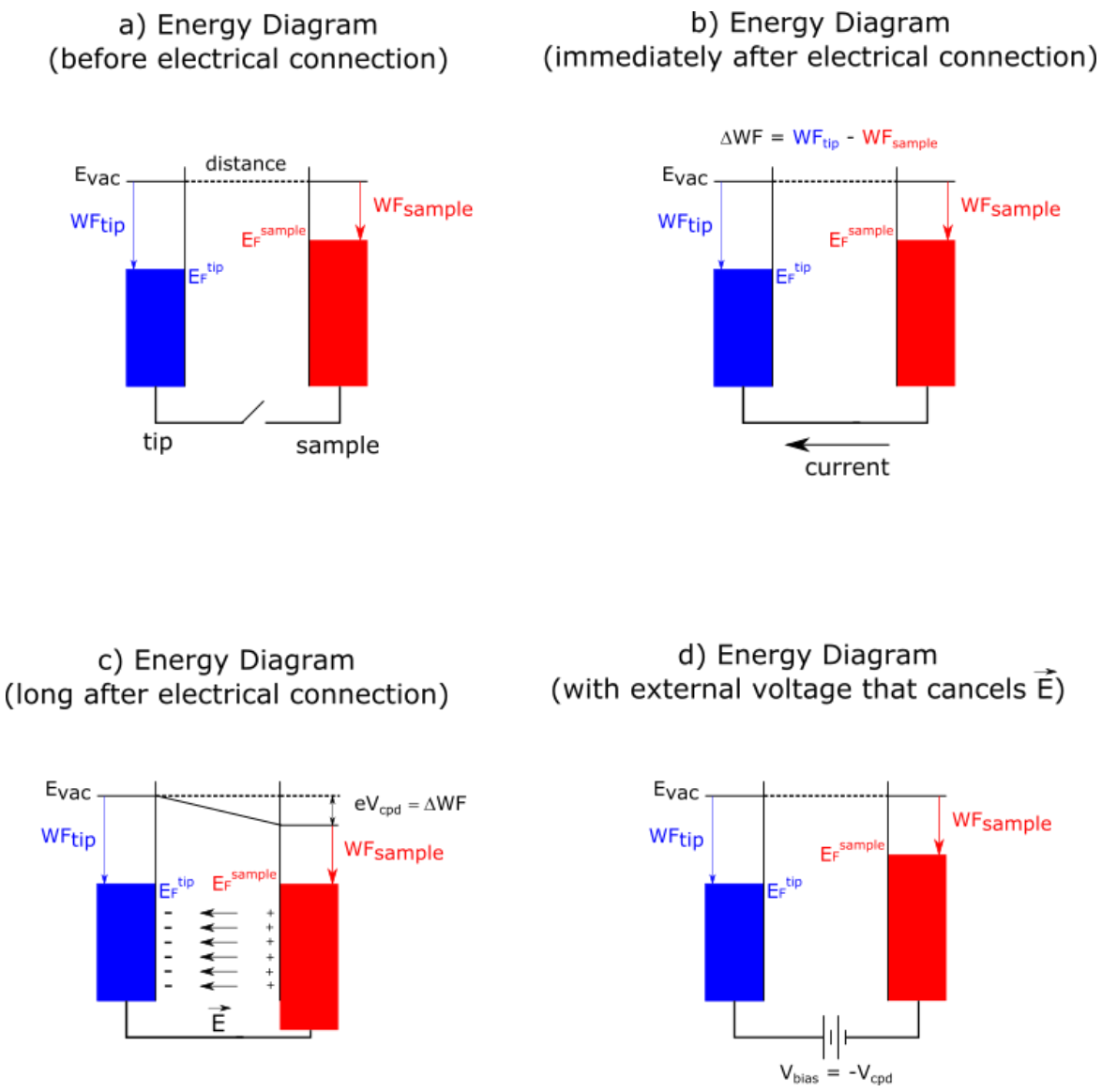

Figure 11. A. Working principle of the Kelvin Probe (KP) when the WF of the sample is lower than the WF in the tip of the KP. Energy diagram: A) Before the electric contact, B) immediately after the contact, C) in steady state when the electric field is developed and the contact potential difference is established, D) when an external voltage is applied to cancel the electric field developed by the charge transfer between the sample and the tip.

Procedure - WF Measurement: This measurement is also done by probing in at least four points and a statistic average is calculated to report the WF of the material with its respective standard deviation after including the correction (calibration with HOPG) in the measurement.

3.2 Fabrication of Organic Photodiodes (OPDs)

The fabrication of devices (five OPD) is made on top of glass substrates, whose size is 1.0" x 1.0" (6.4 cm^2). The OPD area (0.1 cm^2) is defined by the intersection of the electron-collecting electrode (ECE), the photoactive layer (PAL), and the hole-collecting electrode (HCE).

Figure 12.A shows a picture of an actual substrate (top view) which contains five OPD, with their respective areas. **Figure 12.B** shows the cross section of a single OPD, displaying the specific materials of the electrodes and their respective thicknesses. The specific PAL thickness is reported according to the experimental condition presented.

The steps taken for the fabrication of the ECE, PAL and HCE, and ultimately OPD, are described in the following subsections. Highlights of the involved equipment (e.g., spin coater, atomic layer deposition or ALD, etc.) are presented along with each fabrication step.

\

A. TOP VIEW (SUBSTRATE)

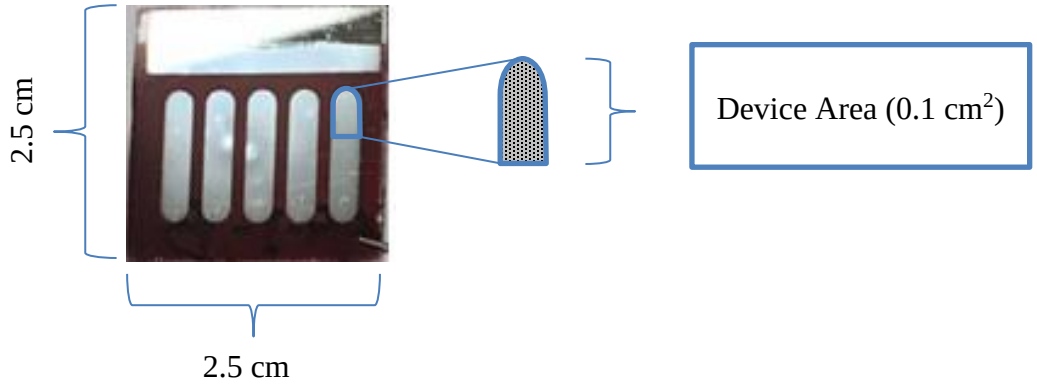

B. CROSS-SECTION VIEW (DEVICE)

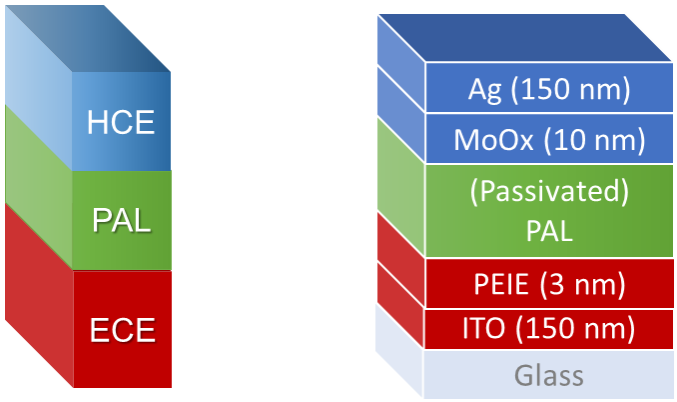

Figure 12. A. Top view of the substrate containing five OPD. B. Cross-section view of OPD.

3.2.1 Electron-Collecting Electrode (ECE)

Equipment: The equipment required for cleaning the substrates is a Sonicator (Branson 5510) [95]. A spin coater (Laurell WS-400-6NPP-LITE) [96] sitting in air is used for depositing the polymer to modify the WF. For thermal annealing of these layers, standards hot plates (VWR International [97]) are used.

Materials: Pre-patterned ITO substrates (MSE Supplies) [98], whose size are 1" x 1" with an ITO area of 1" x 0.5", and a sheet resistance of 12 – 15 Ω/□, are used as starting point of the fabrication.

The (polymer-based) work function modifier is fabricated by using polyethylenimine (see **Figure 13.A**) or PEIE, 80% ethoxylated (Sigma Aldrich [57], product # 306185), and a 2-methoxyethanol or 2ME (see **Figure 13.B**) solvent (anhydrous, 99.8% purity, Sigma Aldrich [57], product # 284467). Materials and solvents were used as received.

3.2.1.1 Substrate

Cleaning: Pre-patterned ITO substrates were cleaned through sonication in four sequential baths (liquinox, water, acetone, and two-propanol) at 40 °C each for 40 min. The WF of ITO was measured as 4.7 eV in a non-controlled environment.

3.2.1.2 PEIE-based Work Function Modifier

Preparation of Solutions: PEIE, which was originally diluted in water at 37 wt.% concentration, was further diluted in a 2ME solvent to attain a concentration of 0.1 wt.% and left stirring at 500 rpm for 12 h.

Coating, Drying, and WF Measurements: The diluted solution was then filtered through a 0.2 μm polytetrafluoroethylene (PFTE) filter and spun onto the etched ITO substrates at 500 rpm for 1 min. The coated ITO substrates were then thermally annealed at 100 °C for 10 min. The preparation of the PEIE solution, the spin coating, and the WF measurements were done in a non-controlled environment. The WF of ITO/PEIE was measured as 3.9 eV.

A. **B.**

Figure 13. Chemical structures for PEIE-based work function modifier [99]: A. PEIE (Polyethylenimine). B. 2ME (2-Methoxyethanol).

3.2.2 Photoactive Layer (PAL)

Equipment: Equipment required to form organic films is a spin coater (Headway Research, Inc. [100]) in a GB filled with nitrogen. For thermal annealing, standards hot plates (VWR International [97]) are required.

Materials: Photoactive materials required are the polymer PCE 10 (Poly[4,8-bis(5-(2-ethylhexyl)thiophen-2-yl)benzo[1,2-b;4,5-b']dithiophene-2,6-diyl-alt-(4-(2-ethylhexyl)-3-fluorothieno[3,4-b]thiophene-)-2-carboxylate-2-6-diyl)), also known as PTB7-Th, PBDTTT-EFT, or PBDTT-FTTE, from Ossila [53] (see **Figure 14.A**); and the fullerene $PC_{71}BM$ ([6,6]-phenyl C71-butyric acid methyl ester ([70]PCBM)) from Solenne [101] (see **Figure 14.B**). Materials were used as received.

A. **B.**

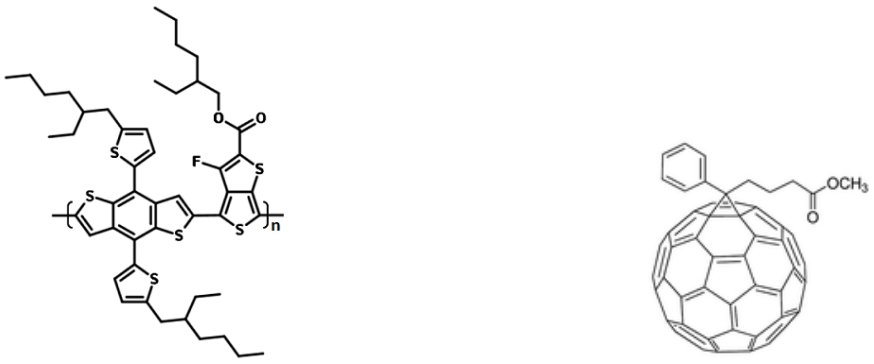

Figure 14. Chemical structures of the donor and the acceptor materials [60, 62]: A. PCE10. B. $PC_{71}BM$.

A. **B.** **C.**

Figure 15. Chemical structures of the solvent, the additive, and the drier [60, 62]: A. CB (Chlorobenzene). B. DIO (1,8-Diiodooctane). C. Methanol

In order to process the photoactive materials, the chlorobenzene (CBE) solvent (see **Figure 15.A**), Sigma Aldrich [57] product # 284513; the 1,8-Diiodooctane (DIO) additive (see **Figure 15.B**), Sigma Aldrich [57] product # 280885; and the methyl alcohol or methanol drier (see **Figure 15.C**), Sigma Aldrich [57] product # 322415, were used as received.

Preparation of Solutions: To form the PAL layer, PCE10 donor polymer was mixed with $PC_{71}BM$ acceptor fullerene and dissolved in CBE with a DIO additive with a ratio CBE:DIO = 97:3 to attain six concentrations: 15, 25, 35, 50, 70, and 100 mg/mL. The D:A composition was 1:1.5 for all the concentrations. The solutions were left stirring for 12 h at 500 rpm on a hot plate at 70 °C inside a N_2-filled glovebox.

Coating and Drying: PAL solution was dynamically spun on the substrates for 30 s at 2000 rpm in a N_2-filled glovebox. After a 5 s pause, each substrate was dried by the immediate deposition of methanol on the formed layer (post-additive soaking) in a second step of spin coating at 4000 rpm for 30 s. Substrates were left under vacuum for further drying for 12 h. A fraction of the covered ITO was exposed by being wiped with CBE.

3.2.3 ALD-based Passivation of the PAL by using Atomic Layer Deposition (ALD) at Low Temperatures

Equipment: Equipment required for the ALD passivation with Al_2O_3 is the Savannah S200 ALD system (Veeco / Ultratech / Cambridge Nanotech Inc.[102]).

Materials: The metal-organic molecule trimethylaluminum (TMA), also known as aluminum trimethanide (Sigma Aldrich [57], product # 663301), was used as received in the Savannah S200 ALD system. This is denominated the TMA precursor (see **Figure 16**).

Principle of Operation: The standard ALD process consists of the chemical reaction between the TMA precursor and the water precursor which are carried by an inert gas (N_2) towards a chamber that facilitates the chemical reaction. The description below assumes a surface with OH groups present at the surface (see **Figure 17.A**).

- In the first step, the TMA precursor flows towards the chamber (see **Figure 17.B**), reacting with the OH groups: H atoms are released from the surface generating a chemical bond with some the methyl groups, initially bounded to the TMA precursor and then released from the Al atom, forming methane (CH_4) as a chemical product. Al atom from the TMA precursor forms a chemical bond with one or two of the O atoms at the surface.

- In the second step, a N_2 purging takes place removing the methane (CH_4) molecules (not shown) generated during the chemical reaction and the TMA precursors that did not participate in any chemical reaction. A pictorial

representation of the materials surface after the purging is shown in **Figure 17.C**.

- In the third step, the water precursor is injected to the chamber (see **Figure 17.D**). In this step, the water molecules react with the methyl (CH_3) groups still bounded to the Al atoms, substituting CH_3 groups with an OH groups. Methane (CH_4) is generated as the product of the chemical reaction.
- In the fourth step, a new N_2 purging is done to extract the methane generated during the chemical reaction and the water precursors, which did not react. A pictorial representation of the materials surface after the purging is shown in **Figure 17.E**.

This whole process is defined as an ALD cycle and can be repeated to grow the number of layers of Al_2O_3 desired with almost atomic precision at sub nanometric scales (approx. 100 pm per cycle).

Procedure: Samples were transferred from a N_2-filled glovebox to the ALD equipment for Al_2O_3 passivation. In this dissertation, 1, 5, 10, 20 and 30 ALD cycles were used as part of the optimization process. The standard protocol for Al_2O_3 deposition was modified from 100 °C to 75 °C as the performance of PCE10:PC_{71}BM devices decreases with temperature.

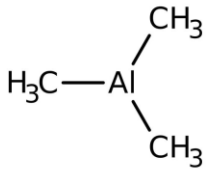

Figure 16. Chemical structures of the precursor trimethylaluminum (TMA) involved in the atomic layer deposition (ALD) process.

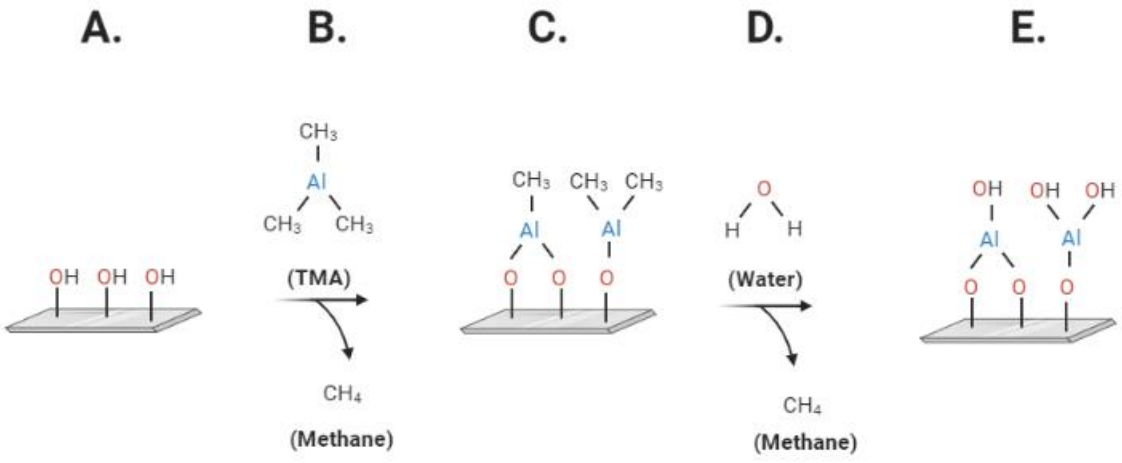

Figure 17. Steps of an ALD cycle.

3.2.4 Hole-Collecting Electrode (HCE)

Materials: Materials used as received for the HCE are the metal oxide, molybdenum oxide (MoO_x), Fisher Scientific [55], Molybdenum (VI) Oxide, Puratronic ®, 99.9995% purity, product # 12930); and the metal, silver or Ag (Kurt J. Lesker [103], product # EVMAG40QXQ-B).

Equipment: Equipment required is the SPECTROS [104] system (Kurt J. Lesker [103]) for physical (thermal) vapor deposition of HCE is available inside a N_2-filled glove box (GB) from MBraun Company [105]. This is to avoid the degradation of the material during the depositions of the HCE.

Shadow masks also are available to define the areas of metal deposition. They were previously designed by a computer-assisted tool and cut from a molybdenum-based alloy by using a high-power IR laser with a beam size of about 50 μm. The openings defined 5 rectangular shapes with rounded corners for the HCE to contact the PAL.

Deposition of HCE through thermal evaporation: The (ALD-passivated) ECE/PAL substrates were transferred back to a N_2-filled GB. They were fixed in a sample holder with capacity for nine substrates. To pattern the electrodes, substrates were covered with a shadow mask and loaded into a Spectros system to deposit the HCE. A MoO_x film with a thickness of 10 nm and an Ag film with a thickness of 100 nm were deposited sequentially at a pressure less than 10^{-7} Torr through physical vapor deposition. The deposition rate was monitored by a sensor based on a standard quartz crystal. At the end of the deposition, the substrates were unloaded and transfer to the respective probe stations to characterize the performance of the fabricated OPD.

3.3 Characterization of Devices

Data acquisition is done through GPIB communication and LabVIEW software (National Instruments [106]) unless otherwise specified. Benchmark is done with Hamamatsu [107] Si photodiodes: S1133-01 [1] and S2386-44K [2] with NIR response; and S1133 [1] with visible response. OPDs are measured using a sample holder with triaxial connections to reduce the noise related to connections. Unless otherwise specified, two or three substrates per experimental condition are used to evaluate the repeatability in the measurements on a total of 10 to 15 devices/experiment.

3.3.1 J-V Curves under Dark Condition

Equipment: Equipment required to measure currents in the pA and fA regime is an electrometer (Keithley, 6430 [108]) or more generally known as a source monitor/measurement unit (SMU). The scheme of the experimental setup is presented in **Figure 18.**

Principle of Operation: A simplified schematic of an SMU is presented in **Figure 19**. For the purpose of this dissertation, the voltage source is chosen as the excitation of the device under test (DUT) and the current meter is used to measure the current flowing through the DUT as a response to the excitation. It should be noted that even when there is no excitation of the DUT through an external voltage, current can be generated by other sources such as thermal excitations, optical sources, etc. For the connections between the SMU and the DUT, triaxial cables are used. This type of cables enables measurements it

the pA and fA range. In contrast to coaxial cables which contains two concentric conductors (the central conductor for the signal, typically known as high or force and the external conductor typically known as low or shield for the ground reference), the triaxial cable contains three concentric conductors (guard, high or force, and low or shield). This third cable (guard), located between high and low conductors is used set to a high voltage to minimize current losses between the high and low conductors and then signal is preserved from the DUT to the SMU.

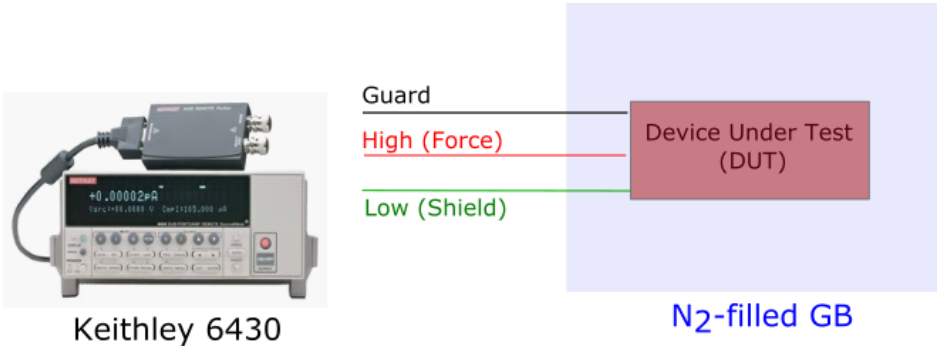

Figure 18. Scheme of experimental setup. On the left, an SMU (Electrometer) and on the right the device under test (DUT) which is inside a N_2-filled GB. Connections are done through triaxial cables.

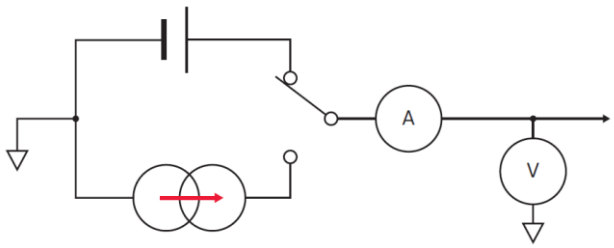

Figure 19. Simplified scheme of an SMU. DUT is connected to the most right of the circuit. Adapted from [109].

Table 5. Characterization of OPDs: Magnitude of the applied voltage and its duration in time.

Voltage (V)	Time (min)	Voltage (V)	Time (min)	Voltage (V)	Time (min)	Voltage (V)	Time (min)
1.5	3	0.4	0.25	0	1	-0.7	0.25
1.4	0.5	0.3	0.25	-0.0025	1	-0.8	0.25
1.3	0.25	0.2	0.25	-0.005	0.5	-0.9	0.25
1.2	0.25	0.1	0.25	-0.01	0.5	-1	0.25
1.1	0.25	0.075	0.25	-0.05	0.25	-1.1	0.25
1	0.25	0.05	0.25	-0.1	0.25	-1.2	0.25
0.9	0.25	0.025	0.5	-0.2	0.25	-1.3	0.25
0.8	0.25	0.02	0.5	-0.3	0.25	-1.4	0.25
0.7	0.25	0.01	0.5	-0.4	0.25	-1.5	0.25
0.6	0.25	0.005	1	-0.5	0.25		
0.5	0.25	0.0025	1	-0.6	0.25		

Procedure: Measurements are made inside a nitrogen-filled glovebox. Range of voltages is between -1.5 V and 1.5 V and scan is done from forward bias to reverse bias. The current measurements are done and recorded every 0.01 min. The time spent at each voltage value to attain steady condition for the current is presented in **Table 5**.

3.3.2 Responsivity as a Function of Wavelength

Equipment: Pieces of equipment required are a laser-driven light source (Energetiq EQ-99X [110]) coupled to a monochromator (CVI Spectral Products CM110 [111]), optical filters (Newport [112] FSR-GG400 in the 400 nm - 700 nm range, FSR-RG610 in the 700 nm - 1100 nm range), and a reference diode (Hamamatsu S2386-44K [107], [2]). For the measurement of current in this setup, an electrometer (Keithley 6517A [113]) is required to measure the current flowing through the DUT and a SMU (Keithley 2400 [114]) for the measurement of the current flowing through the reference diode. For calibration

purposes, an optical power meter (Nova II – Ophir photonics [115]) is used to measure the optical intensity at the position of the DUT.

Principle of Operation: The light beam from laser-driven light source is coupled to a monochromator. The monochromator is controlled from a computer to select a specific wavelength from the laser-driven light source. The monochromatic light beam is split so one of the light beams reaches position of the DUT and the second light beam reaches a reference diode. Experimental setup is shown in **Figure 20**.

The measurement is done in three different ranges: UV range (300 nm – 400 nm), visible range (400 nm – 700 nm), and near-infrared range (700 nm – 1100 nm). Depending on the range of measurement (UV, visible, and near-infrared), a filter is used to avoid that overtones from the monochromator generate any additional current. The UV range does not require any filter. The visible range requires the FSR-GG400 filter. The near-infrared range needs an FSR-RG610.

Under calibration mode, the optical power meter is placed in the DUT position. The measured optical power as a function of wavelength is recorded (see **Figure 21**) and correlated to the current measured by the reference diode. Under measurement mode, the OPD is placed in the DUT position. To obtain the responsivity at a given wavelength, the current measured at the DUT is correlated to the optical power through the current measured in the reference diode.

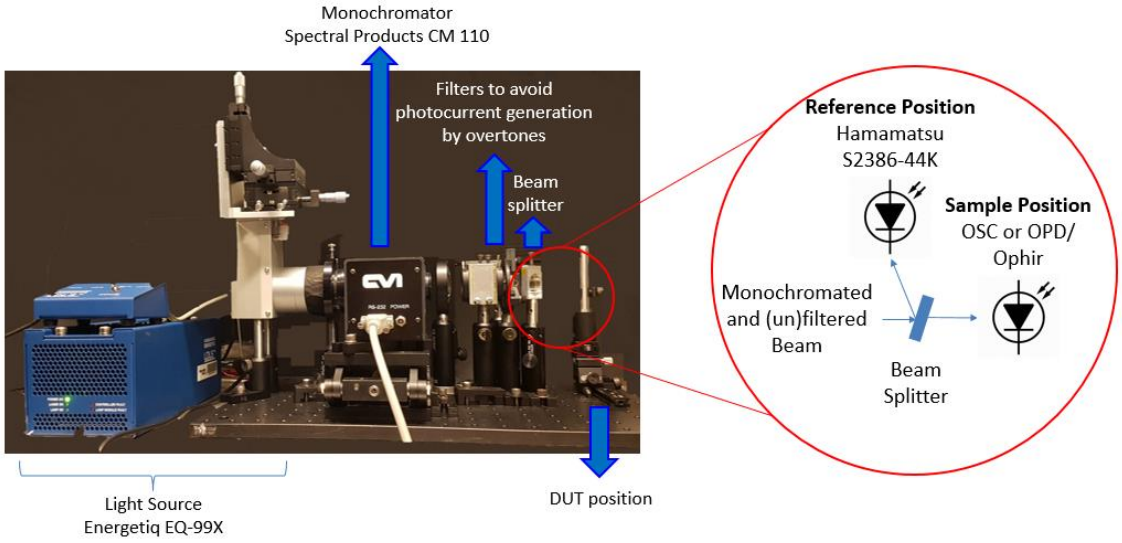

Figure 20. Experimental setup to measure responsivity. The light source is located to the most left of the picture. DUT is located to the most right of the picture.

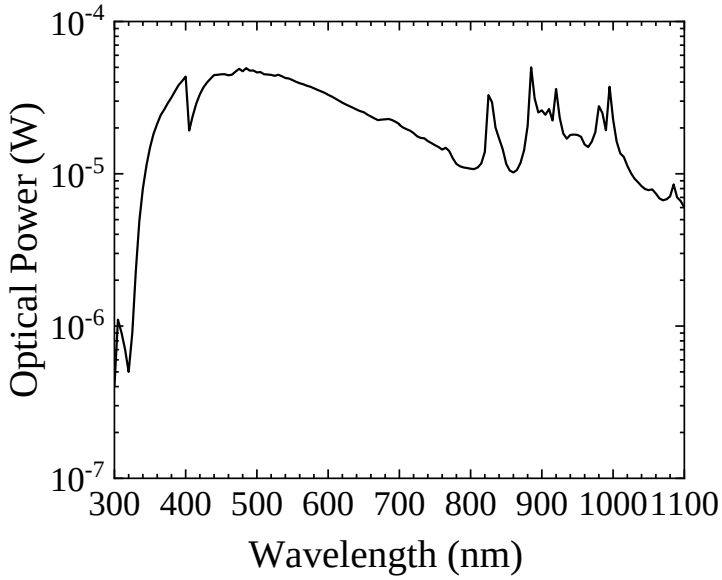

Figure 21. Optical power measured by an optical meter (Nova II – Ophir photonics [115]). Measurements were done at the Georgia Institute of Technology by the author of this dissertation.

Procedure: The laser-driven light source is turned on for 10 minutes before calibration and/or measurement to ensure stability in the light source. The DUT is placed at a distance in which the beam of light illuminates the area of the device. The scan of the wavelength range is done every 5 nm. At each wavelength selected, the current measured in the DUT is recorded after six seconds (for the current to reach steady state). The value of the current measured (after subtraction of the current under dark condition) is divided by the optical power. This optical power is estimated from the current measured in the reference diode and the correlation to the optical power measured during the calibration step.

3.3.3 Light Intensity Experiments at a Fixed Wavelength to Measure Responsivity, SNR, NEP and Detectivity

Equipment: Pieces of equipment required are light sources: an LED (Thor Labs Inc. ML735L3 [116]), which has a nominal wavelength of 735 nm, is used for the characterization of OPDs in the NIR region of the electromagnetic spectrum; a laser, which as a nominal wavelength of 653 nm, is used for the characterization in the visible region of the electromagnetic spectrum. A DC source (Agilent E3647A [117]) is used to drive the light sources. A neutral density optical filter (ND4) is used to excite the OPD at low optical intensities (< 100 pW). For calibration purposes, an optical power meter (Nova II – Ophir photonics [115]) is used to measure the optical intensity at the position of the DUT.

For the measurement of current flowing through the OPD, an electrometer (Keithley, 6430 [108]) is used as the instrument of measurement. Triaxial cables are used

to connect the electrometer with the DUT in order to be able to measure the low current flowing through the device, which is generated at low optical intensities as well as to obtain the noise current.

Principle of Operation: The main purpose of the experimental setup is to identify the optical power in which the current photogenerated by the OPD (average of the measured current) equals the value of the noise current (rms value of the measured current). The optical signal received at the DUT depends on the voltage applied to the light source (LED or LASER) and on the distance existing between the light source and the DUT. Therefore, the alignment and the distance between the position of the light source and the position of the DUT (OPD or optical meter) should be consistent during the calibration and the measurement itself (see **Figure 22**).

Procedure: For the calibration of the experimental setup, the light source is mechanically coupled to the optical meter then the separation distance is 1 cm. The scan of the optical power starts from high optical intensities to low optical intensities (voltage step of 0.1 V) and six seconds are given for the value of the optical signal to stabilize. Measurement is repeated twice, and the optical intensities are recorded as function of the applied voltage to the light source: the first one without an ND4 filter and the second one with the ND4 filter between the optical source and the optical meter. This is done to obtain the exact value of the optical attenuation of the filter. This value is used to estimate the optical power at very low intensities (beyond the scope of the optical meter).

For the measurement of the DUT, first, the responsivity at high optical intensities is obtained from the responsivity experimental setup described in the previous section. The

light source (LED or LASER) is set up at its higher optical intensity (typically a measured optical intensity is higher than 1 μW) with the highest voltage possible applied to the optical source. The light source and the DUT are separated by 1 cm of distance. Then, the alignment between the optical source and the DUT is adjusted for this value to match the value obtained from the ratio between the optical power (previously measured during the calibration and correlated to the voltage applied to the light source) and the measured current. After this, the optical intensity is decreased at the same conditions (voltage step and stabilization times) during the calibration till the light source is completely off.

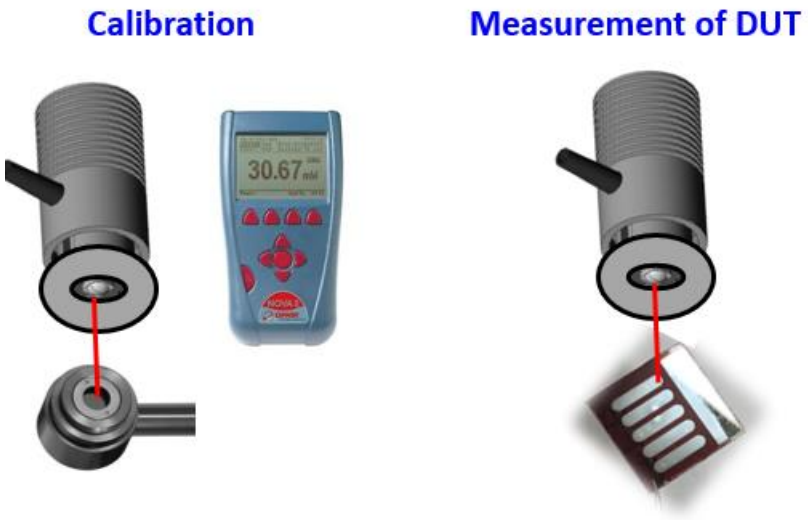

Figure 22. Setup for light-intensity experiments.

CHAPTER 4. RESULTS OF ORGANIC PHOTODIODES WITH NEAR-INFRARED RESPONSE BASED ON PCE10:$PC_{71}BM$

In this chapter, the main findings originated from this research are presented. **Section 4.1** summarizes simulations of current density–voltage curves (*J–V* curves) and open-circuit voltage–short-circuit current density curves (V_{OC}–J_{SC} curves) as a function of the electrical parameters (reverse saturation current J_0, ideality factor *n*, series resistance R_S, and shunt resistance R_P) of the Shockley [81] and Prince [80] models. Evaluation is done under dark and illumination conditions. The exploration of the illumination conditions is done through the variation of the photogenerated current density J_{ph} (before parasitic effects). The impact of all these parameters on the shot and thermal noise is also evaluated by correlating the electrical parameters of the electrical models to the analytical expressions of the white noise (thermal and shot noise), which are a function of these electrical parameters.

Section 4.2 presents the design approach 1 in which the thickness of the photoactive layer (PAL) is increased to reduce the measured RMS noise current (I_{rms}). Under this approach, the correlation between the experimental data (measured *J-V* and V_{OC}-J_{SC} curves) and the Prince model show that R_S and R_P are increased as the PAL thickness increases. The simulations and measurements in this section also suggest that J_{ph} is decreased for wavelengths in the visible range (400 nm – 700 nm) of the electromagnetic spectrum as the PAL thickness increases. For a specific PAL thickness of 1150 nm, OPDs with a narrowband responsivity in the near-infrared (NIR) region (up to a wavelength of 850 nm) are demonstrated. This approach shows its effectiveness in reducing the noise levels for

two types of thick PCE10:$PC_{71}BM$ OPDs (PAL thicknesses of 700 nm and 1150 nm). The RMS noise values attained by these thick PCE10:$PC_{71}BM$ OPDs are comparable to state-of-the-art OPDs based on P3HT:ICBA [5], which have responsivity in the visible range only (up to 650 nm). Therefore, thick PCE10:$PC_{71}BM$ OPDs, especially with PAL thickness of 1150 nm, can be an alternative used for the detection of quasi-monochromatic NIR signals (λ < 850 nm) by exploiting its narrowband feature. However, for the detection of broadband signals that include both the visible region and part of the NIR region, the lower responsivity values of thick PCE10:$PC_{71}BM$ OPDs compared to P3HT:ICBA OPDs might not offer a significantly advantage.

Lastly, **Section 4.3** presents the design approach 2 in which a passivation of the PAL is done through the atomic-layer deposition (ALD) of the H_2O and trimethylaluminum (TMA) precursors at 75 °C. The proposed passivation procedure is then compatible with materials that cannot be processed at higher temperatures (i.e., T > 75 °C) because of the degradation of the device's performance [65]. It is demonstrated that passivated PCE10:$PC_{71}BM$ OPDs with a specific PAL thickness of 170 nm can attain measured RMS noise current I_{rms} values with one order of magnitude lower than reference PCE10:$PC_{71}BM$ OPDs with the same PAL thickness. Furthermore, I_{rms} values of passivated PCE10:$PC_{71}BM$ OPDs (approach 2) are comparable to thick PCE10:$PC_{71}BM$ OPDs (approach 1). Nevertheless, the responsivity values of passivated PCE10:$PC_{71}BM$ OPDs (approach 2) are higher than thick PCE10:$PC_{71}BM$ OPDs (approach 1), especially in the visible range. This approach can be helpful then to detect broadband signals which have spectral components not only in the visible region, but also in the NIR region (up to 850 nm).

4.1 Simulation using the Equivalent Circuit

In addition to the electrical parameters (J_{ph}, J_0, n, R_P, and R_S) of the Prince model [80], for the discussion in this section the thermal voltage V_T is defined as $V_T = kT/q$ where k is the Boltzmann constant, q is the fundamental electric charge, and T is the temperature. When T = 25 °C, V_T = 26 mV. All the simulated devices will be assumed to have a photoactive area A = 1 cm^2. Therefore, $R_SA = R_S$ and $R_PA = R_P$.

Shockley [81] and Prince [80] models have been used in the past to model organic solar cells [79] and organic photodiodes [5]. Although explorations (partial or total) of the impact of the electrical parameters on the performance of organic solar cell has been reported in the past at experimental and simulation levels [118], similar parametric explorations have not been found for OPDs.

During the experimental optimization of OPDs' performance two or more electrical parameters can be changed at the same time. Then, it is important to understand the impact of each parameter independently in the noise and the photogenerated current to strategize the optimization path. Both parameters (noise and the photogenerated current) will influence the overall performance of OPDs, and ultimately their specific detectivity D^*. In this section, this parametric exploration will be done by varying independently the values of the electrical parameters (J_{ph}, J_0, n, R_S, and R_P), considering values reported experimentally. Some of the selected values, which might not necessarily be attainable in practice, are also evaluated to test special conditions, e.g., the validity of the simplification of the Prince model [80] into a simpler model, i.e., Shockley model [81]. The values of the electrical parameters that will be explored are summarized in **Table 6**.

Table 6. Electrical parameters selected for the simulation. Photoactive area A = 1 cm^2. Types of devices includes organic photodiodes (OPDs) and organic solar cells (OSCs)

Electrical Parameter	Unit	Selected Range or Values for Simulation	Relevant References and/or Justification for the Selection of Values	Type of Device
J_{ph}	A/cm^2	0 - 1 x 10^{-1}	• Under dark condition: ○ J_{ph} = 0 • Under illumination condition: ○ J_{ph} = 67 mA/cm^2 (due to perfect solar photogeneration conditions up to λ = 4 μm)	Photodetectors and/or solar cells
J_0	A/cm^2	< 1 x 10^{-12}	• Not necessarily realizable in practice for OPDs. These values are used to validate whether large R_P (in the order of TΩ) emulates $R_P \rightarrow \infty$	N. A.
		1 x 10^{-12}	• PAL: P3HT:ICBA • Relevant references: [5]	Si PDs and OPDs
		10 x 10^{-12}	• PAL: P3HT:OPDs • Relevant references: [5]	OPDs
		100 x 10^{-12}	• This work (see **Section 4.2** and **Section 4.3**)	OPDs
		1 x 10^{-9}	• PAL: CuPc/PV • Relevant references: [119]	OSCs
n		1	• Band-to-band recombination • Relevant references: [5]	Si PDs
		1.5	• PAL: P3HT:ICBA • Relevant references: [5]	OPDs
		2	• Shockley-Read-Hall recombination	-
R_S	Ω	1	• Typical values in OSCs	OSCs
		1 x 10^3	• This work (see **Section 4.2** and **Section 4.3**)	OPDs
		1 x 10^6	• Not necessarily realizable in practice for OPDs. These values are used to evaluate conditions in which J_{ph} can be extracted in the form of J_{SC}	N. A.
R_P	Ω	1 x 10^3	• Typical values in OSCs	OSCs
		1 x 10^6	• Typical values in OSCs	OSCs
		1 x 10^9	• PAL: P3HT:ICBA and P3HT:PCBM • Relevant references [5]	OPDs
		10 x 10^9	• Relevant references [5]	Si PDs
		≥ 100 x 10^9	• Not necessarily realizable in practice for OPDs. These values are used to emulate conditions in which $R_P \rightarrow \infty$ • Relevant references: [5]	N. A.

4.1.1 J-V Curves under Dark Condition and V_{OC}-J_{SC} Curves obtained from the Shockley Model

The impact of the variation of the reverse saturation current J_0 and the ideality factor n on the electrical (photo)response of OPDs that follow the Shockley model (SM) is explored in this sub-section. **Figure 23**, **Figure 24**, and **Figure 25** show the *J*-*V* curves (**top**) under dark condition and the V_{OC}-J_{SC} curves (bottom) when the ideality factor is n = 1.0, n = 1.5, and n = 2.0, respectively. For each ideality factor condition, the reverse saturation current density J_0 is varied by one order of magnitude between 1 fA/cm^2 and 1 nA/cm^2. In the simulations, the photoactive area A = 1 cm^2 and the room temperature T = 25 °C.

The impact of the ideality factor n is mainly observed in the slope of *J*-*V* curves (under dark condition) in forward bias (**Figure 23**-**Figure 25 – top**). For a fixed value of J_0, the higher the n the lower the slope of the *J*-*V* curves. Indeed, it can be shown that for $V >> nV_T$ (around 52 mV when n = 2),

$$\ln\left(J_{DARK\_SM}\right) = \frac{V}{nV_T} + \ln(J_0) \tag{47}$$

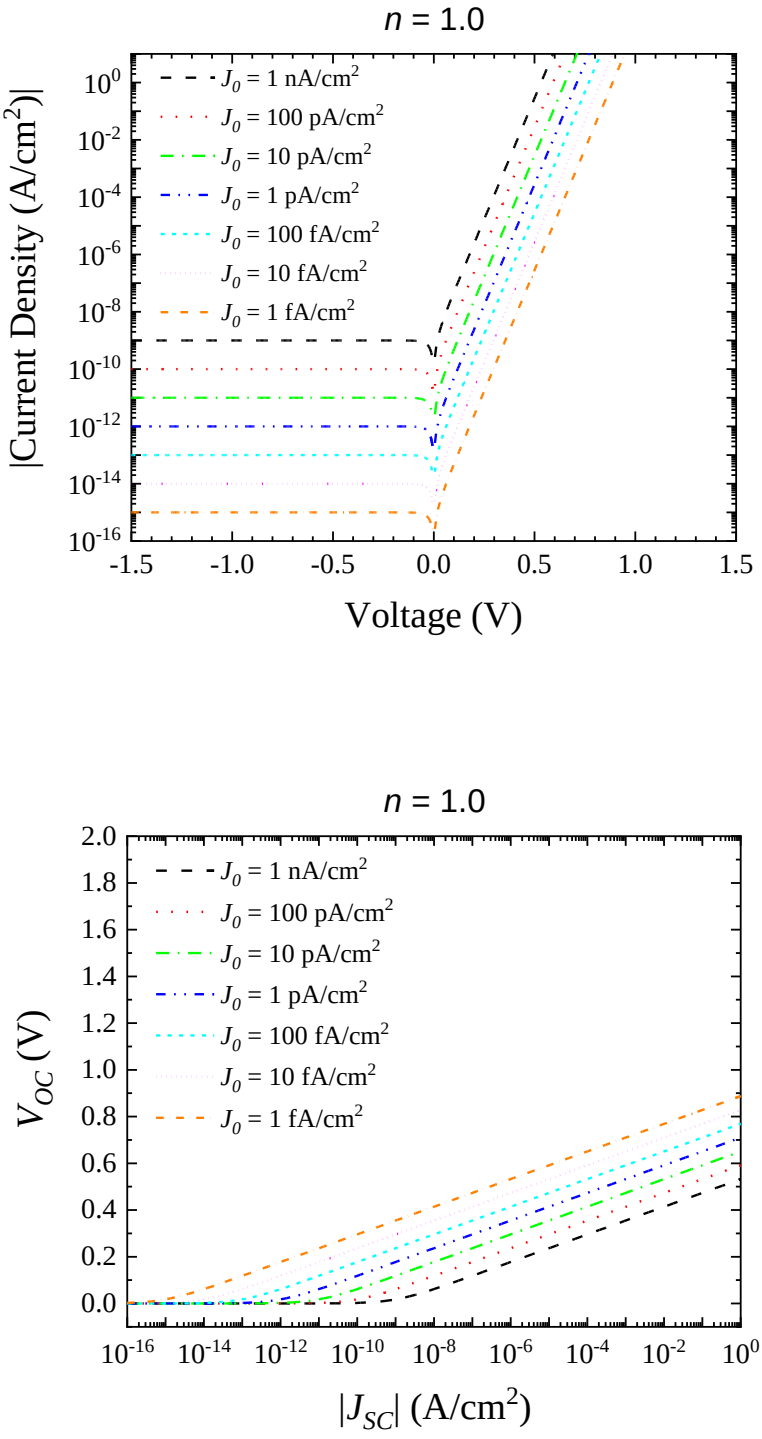

Figure 23. Simulated curves based on the Shockley model [81] – Variation of J_0 with n = 1. (Top) J-V curves in semi-log scale. (Bottom) V_{OC}-J_{SC} curve in semi-log scale.

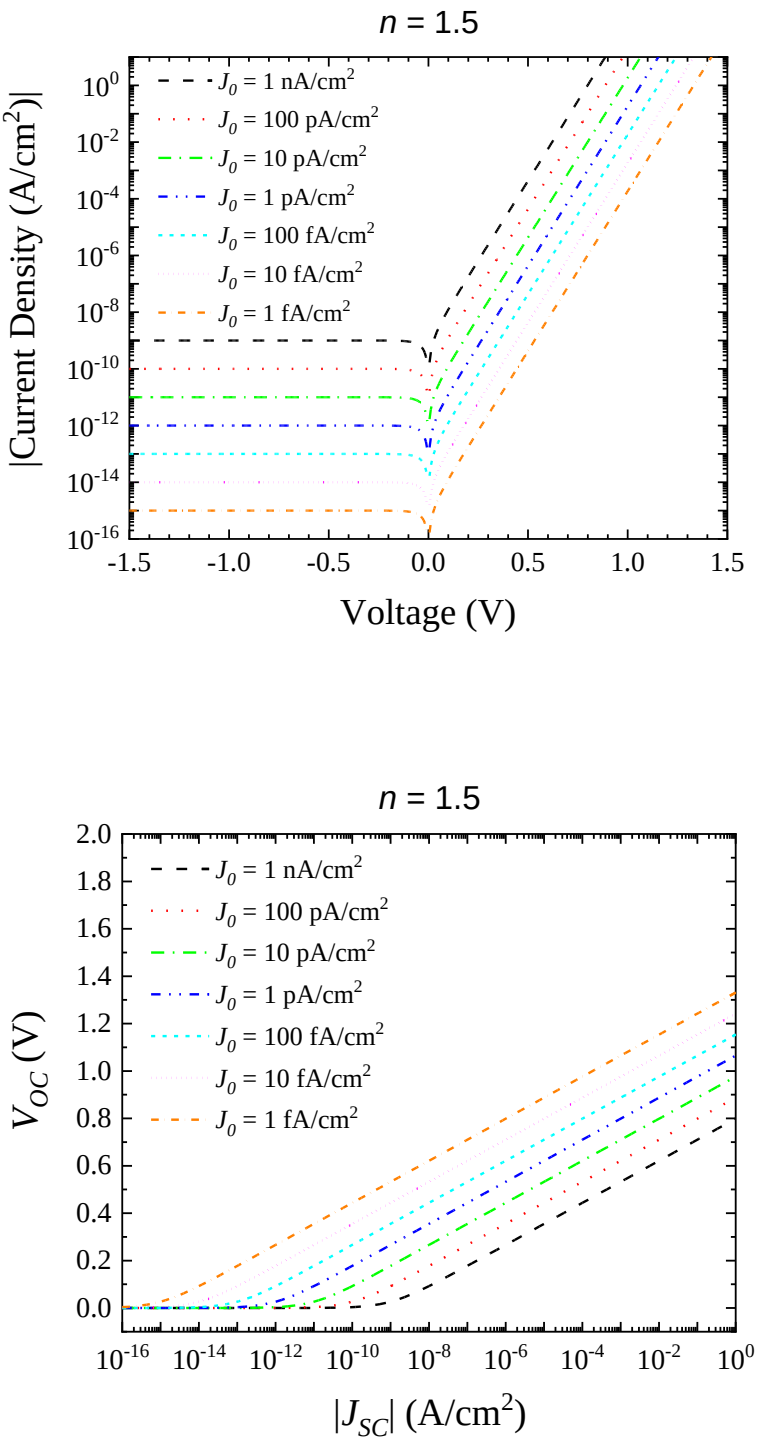

Figure 24. Simulated curves based on the Shockley model [81] – Variation of J_0 with n = 1.5. (Top) J-V curves in semi-log scale. (Bottom) V_{OC}-J_{SC} curve in semi-log scale.

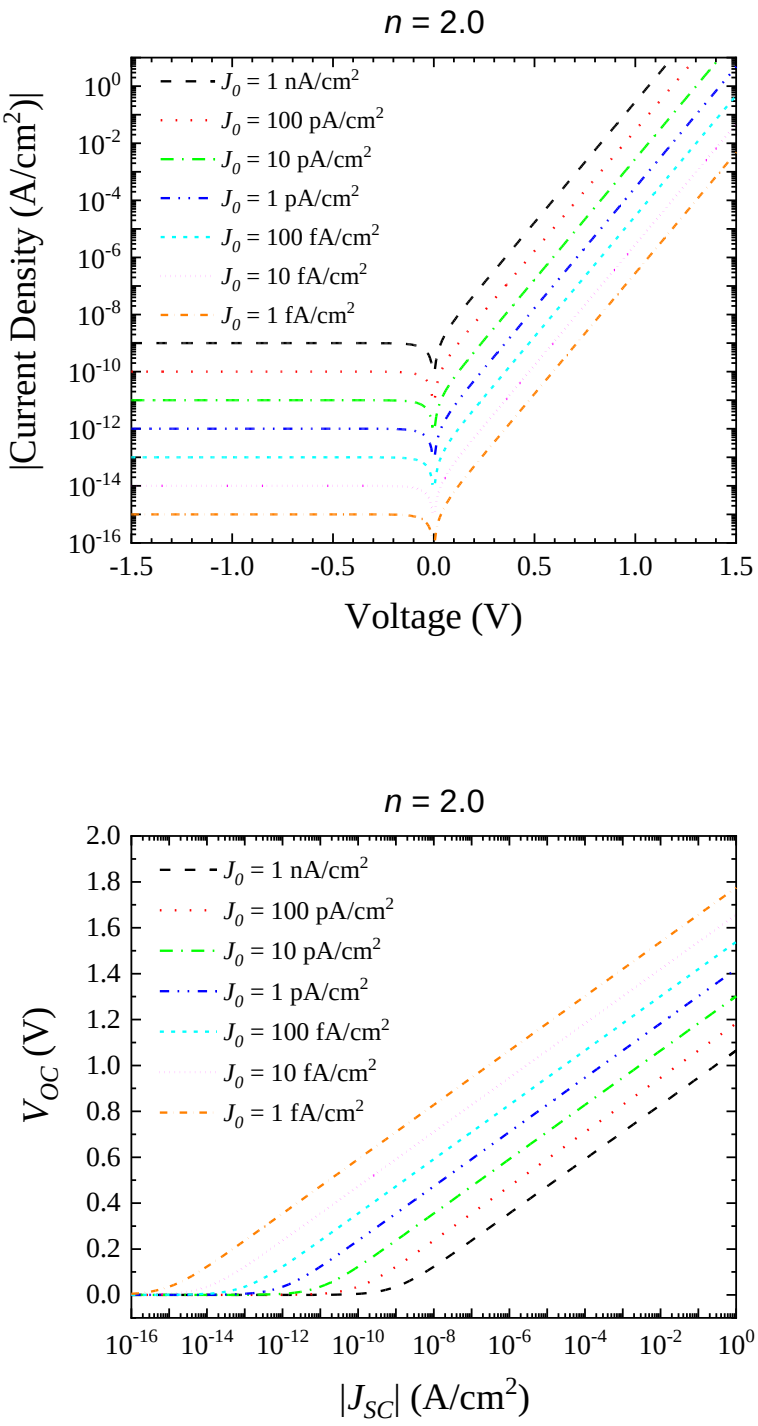

Figure 25. Simulated curves based on the Shockley model [81] – Variation of J_0 with n = 2. (Top) J-V curves in semi-log scale. (Bottom) V_{OC}-J_{SC} curve in semi-log scale.

Equation (47) is only valid for forward bias ($V >> V_T$). Similarly, the impact of n on the V_{OC}-J_{SC} curves is also observed in the slope of the curves (**Figure 23-Figure 25 – bottom**). However, in contrast to J-V curves, high n values increase the slope of the V_{OC}-J_{SC} curves for a fixed value of J_0. Indeed, it can be shown that for $V_{OC} >> nV_T$,

$$V_{OC} = nV_T \ln(J_{sc}/J_0) \tag{48}$$

The impact of the reverse saturation current J_0 is mainly observed in the constant value of J-V curves (under dark condition) in reverse bias (**Figure 23-Figure 25 –** top). The higher the value of J_0 the higher the values of J_{DARK_SM} attained in reverse bias. From the Shockley diode equation, it can be shown that $J_{DARK\_SM} = -J_0$ when $V << 0$. In forward bias, the J-V curves (under dark condition) are shifted up as per equation (47). On the other hand, the impact of J_0 on the V_{OC}-J_{SC} curves (**Figure 23-Figure 25 –** bottom), is observed in the cut-off value of the curves with respect to the J_{SC} axis (x axis). While this value has some influence of the ideality factor n, according to equation (48), it is dominated mainly by J_0 as $1.0 \leq n \leq 2.0$.

4.1.2 Simulated Spectral Power Density obtained from the Shockley Model (Dark Component)

The noise spectral power density for the Shockley model under dark condition $S_{i,shot,SM\_dark}$ is presented for three values of n (n = 1.0 in **Figure 26**, n = 1.5 in **Figure 27**, and n = 2.0 in **Figure 28**). For each n value, $S_{i,shot,SM\_dark}$ is calculated as a function of the external voltage V for different conditions of J_0. It is important to note that $S_{i,shot,SM\_dark}$ is constant in the frequency domain for a fixed V, n, and J_0 as the proposed circuit model only captures the shot noise.

The impact of the ideality factor n is observed in forward bias mainly (**Figure 26** - **Figure 28**): Lower values of $S_{i,shot,SM\_dark}$ are observed for higher values of n. However, no major impact of n on $S_{i,shot,SM\_dark}$ is observed at reverse bias conditions and at unbiased conditions. These are the conditions in which OPDs typically operate. Therefore, for the remaining simulation analysis, n will be assumed to be 1.0.

The **Figure 29** presents the root-mean square (RMS) noise current $I_{rms,shot,SM\_dark}$ calculated from the spectral noise power density $S_{i,shot,SM\_dark}$ as a function of the bandwidth B through

$$I_{rms,shot,SM\_dark} = \sqrt{S_{i,shot,SM\_dark}(V = 0)B} \tag{49}$$

for an unbiased condition ($V = 0$).

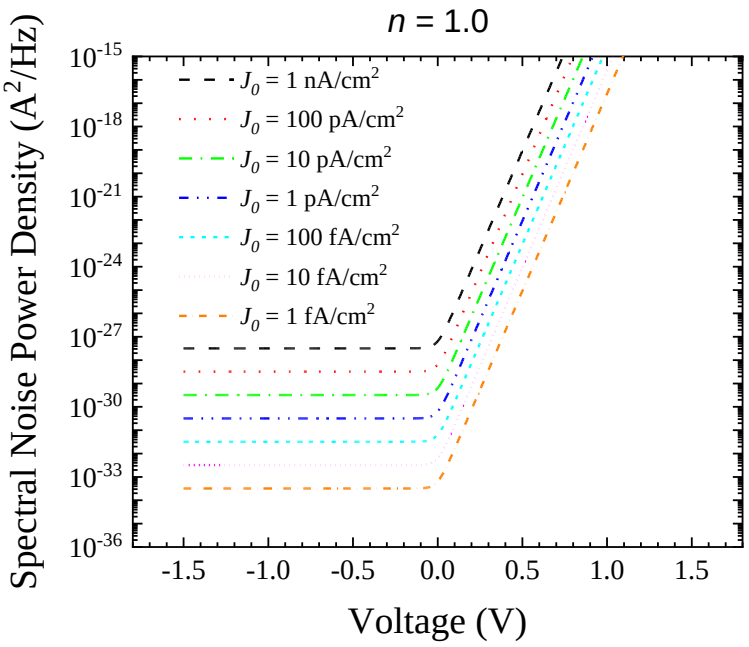

Figure 26. Simulated curves based on the Shockley model [81] – Spectral noise power density $S_{i,shot,dark}$ as a function of external voltage V for different levels of reverse saturation current density J_0. Ideality factor n = 1.0.

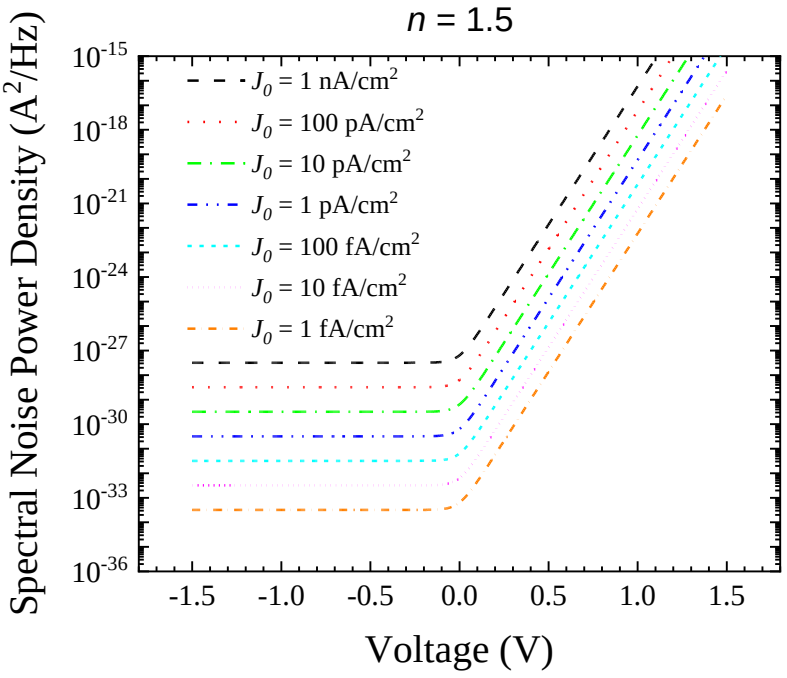

Figure 27. Simulated curves based on the Shockley model [81] – Spectral noise power density $S_{i,shot,dark}$ as a function of external voltage V for different levels of reverse saturation current density J_0. Ideality factor n = 1.5.

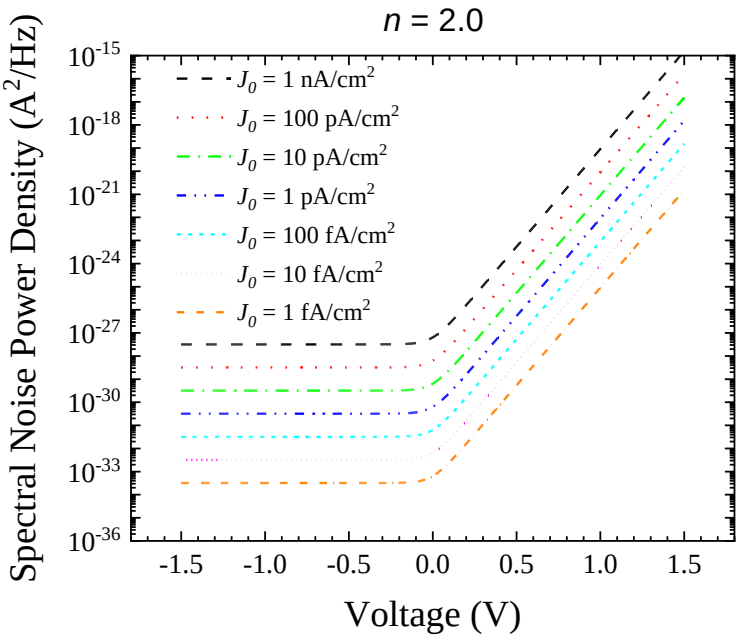

Figure 28. Simulated curves based on the Shockley model [81] – Spectral noise power density $S_{i,shot,SM\_dark}$ as a function of external voltage V for different levels of reverse saturation current density J_0. Ideality factor n = 2.0.

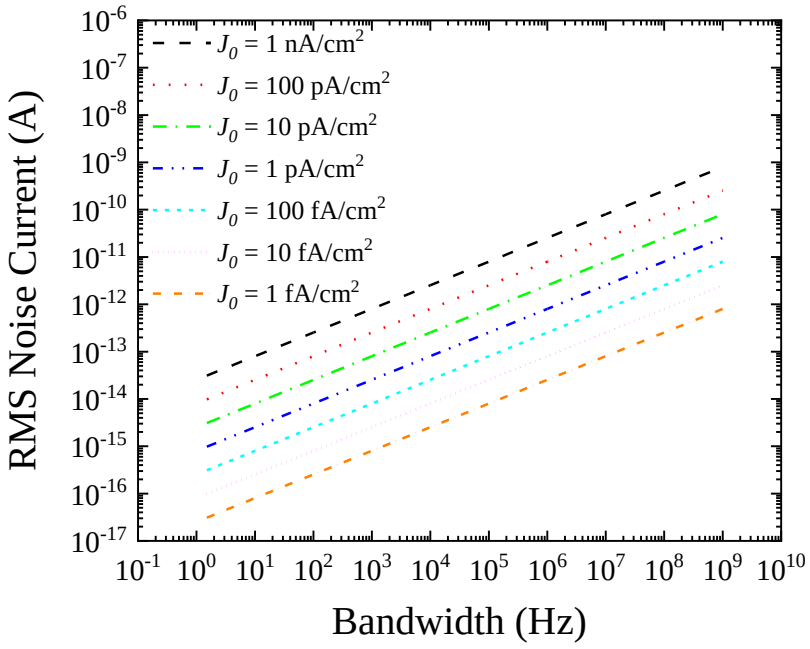

Figure 29. Simulated curves based on the Shockley model [81] – Variation of $S_{i,shot,SM\_dark}$ as a function of the bandwidth B and for different levels of reverse saturation current density J_0. Ideality factor n = 1.0.

As expected, the higher the value of J_0, the higher the value of $I_{rms,shot,SM\_dark}$ because at unbiased condition ($V = 0$)

$$S_{i,shot,SM\_dark}(V = 0) = 4qAJ_0 \tag{50}$$

where q is the fundamental electric charge, J_0 is the reverse saturation current density, and A is the photoactive area. For these simulations, $A = 1$ cm^2 and then the reverse saturation current I_0 is $I_0 = J_0A$. Combining equations (49) and (50), $I_{rms,shot,SM\_dark}$ can be written explicitly as

$$I_{rms,shot,SM\_dark} = \sqrt{4qI_oB} \tag{51}$$

4.1.3 Simulated Spectral Power Density obtained from the Shockley Model (Illumination Component)

In general, the noise spectral power density under light condition $S_{i,shot,light}$ can be written in general as

$$S_{i,shot,light} = 2qAJ_{LIGHT} \tag{52}$$

where q is the fundamental electric charge, A is the photoactive area, and J_{LIGHT} is the current at the output of the device. At $V = 0$, $J_{LIGHT} = J_{SC}$. For the Shockley model (SM),

the photocurrent can be expressed as $J_{LIGHT} = J_{SC} = J_{ph}$. Then, $S_{i,shot,SM\_light}(V = 0)$ can be expressed as

$$S_{i,shot,SM\_light}(V = 0) = 2qAJ_{ph} \tag{53}$$

Figure 30 shows the noise spectral power density under light condition and unbiased condition $S_{i,shot,light\_SM}(V = 0)$ as a function J_{ph}.

On the other hand, **Figure 31** presents the root-mean square (RMS) noise current $I_{rms,shot,SM\_light}$ for different values of J_{ph} calculated from $S_{i,shot,light\_SM}(V = 0)$

$$I_{rms,shot,SM\_light} = \sqrt{S_{i,shot,SM\_light}(V = 0)B} \tag{54}$$

Combining equations (53) and (54), $I_{rms,shot,SM\_dark}$ can be written explicitly as

$$I_{rms,shot,SM\_light} = \sqrt{2qI_{ph}B} \tag{55}$$

As expected, the higher the value of $I_{ph} = AJ_{ph}$, the higher the value of $I_{rms,shot,SM\_light}$.

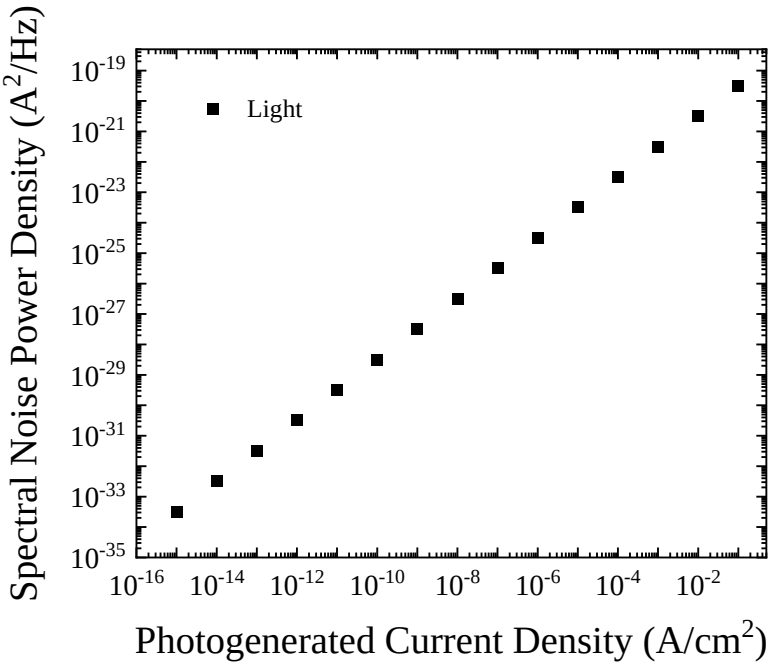

Figure 30. Simulated curve for the spectral noise power density $S_{i,shot,light}$ of the photogenerated current density (J_{ph}) before parasitic effects.

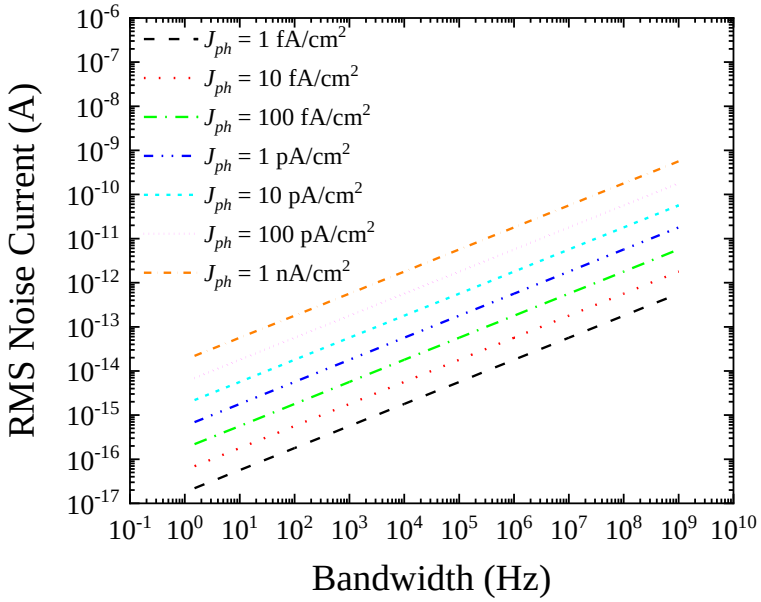

Figure 31. Simulated curves based on the Shockley model [81]. RMS shot noise current ($I_{rms,shot}$) due to illumination as a function of the bandwidth B.

4.1.4 J-V Curves under Dark Condition and V_{OC}-J_{SC} Curves obtained from the Prince Model

4.1.4.1 Impact of the Series Resistance R_S on the *J-V* Curves under Dark Condition and V_{OC}-J_{SC} Curves when the Shunt Resistance R_P is High (100 TΩ)

The impact of the variation of the reverse saturation current J_0 and the series resistance for an ideality factor n = 1.0 and a shunt resistance R_P = 100 TΩ on the electrical (photo)response of OPDs that follow the Prince model is explored in this sub-section.

Figure 32, **Figure 33**, and **Figure 34** show the *J-V* curves (top) under dark condition and the V_{OC}-J_{SC} curves (bottom) when the reverse saturation current density is J_o = 1 nA/cm^2, J_0 = 1 pA/cm^2, and J_0 = 1 fA/cm^2, respectively. For each reverse saturation current density condition, the series resistance R_S is varied by one order of magnitude between 1 Ω and 100 kΩ. In the simulations, the photoactive area A = 1 cm^2 and the temperature T = 25 °C. The continuous line in each figure (**Figure 32**-**Figure 34**) represents the Shockley model for reference.

The impact of the reverse saturation current density J_0 is firstly observed in reverse bias (**Figure 32**-**Figure 34** – top). For a fixed value of R_S, the higher the reverse saturation current density J_0 the higher the value of the current density in reverse bias J_{DARK}($V << 0$). It is noted that even with a very high shunt resistance (i.e., R_S = 100 TΩ), a low saturation current density (i.e., J_0 = 1 fA/cm^2) can make that the *J-V* curves does not follow the Shockley model (continuous line) in reverse bias (**Figure 34** – top). In forward bias, the impact of J_0 on the *J-V* curves resembles the shift of the curves in the Shockley model.

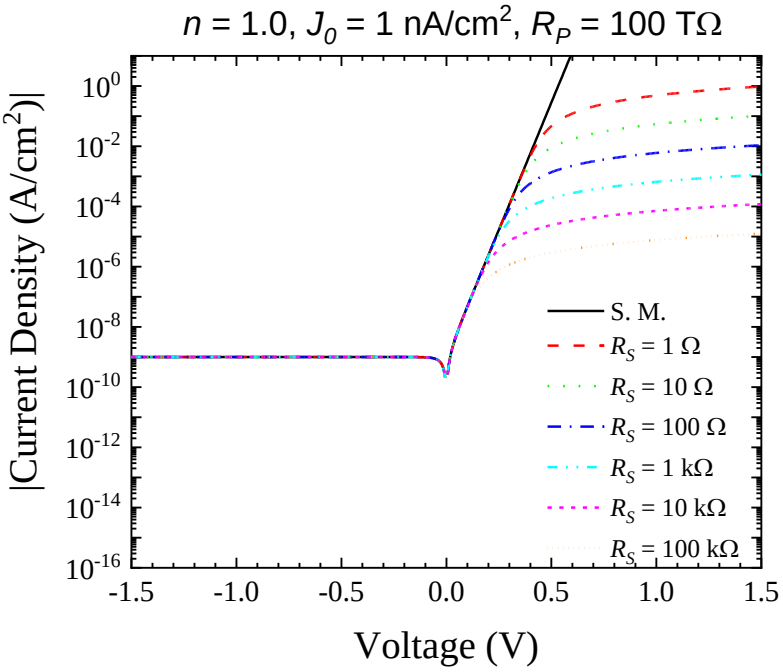

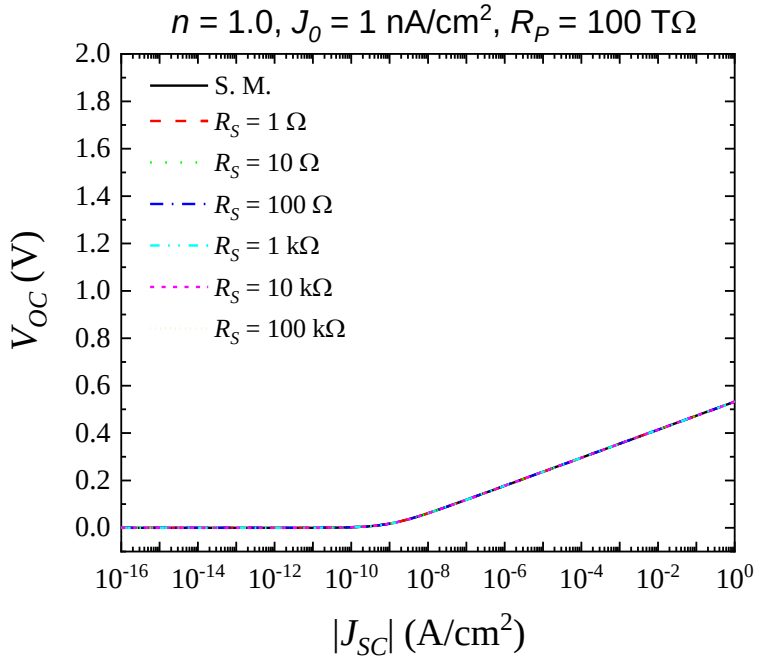

Figure 32. Simulated curves based on the Prince model [80] – Variation of R_S with n = 1, Jo = 1 nA/cm^2, and R_P = 100 TΩ. (Top) J-V curves in semi-log scale. (Bottom) V_{OC}-J_{SC} curve in semi-log scale.

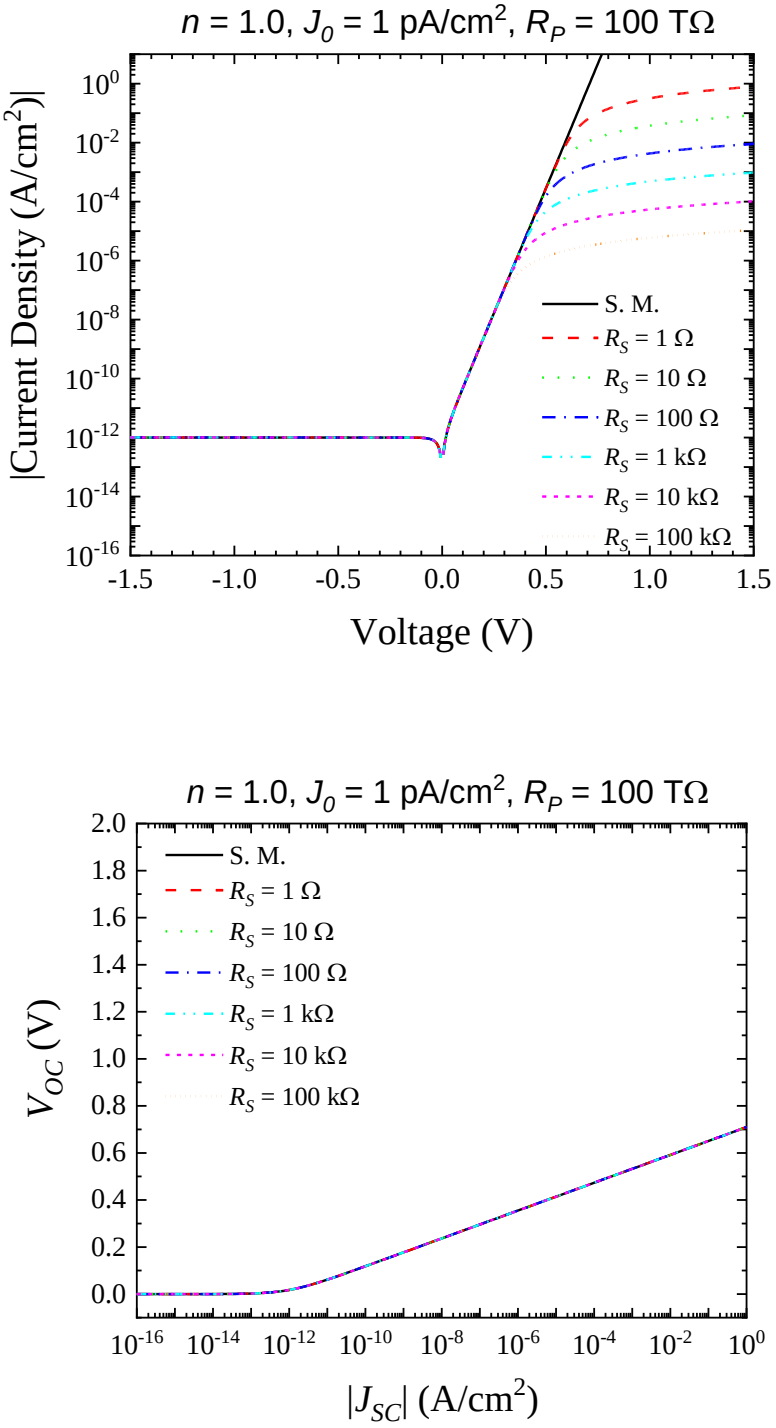

Figure 33. Simulated curves based on the Prince model [80] – Variation of R_S with n = 1, Jo = 1 pA/cm^2, and R_P = 100 TΩ. (Top) J-V curves in semi-log scale. (Bottom) V_{OC}-J_{SC} curve in semi-log scale.

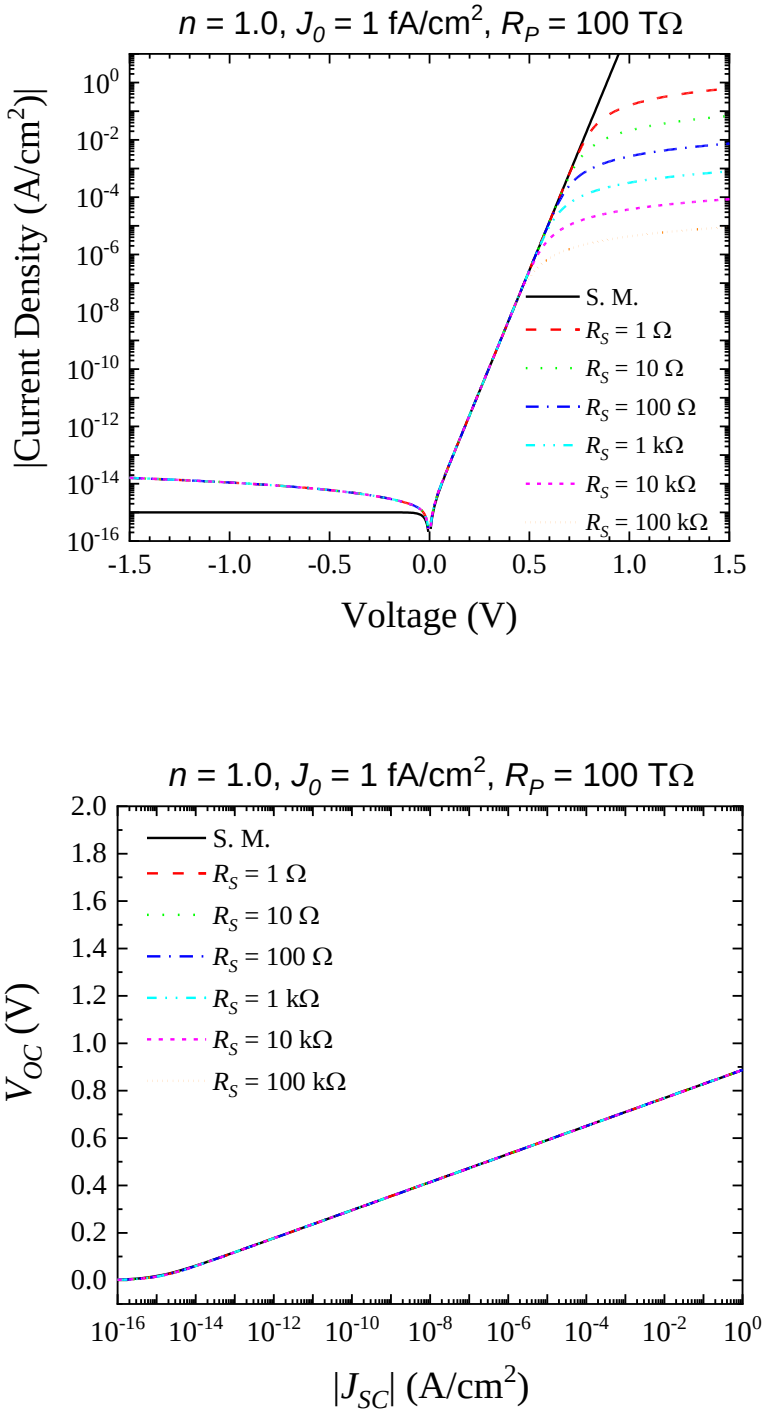

Figure 34. Simulated curves based on the Prince model [80] – Variation of R_S with n = 1, Jo = 1 fA/cm^2, and R_P = 100 TΩ. (Top) J-V curves in semi-log scale. (Bottom) V_{OC}-J_{SC} curve in semi-log scale.

The impact of the series resistance R_S is negligible in reverse bias and it is mainly observed in forward bias (**Figure 32**-**Figure 34** – top). In forward bias, R_S is the responsible for deviation of the *J*-*V* curves from the Shockley model, suggesting a saturation of the current in forward bias. This behavior is observed independently of the levels of reverse saturation current J_0 simulated (J_0 = 1 nA/cm^2 in **Figure 32**, J_0 = 1 pA/cm^2 in **Figure 33**, and J_0 = 1 fA/cm^2 in **Figure 34**). On the other hand, V_{OC}-J_{SC} curves (**Figure 32**-**Figure 34** – bottom) are not impacted by the chosen values of J_0, R_S and R_P following the Shockley model (continuous line).

4.1.4.2 Impact of the Shunt Resistance R_P on the *J*-*V* Curves under Dark Condition and V_{OC}-J_{SC} Curves when the Series Resistance R_S is Low (1 Ω)

The impact of the variation of the reverse saturation current J_0 and the shunt resistance R_P on the electrical (photo)response of OPDs that follow the Prince model is explored in this sub-section. **Figure 35**, **Figure 36**, and **Figure 37** show the *J*-*V* curves (top) under dark condition and the V_{OC}-J_{SC} curves (bottom) when the reverse saturation current density is J_0 = 1 nA/cm^2, J_0 = 1 pA/cm^2, and J_0 = 1 fA/cm^2, respectively. For each reverse saturation current density condition, the shunt resistance R_P is varied by one order of magnitude between 1 GΩ and 100 TΩ. In the simulations, the series resistance R_S = 1 Ω the photoactive area A = 1 cm^2 and the temperature T = 25 °C. The continuous line in each figure (**Figure 35**-**Figure 37**) represents the Shockley model for reference.

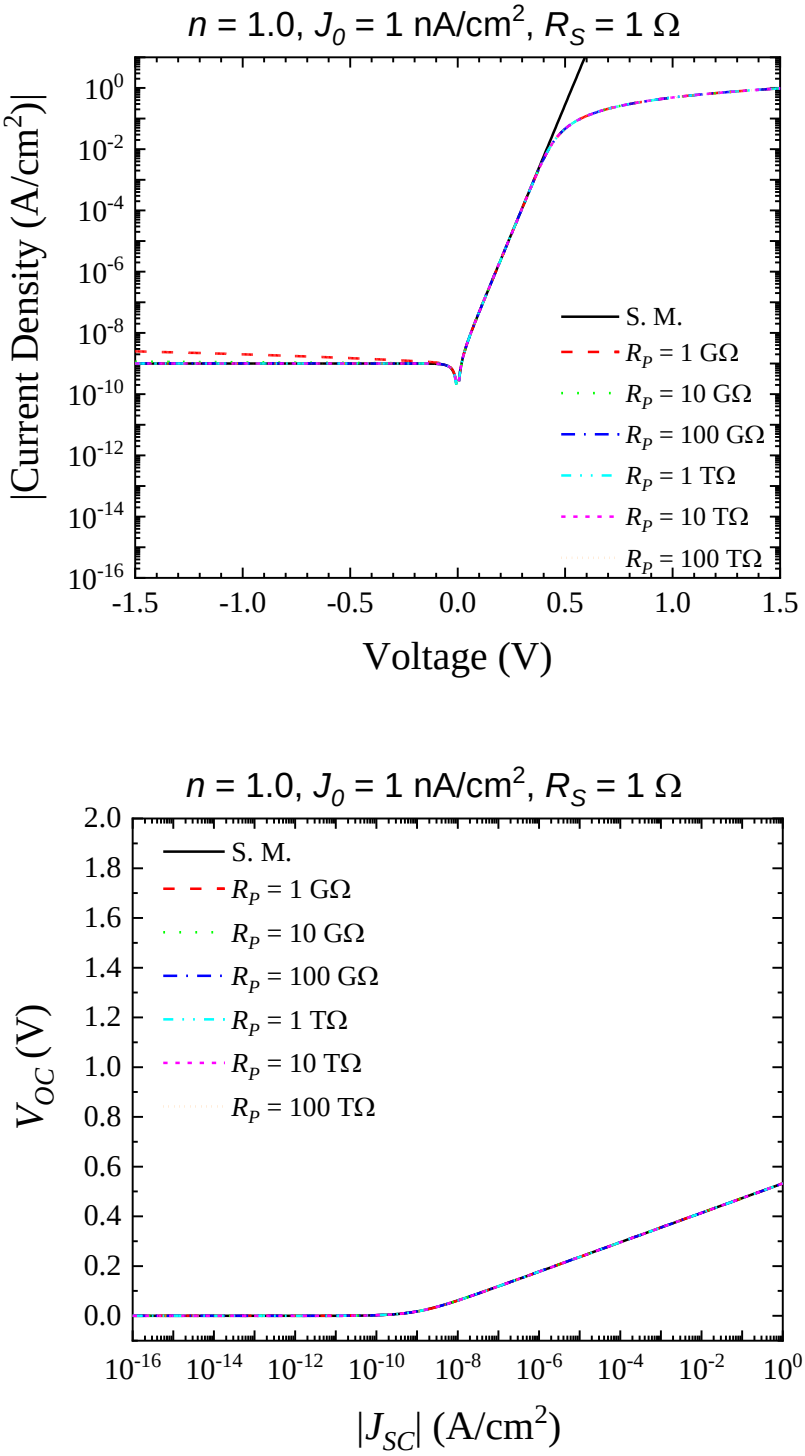

Figure 35. Simulated curves based on the Prince model [80] – Variation of R_P with n = 1.0, Jo = 1 nA/cm^2, and R_S = 1 Ω. (Top) J-V curves in semi-log scale. (Bottom) V_{OC}-J_{SC} curve in semi-log scale.

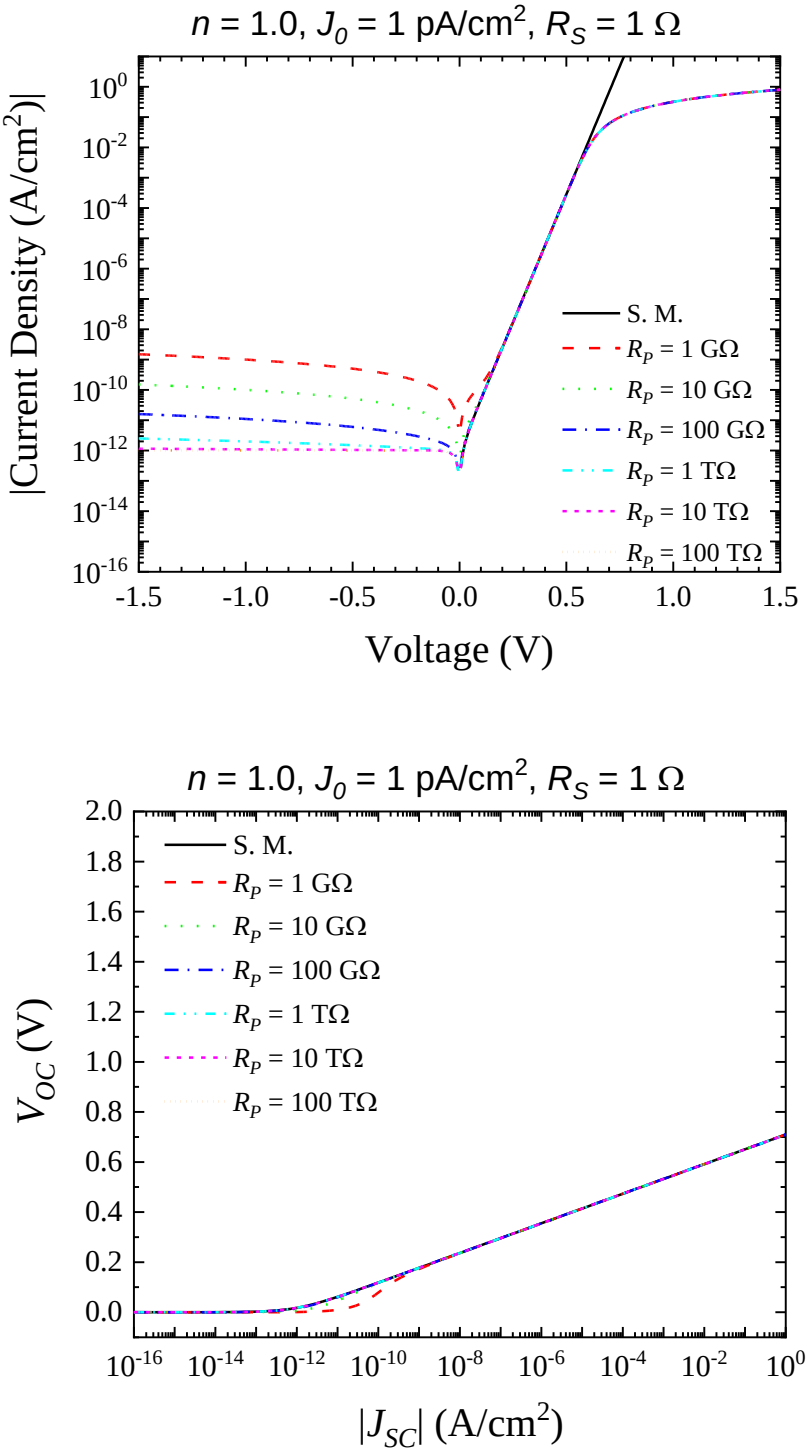

Figure 36. Simulated curves based on the Prince model [80] – Variation of R_P with n = 1.0, Jo = 1 pA/cm^2, and Rs = 1 Ω. (Top) J-V curves in semi-log scale. (Bottom) V_{OC}-J_{SC} curve in semi-log scale.

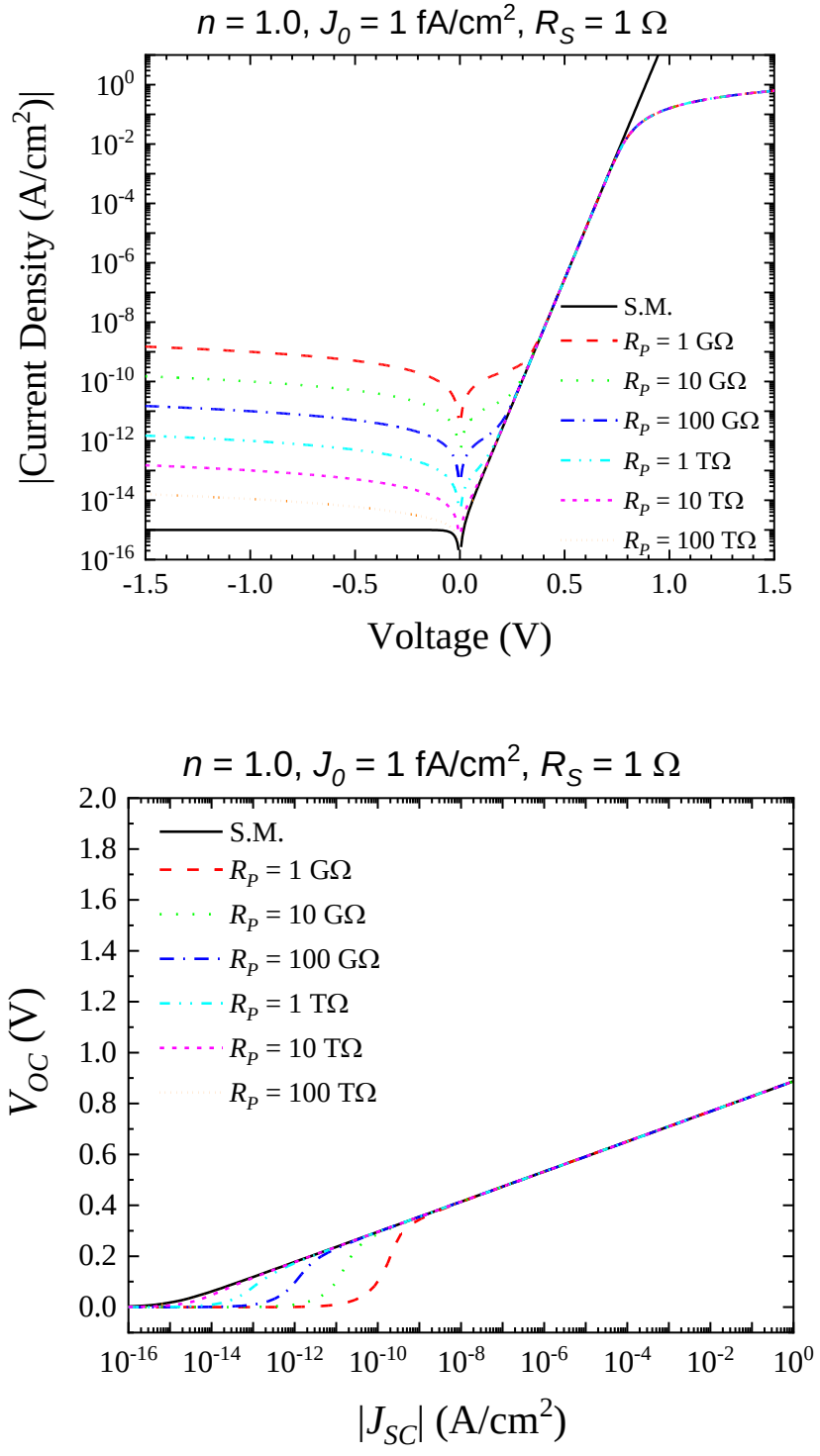

Figure 37. Simulated curves based on the Prince model [80] – Variation of R_P with n = 1, Jo = 1 fA/cm^2, and R_S = 1 Ω. (Top) J-V curves in semi-log scale. (Bottom) V_{OC}-J_{SC} curve in semi-log scale.

The impact of the shunt resistance R_P is negligible in forward bias, where the series resistance R_S is the responsible for the saturation of the current density value in forward bias (**Figure 35-Figure 37 - top**). In reverse bias, the departure of the *J-V* curves (as a function of the shunt resistance values R_P) from the Shockley model depends on the value of the reverse saturation current J_0. For example, when J_0 = 1 nA/cm^2 (**Figure 35 -** top), the deviation from the Shockley model happens at R_P = 1 GΩ. When J_0 = 1 pA/cm^2 (**Figure 36 -** top), the deviation is observed with R_P < 10 TΩ. When J_0 = 1 fA/cm^2 (**Figure 37 -** top), show the departure of the *J-V* curves for all the simulated shunt resistance values R_P.

On the other hand, V_{OC}-J_{SC} curves (**Figure 35 - bottom**) are impacted by the R_P values depending on the values of the reverse saturation current density J_0. For the R_P values simulated, no impact was observed when J_0 = 1 nA/cm^2 (**Figure 35**). When J_0 = 1 pA/cm^2 (**Figure 36**), the V_{OC}-J_{SC} curves show deviations from the Shockley model for R_P = 1 GΩ and slightly for R_P = 10 GΩ. When J_0 = 1 fA/cm^2 (**Figure 37**), for practically all the values of R_P, the V_{OC}-J_{SC} curves deviate from the Shockley model at low values of J_{SC}.

Note that the higher the reverse saturation current density J_0, the higher the tolerance to low shunt resistance values R_P. The deviation from the Shockley model is more visible in the *J-V* curves than in the V_{OC}-J_{SC} ones.

4.1.4.3 Impact of the Shunt R_P and the Series Resistance R_S on the Thermal Noise

The impact of the series resistance R_S and the shunt resistance R_P on the thermal noise is evaluated next. The spectral noise power density $S_{i,thermal}$ due to thermal noise can be expressed as

$$S_{i,thermal} = \frac{4kT}{R_S + R_P} \tag{56}$$

where k is the Boltzmann constant and T is the temperature. The values for thermal RMS noise current $I_{rms,thermal}$ can be found through $S_{i,thermal}$ as

$$I_{rms,thermal} = \sqrt{S_{i,thermal} B} \tag{57}$$

Combining equations (56) and (57), $I_{rms,thermal}$ as a function of B for a given T can be written as

$$I_{rms,thermal} = \sqrt{\frac{4kTB}{R_S + R_P}} \tag{58}$$

Figure 38 shows that $S_{i,thermal}$ is dominated by the highest value of resistance which is typically R_P. Among the simulated conditions for R_S, the worst-case scenario (highest values of $S_{i,thermal}$) is observed for the lowest value of R_S (1 Ω) and the lowest value of R_P (100 kΩ). When $R_P >> R_S$, R_S does not have an appreciable impact on the $S_{i,thermal}$ giving some flexibility for having high values of R_S in the fabrication process. **Figure 39** shows the benefit of maximizing the value of R_P as the value of $I_{rms,thermal}$ decreases with high values of R_P. As expected, the$I_{rms,thermal}$ increases with the bandwidth *B*.

4.1.4.4 Impact of the Ratio between the Shunt R_P and the Series Resistance R_S on the Photocurrent J_{LIGHT}

For the Prince model in short-circuit condition, the impact of the variation of the ratio between the shunt resistance and the series resistance (R_P/R_S) on the photocurrent density after parasitic effects (then $J_{LIGHT} = J_{SC}$) is evaluated. The evaluation is done for three different series resistance values R_S = 1 Ω (**Figure 40**), R_S = 1 kΩ (**Figure 41**), and R_S = 1 MΩ (**Figure 42**) and for two different photogenerated (before parasitic effects) current density levels: J_{ph} = 100 pA/cm^2 (**Figure 40–Figure 42 - left**) and J_{ph} = 100 fA/cm^2 (**Figure 40–Figure 42 - right**). In each figure, different simulation results for three reverse saturation current densities (J_0 = 1 fA/cm^2, J_0 = 1 pA/cm^2, and J_0 = 1 nA/cm^2) are evaluated.

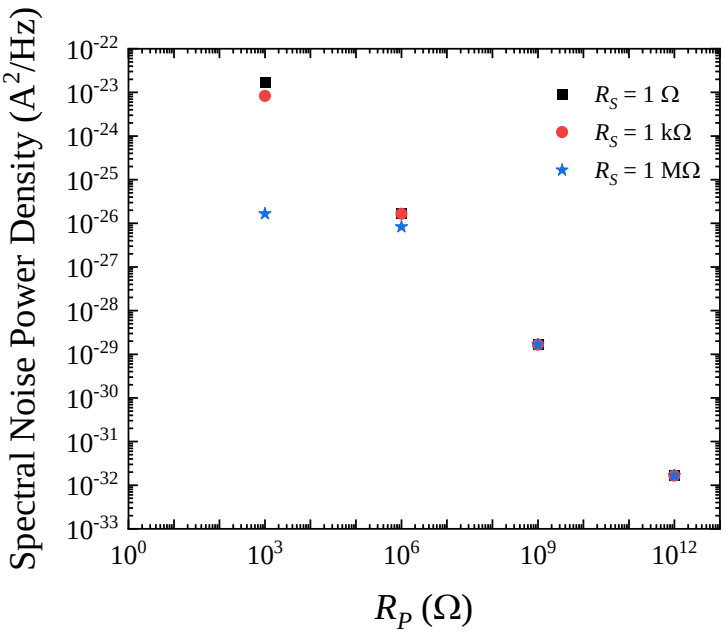

Figure 38. Simulated curves based on the Prince model [80] – Impact of the variation of R_P and R_S on the spectral noise power density due to thermal noise $S_{i,thermal}$.

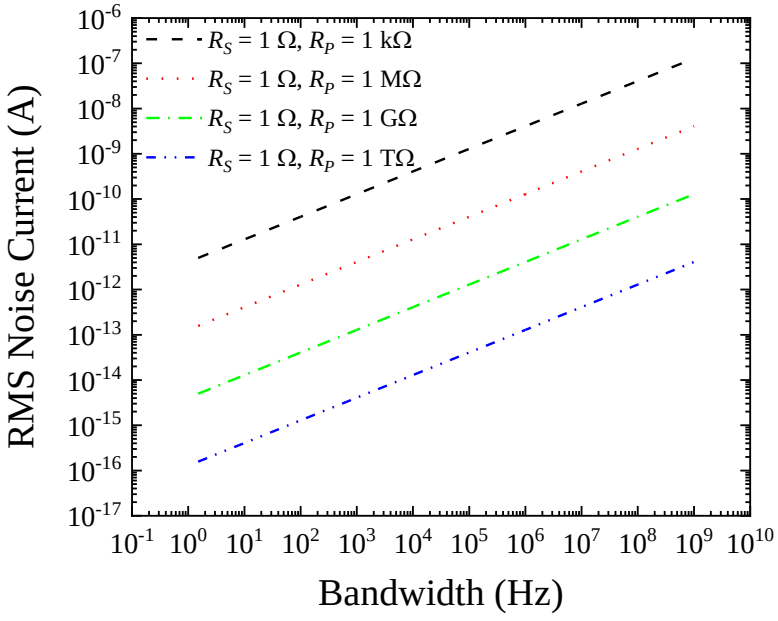

Figure 39. Simulated curves based on the Prince model [80] – RMS thermal noise current ($I_{rms,thermal}$) due to R_P as a function of the bandwidth B (with R_S = 1 Ω).

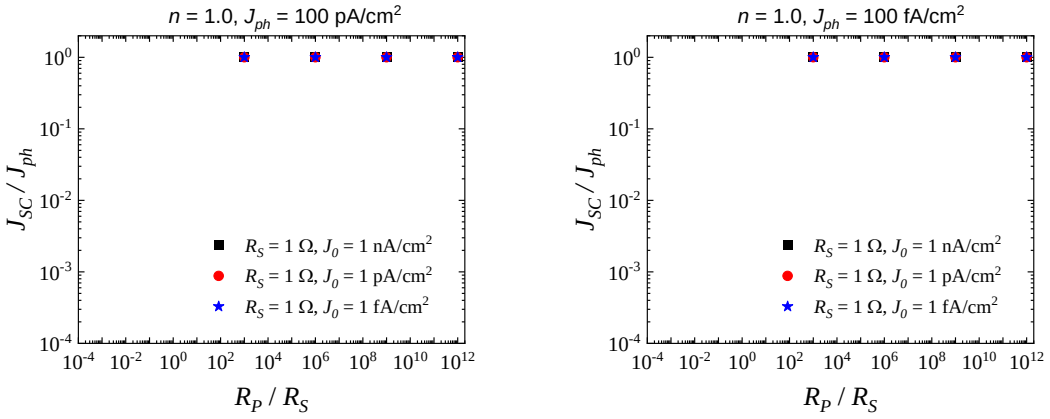

Figure 40. Simulated curves based on the Prince model [80] – Impact of the variation of R_P / R_S on J_{SC} (with R_S = 1 Ω). R_P: 1 kΩ, 1 MΩ, 1 GΩ, and 1 TΩ. (Left) J_{ph} = 100 pA/cm². (Right) J_{ph} = 100 fA/cm².

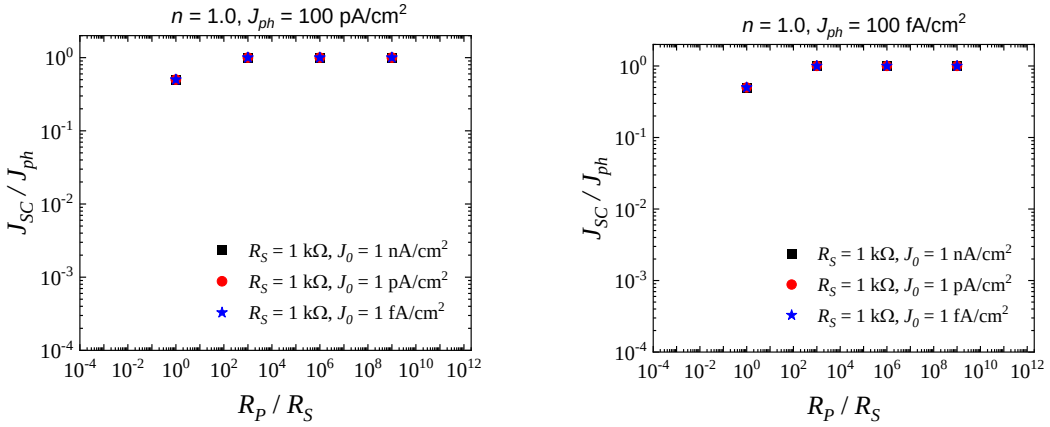

Figure 41. Simulated curves based on the Prince model [80] – Impact of the variation of R_P / R_S on J_{SC} (with R_S = 1 kΩ). R_P: 1 kΩ, 1 MΩ, 1 GΩ, and 1 TΩ. (Left) J_{ph} = 100 pA/cm². (Right) J_{ph} = 100 fA/cm².

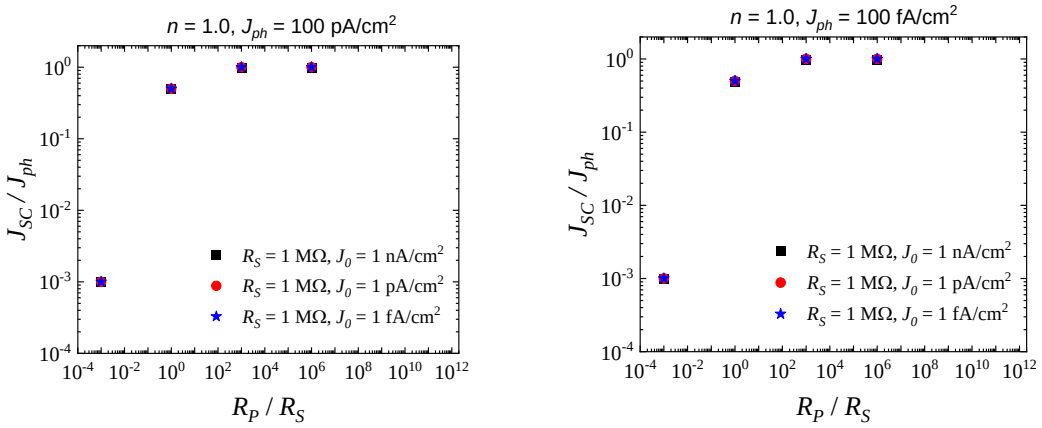

Figure 42. Simulated curves based on the Prince model [80] – Impact of the variation of R_P / R_S on J_{SC} (with R_S = 1 MΩ). R_P: 1 kΩ, 1 MΩ, 1 GΩ, and 1 TΩ. (Left) J_{ph} = 100 pA/cm^2. (Right) J_{ph} = 100 fA/cm^2.

From the simulation results, no appreciable differences are observed for the two different levels of illumination, namely, J_{ph} = 100 pA/cm^2 (**Figure 40–Figure 42 - left**) and J_{ph} = 100 fA/cm^2 (**Figure 40–Figure 42 - right**). For these simulated illumination conditions, J_0 does not have an impact and then all the points overlap.

No appreciable changes J_{SC}/J_{ph} (logarithmic scale) are observed at a low series resistance value, R_S = 1 Ω (**Figure 40**), for the chosen R_P/R_S values (R_P = 1 kΩ, 1 MΩ, 1 GΩ, and 1 TΩ). Then, the photogenerated current density is transferred to the output of the circuit (short-circuit condition) and $J_{SC} \approx J_{ph}$; for the next simulated value of series resistance R_S = 1 kΩ (**Figure 41**), a reduction of the current at the output in short-circuit condition (J_{SC}) is observed for R_P/R_S = 1 (R_P = 1 kΩ) making $J_{SC} \approx 0.4 J_{ph}$. Then a significant part of the photogenerated current density cannot be extracted at the output of the circuit; finally, for R_S = 1 MΩ (**Figure 42**), the current density at the output (J_{SC}) falls drastically

for $R_P/R_S = 10^{-3}$ (R_P = 1 kΩ) then $J_{SC} \approx 10^{-3}\ J_{ph}$. For $R_P/R_S = 1$ (R_P = 1 MΩ), a less drastic fall of the output current (J_{SC}) is observed ($J_{SC} \approx 0.4 J_{ph}$).

These results show that for low illumination conditions (e.g., J_{ph} = 100 pA/cm^2 or J_{ph} = 100 fA/cm^2) most of the photogenerated current density (J_{ph}) before parasitic effects can be extracted at the output in the form of short-circuit current density (J_{SC}), namely $J_{SC} \approx J_{ph}$. This is possible if $R_P >> R_S$ even at very high series resistance values (e.g., R_S = 1 kΩ or R_P = 1 MΩ) in contrast to high illumination values (e.g., J_{SC} >> 1 mA/cm^2) typical in standard testing conditions of solar cells with high power conversion efficiencies (PCE >> 1%).

4.1.5 Summary of Results for Simulations

Simulations have helped understand the impact of the equivalent circuit's parameters (individually) on the performance of photodiodes. Based on the presented simulations, the performance of OPDs can be improved (low thermal noise and high photocurrent) by maximizing R_P, R_P / R_S and R_S can have high values 1 MΩ (when R_P / $R_S \geq 10^3$). Additionally, the minimization of J_0, independently of the value of n (at unbiased conditions and reverse bias condition) will contribute to the reduction of white noise. These design guidelines will be used in the fabrication of OPDs expecting than more than one parameter changes during the optimization.

4.2 Approach 1: PCE10:$PC_{71}BM$-Based Organic Photodiodes (OPDs) with a Thick Photo-Active (PAL) Layer

OPDs with thick PAL (500 nm) based on the polymer electron-donor P3HT and the electron-acceptor fullerene ICBA have enabled OPDs with detectivity D* values comparable to Silicon [5]. Furthermore, this approach has been reported as the driving strategy for other high-performance broadband OPDs [120], suggesting this approach is extendable to other PAL materials. Guided by the simulation results obtained in Section **4.1**, the optimization of PCE10:$PC_{71}BM$ OPDs will be done through the variation of the PAL thickness to reduce the noise and maximize *D**. The thickness variation is done through the tuning of the chemical concentration of the solution prepared for deposition of the PAL through the spin-coating method. The device structure used in this aprpoach (approach 1) is shown in **Figure 43**.

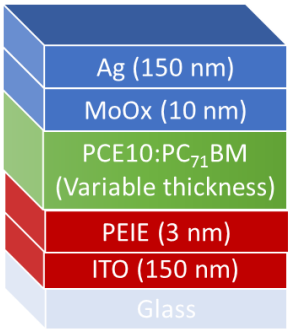

Figure 43. Device structure used in approach 1. The type of the PAL (PCE10:$PC_{71}BM$ with variable thickness) is a bulk heterojunction (BHJ). ECE: ITO (150 nm) / PEIE (3 nm). HCE: MoO_x(10 nm)/Ag (150 nm).

Various concentrations were tested (25 mg/mL, 35 mg/mL, 50 mg/mL, 70 mg/mL, and 100 mg/L) during the optimization process to obtain PCE10:$PC_{71}BM$-based OPDs with low noise. The correspondence of the some of the concentrations tested and the obtained thickness (measured through profilometry) is displayed in **Figure 44**. **Table 7** summarizes the relation between the concentration and the thickness of the PAL used in the fabrication of PCE10:$PC_{71}BM$ OPDs. The thickness values for concentrations of 35, 50, and 70 mg/mL were obtained from measurements. The thickness values for concentrations of 25 mg/mL and 100 mg/mL were obtained from extrapolation of the measured values. For some of obtained PCE10:$PC_{71}BM$ PAL, the absorption is indirectly quantified through 1 – transmission (T) with ellipsometry and it is shown in **Figure 45** confirming the sensitivity of PCE10:$PC_{71}BM$ PAL in the visible and NIR regions.

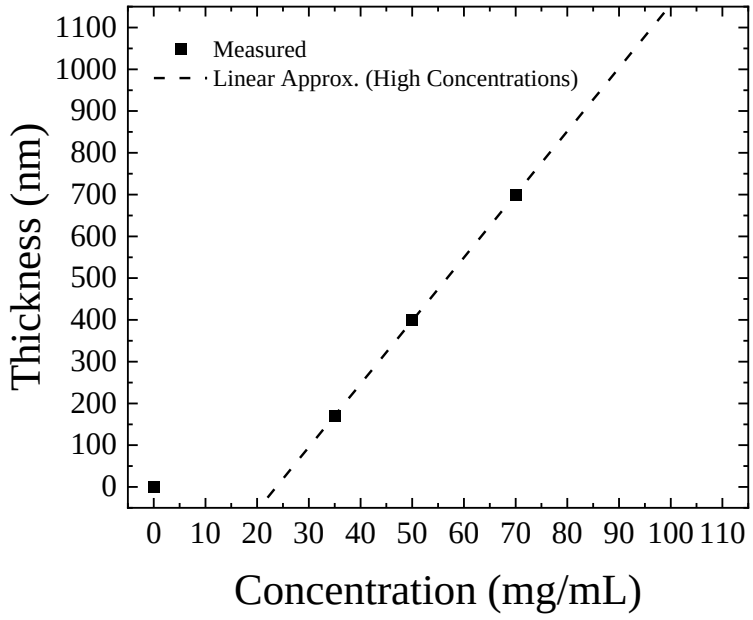

Figure 44. Relation between the concentration for the PCE10:$PC_{71}BM$ solution and the thickness of the PCE10:$PC_{71}BM$ PAL attained through spin coating of the solution on glass. Measured in air with profilometry.

Table 7. The relation between the concentration and the thickness of the PCE10:$PC_{71}BM$ PAL.

Concentration (mg/mL)	Thickness (nm)	Concentration (mg/mL)	Thickness (nm)
25	~50	70	700
35	170	100	1150
50	400		

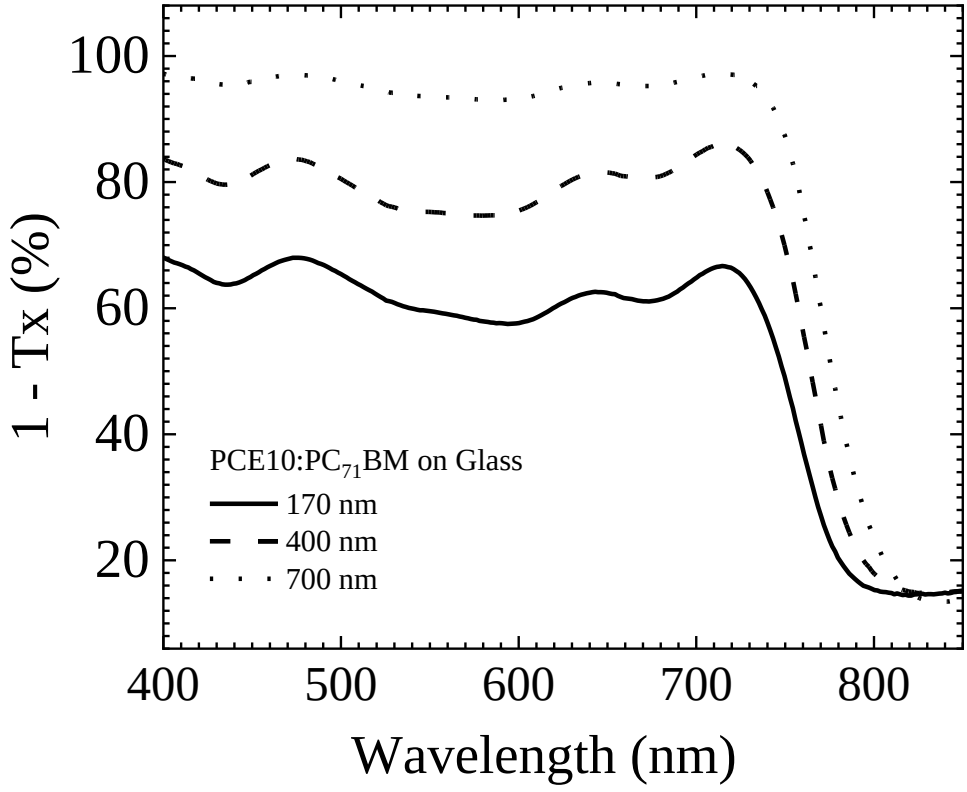

Figure 45. Absorption of the PCE10:PC71BM PAL and the thickness attained through spin coating of the solution on glass. Measured in air.

4.2.1 J-V Curves under Dark Condition of Thick PCE10:$PC_{71}BM$ NIR OPD

The optimization of the thickness is evaluated through the *J-V* curves considering the previous results in which the high ratio values between the shunt and series resistance R_P/R_S minimize noise. **Figure 46 (top)** shows *J-V* curves for the PAL thicknesses of 50 nm (25 mg/mL when PCE10:$PC_{71}BM$ is in form of solution), and **Figure 46 (bottom)** shows *J-V* curves for the PAL thicknesses of 400 nm (50 mg/mL when PCE10:$PC_{71}BM$ is in form of solution). These PAL thicknesses (50 nm and 400 nm) yield OPDs with low shunt resistance R_P values, poor repeatability of the *J-V* curves, and low yield in the number of OPDs. Some of these observations (low R_P, poor repeatability, and low yield) on thin PAL OPDs have been attributed in the past to defects, pinholes, bubbles, and ITO spikes [120]. Therefore, PAL thicknesses of 50 nm and 400 nm will not be considered any longer for additional characterization procedures.

On the other hand, **Figure 47 (top)** shows *J-V* curves for the PAL thicknesses of 700 nm (70 mg/mL when PCE10:$PC_{71}BM$ is in form of solution), and **Figure 47 (bottom)** shows *J-V* curves for the PAL thicknesses of 1150 nm (100 mg/mL when PCE10:$PC_{71}BM$ is in form of solution). These PAL thicknesses (700 nm and 1150 nm) yield OPDs with high shunt resistance R_P values, an acceptable repeatability of the *J-V* curves, and high yield in the number of OPDs. This has been a strategy used in relatively recent times for the optimization of broadband OPDs with sensitivity in the visible range only [5, 120], and for narrowband OPDs with sensitivity in the NIR for materials different than a PAL comprised of PCE10:$PC_{71}BM$ OPDs [121-123] .

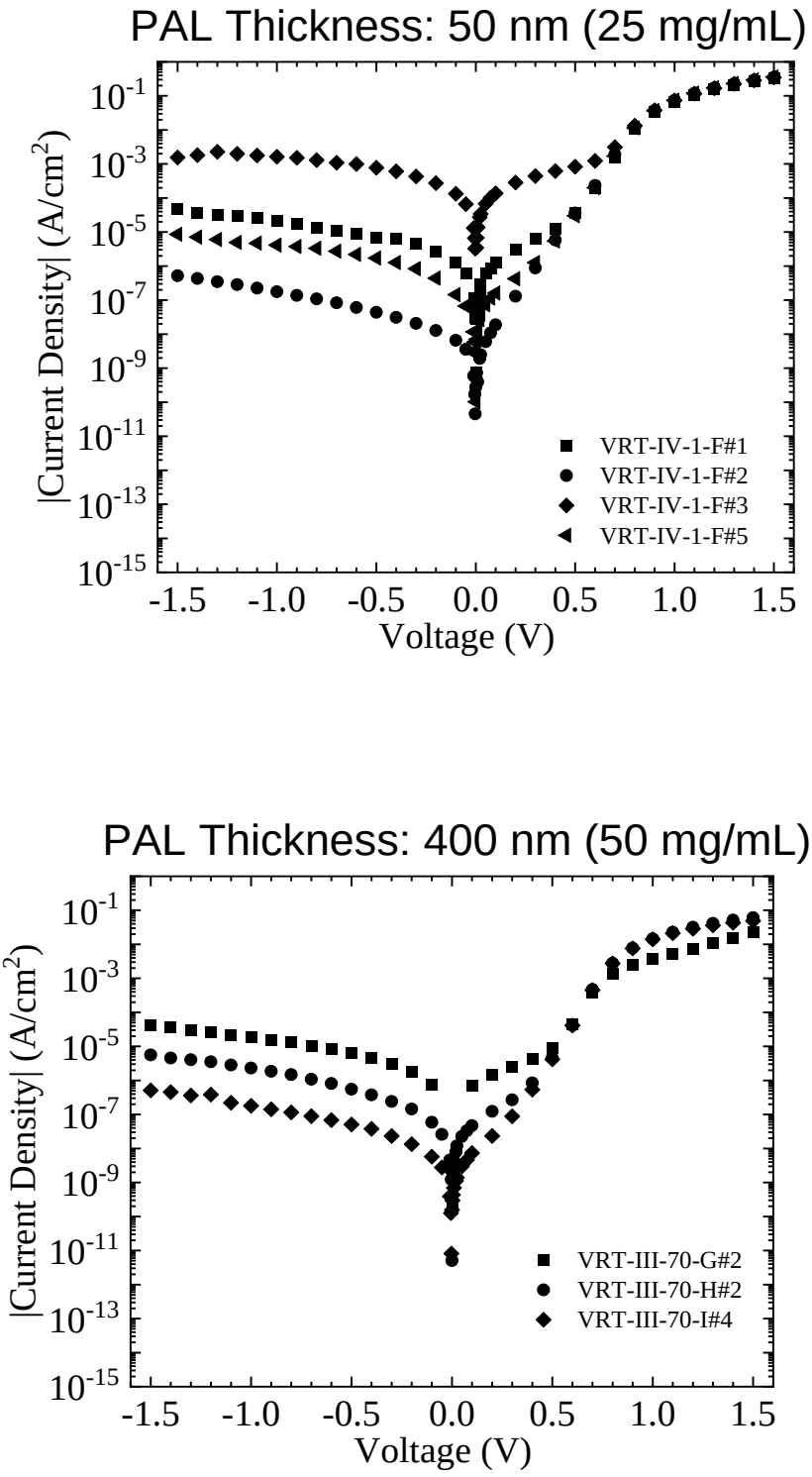

Figure 46. Measured *J*-*V* curves for NIR OPDs with relatively thin PAL thicknesses. Top: 50 nm (25 mg/mL in solution). Bottom: 400 nm (50 mg/mL in solution). Photoactive area is A = 0.1 cm^2. Measured in a N_2-filled glovebox.

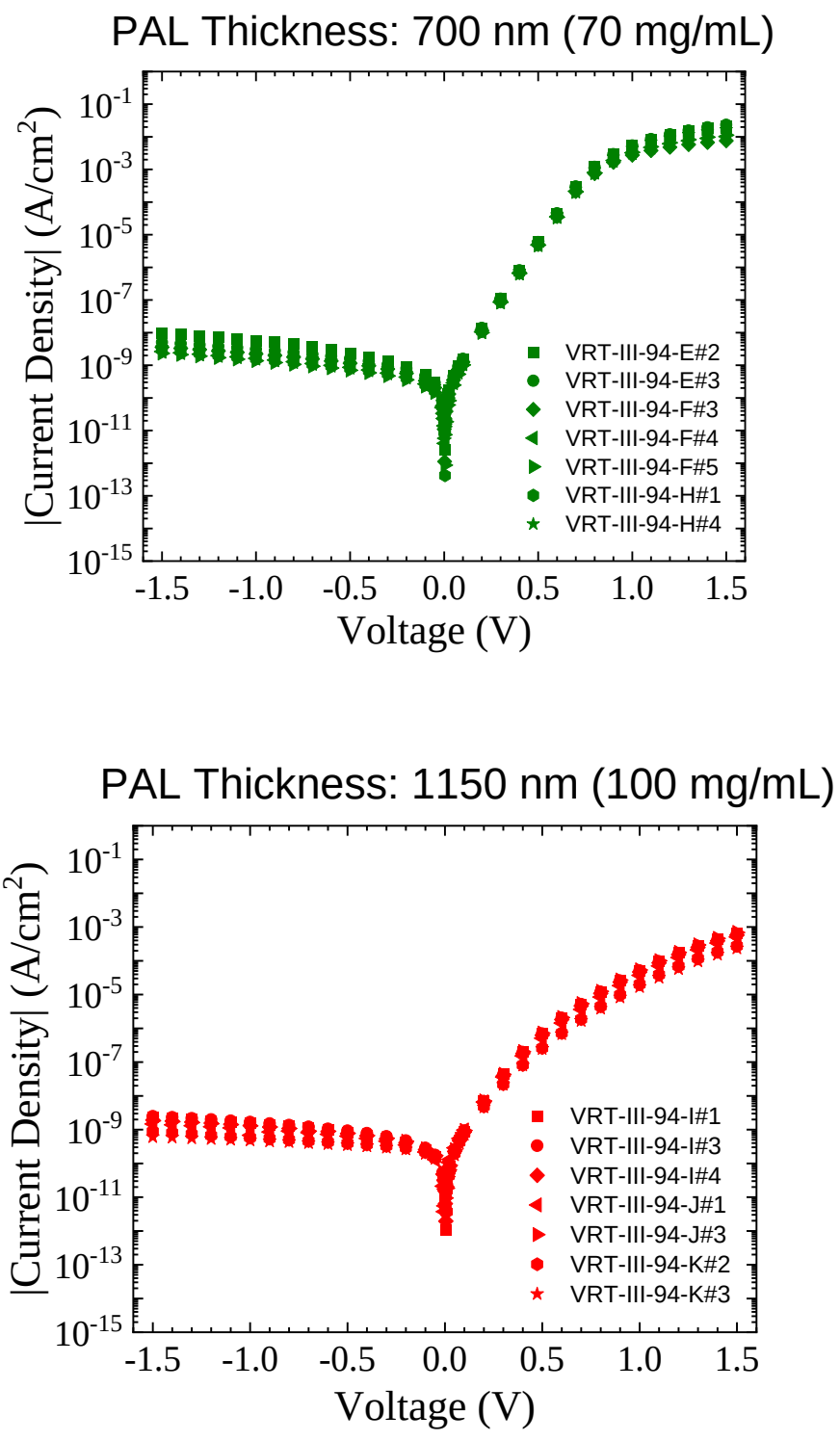

Figure 47. Measured *J-V* curves for NIR OPDs with relatively thick PAL thicknesses. Top: 700 nm (70 mg/mL in solution). Bottom: 1150 nm (100 mg/mL in solution). Photoactive area is A = 0.1 cm^2. Measured in a N_2-filled GB.

By using a light source of a wavelength λ = 735 nm, one of the OPDs with PAL thickness of 700 nm (70 mg/mL when PCE10:$PC_{71}BM$ is in form of solution) is measured and fitted with the Prince model as displayed in **Figure 48**. From this modelling procedure, the reverse saturation current value J_0 = 190 pA/cm^2 and the ideality factor n = 1.48 are obtained. Next, the series resistance R_S and shunt resistance R_P values are also obtained from the fitting of *J-V* curves in the dark (**Figure 47**) with the Prince model (**Figure 48** and **Figure 49**). The values for the minimum, maximum and median *J-V* curves for PAL thicknesses of 700 nm and 1150 nm are summarized in **Table 8**.

From **Table 8**, the series resistance R_S in OPDs with PAL thicknesses of 1150 nm is at least one order of magnitude higher than in OPDs with PAL thicknesses of 700 nm. This is consistent with the current density J_{DARK} values in forward bias which have an order of magnitude of difference between thicknesses of 700 and 1150 nm at 1.5 V. On the other hand, the shunt resistance R_P values for both PAL thicknesses are at around the same order of magnitude as observed in **Table 8**.

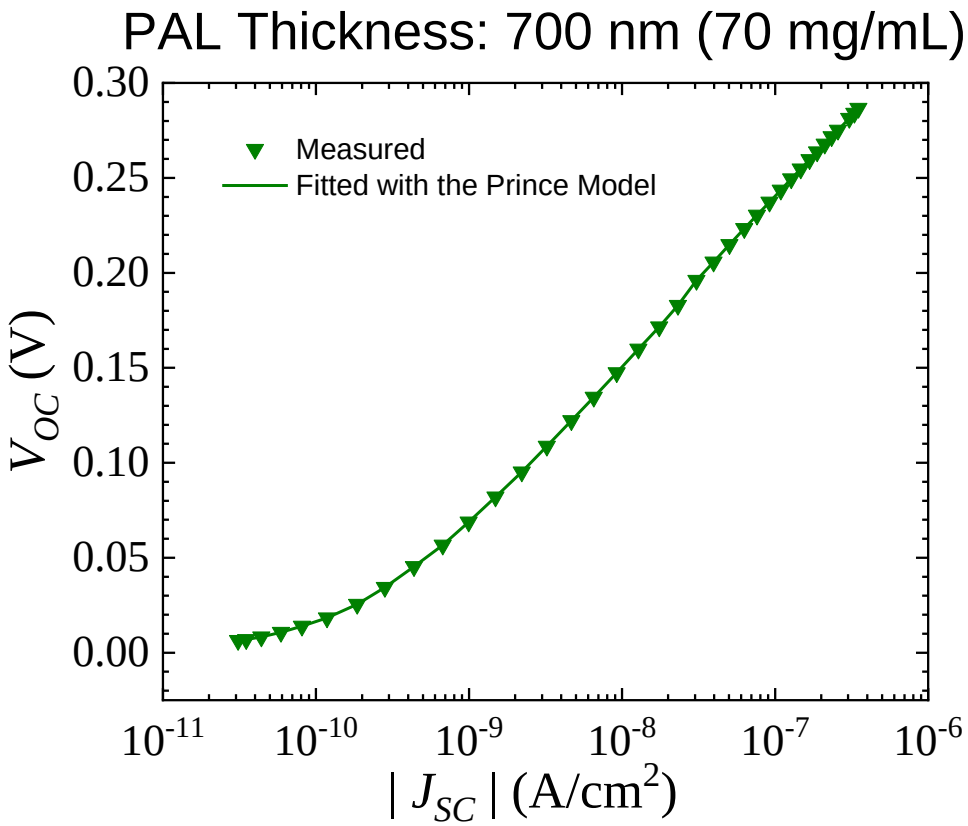

Figure 48. Measured V_{OC}-J_{SC} curve for a NIR light source (λ = 735 nm) for an OPD with PAL thickness of 700 nm (70 mg/mL in solution). Photoactive area is A = 0.1 cm^2. Measured in a N_2-filled glovebox.

Table 8. Electrical parameters obtained from the Prince model [80] for PCE10:$PC_{71}BM$ OPDs with thicknesses of 700 nm and 1150 nm. Photoactive area is A = 0.1 cm^2.

Thickness (nm)	n	J_0 (pA/cm^2)	R_S (Ω)			R_P (Ω)		
			Min.	Med.	Max.	Min.	Med.	Max.
700	1.48	190	1 x 10^3	0.5 x 10^3	0.4 x 10^3	9 x 10^9	5 x 10^9	2 x 10^9
1150			40 x 10^3	15 x 10^3	13 x 10^3	35 x 10^9	9 x 10^9	7 x 10^9

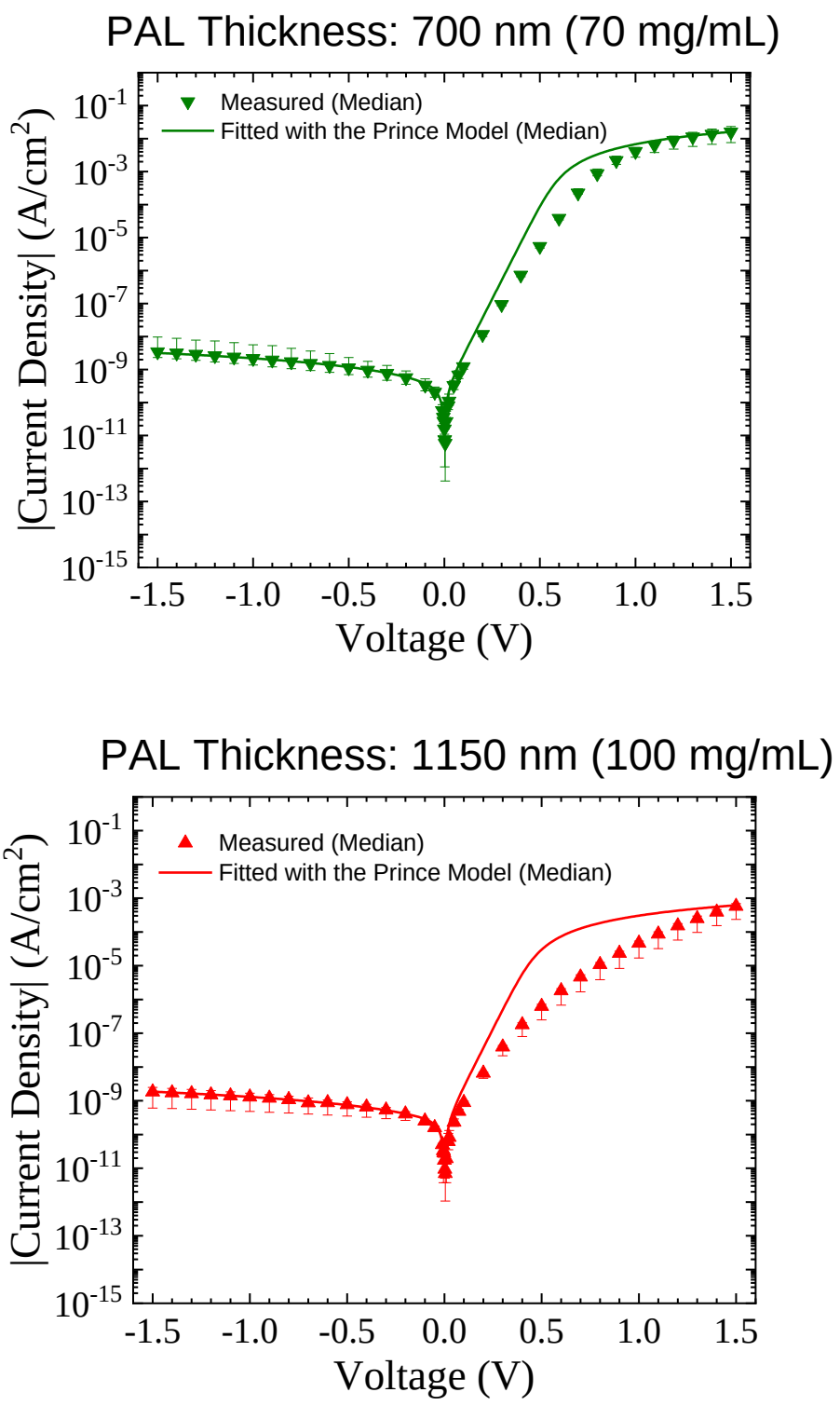

Figure 49. Measured *J-V* curves (median of 7 devices) for PCE10:$PC_{71}BM$ OPDs and their respective simulated *J-V* curves with the Prince model. Top: 700 nm (70 mg/mL in solution). Bottom: 1150 nm (100 mg/mL in solution). Photoactive area is $A = 0.1$ cm^2. Measured in a N_2-filled glovebox.

Table 9. The ratio between the shunt resistance R_P and the series resistance R_S for PCE10:PC$_{71}$BM OPDs with PAL thicknesses of 700 nm and 1150 nm.

Thickness (nm)	R_P / R_S		
	Minimum	Median	Maximum
700	9×10^6	10×10^6	5×10^6
1150	0.9×10^6	0.6×10^6	0.5×10^6

When the ratio R_P/R_S is calculated for the PCE10:PC$_{71}$BM OPDs with thicknesses of 700 nm and 1150 nm (see **Table 9**), it is observed that $R_P/R_S > 10^5$ for all the cases (minimum, median, and maximum values). Therefore, it is expected that $J_{SC}/J_{ph} \rightarrow 1$ for illumination conditions in which $J_{ph} < 1$ nA/cm^2. Overall, the fitting procedure of the *J-V* curves (median) with the Prince model show a correlation between the model and the experimental data for reverse bias conditions. For large voltages in forward bias conditions ($V > 0.2$ V), deviations are observed which could correspond to modifications in the OPDs when radiated and stressed with several measurement scans. As OPDs are expected to operate under unbiased and/or reverse bias conditions, the Prince model seems to be an acceptable equivalent circuit to describe the electrical behaviour of PCE10:PC$_{71}$BM OPDs with thicknesses of 700 nm and 1150 nm.

4.2.2 Responsivity as a Function of Wavelength of Thick PCE10:$PC_{71}BM$ NIR OPDs

The responsivity of PCE10:$PC_{71}BM$ OPDs at high optical power intensities (> 1 μW) for PAL thicknesses of 700 nm and 1100 nm is evaluated for unbiased and biased conditions. The optical source used is an LED with a central wavelength value λ = 735 nm.

4.2.2.1 Responsivity at High Optical Powers under Unbiased Conditions

Under unbiased conditions, measurements of PCE10:$PC_{71}BM$ OPDs with PAL thicknesses of 700 nm are displayed in **Figure 50**. These OPDs show sensitivity not only in the visible range of the electromagnetic spectrum, but also in the NIR up to λ = 850 nm. The responsivity peak is 157 mA/W at λ = 750 nm and the calculated *EQE* value at this wavelength is 26%. At λ = 653 nm (testing LASER source), the responsivity value is 94 mA/W and the *EQE* value is 18%. At λ = 735 nm (testing LED source), the responsivity value is 137 mA/W and the *EQE* value is 23%.

On the other hand, PCE10:$PC_{71}BM$ OPDs with PAL thicknesses of 1150 nm are presented in **Figure 51**. The increment of thickness yields OPDs with narrowband sensitivity between λ = 720 nm and λ = 820 nm. The responsivity peak is 78 mA/W at λ = 765 nm and the calculated *EQE* value at this wavelength is 13%. At λ = 653 nm (testing LASER source), the responsivity value is 12 mA/W is 2%. At λ = 735 nm (testing LED source), the responsivity value is 29 mA/W and the *EQE* value is 5%.

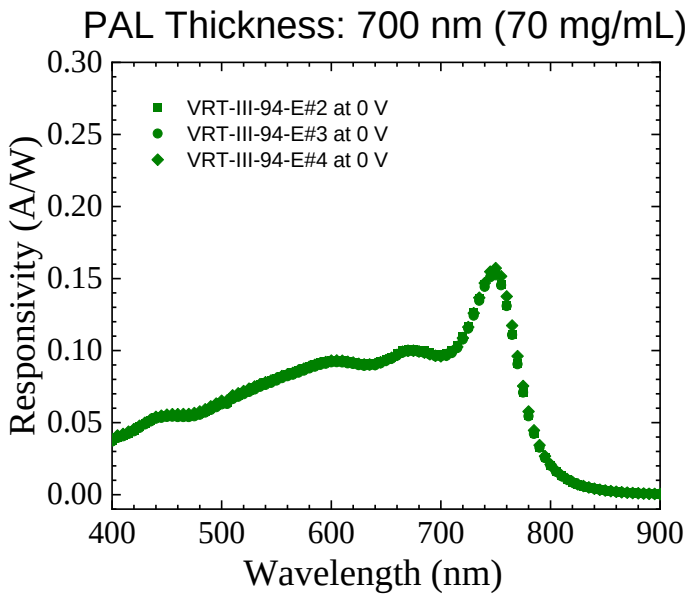

Figure 50. Measured responsivity of PCE10:$PC_{71}BM$ OPDs with PAL thickness of 700 nm (70 mg/mL in solution). Photoactive area is A = 0.1 cm^2. OPDs were measured at 0 V in air.

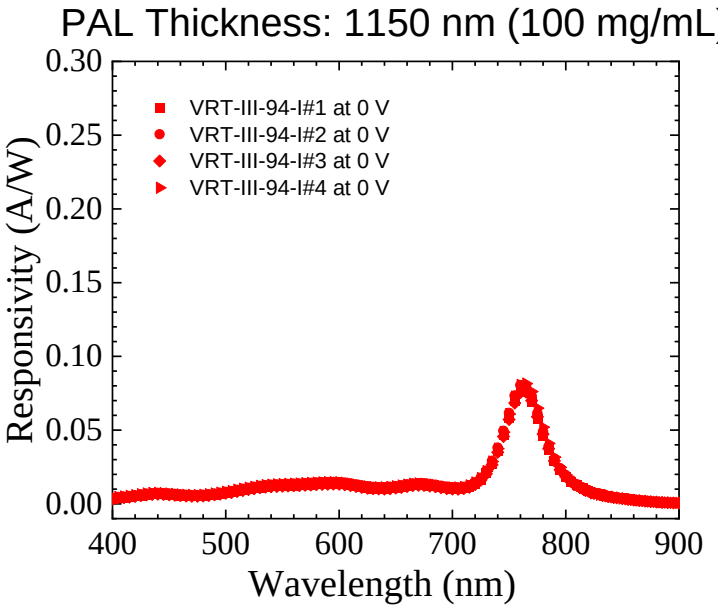

Figure 51. Measured responsivity of PCE10:$PC_{71}BM$ OPDs with PAL thickness of 1150 nm (100 mg/mL in solution). Photoactive area is A = 0.1 cm^2. OPDs were measured at 0 V in air.

Figure 52 shows that the responsivity of PCE10:$PC_{71}BM$ OPDs for the two evaluated PAL thicknesses (700 nm and 1150 nm) overlaps for wavelengths λ > 780 nm, but it differs significatively for the rest of the visible and NIR regions of the electromagnetic spectrum. The previous modelling of the *J-V* curves under dark condition (**Table 8**) have enabled to extract series resistance (R_S) values of PCE10:$PC_{71}BM$ OPDs that range 400 Ω < R_S < 400 kΩ. As expected, the thickest OPDs (1150 nm) are the most resistive ones; shunt resistance (R_P) values 2 GΩ < R_P < 35 GΩ. The thickest OPDs (1150 nm) have the highest values; a reverse saturation current value J_0 = 190 pA/cm^2 with the assumption that J_0 is not deeply impacted (i.e., change of the value by one order of magnitude) by the variation of the PAL thickness; shunt and series resistance ratio values (R_P / R_S) that span 0.5 x 10^6 < R_P / R_S < 10 x 10^6 (**Table 9**).

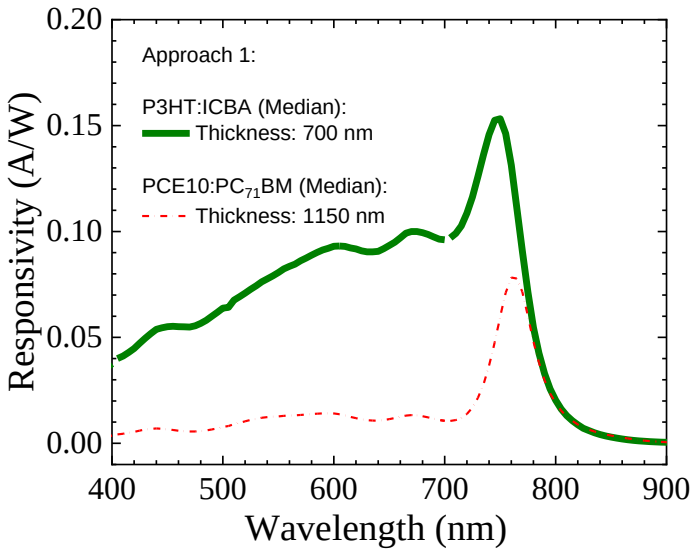

Figure 52. Measured responsivity of PCE10:$PC_{71}BM$ OPDs with PAL thickness of 700 nm (70 mg/mL in solution – 4 devices) and 1150 nm (100 mg/mL in solution – 3 devices). Photoactive area is *A* = 0.1 cm^2. OPDs were measured at 0 V in air.

Considering these values and simulations of the Prince model for J_{SC}/J_{ph} (**Figure 40** - **Figure 42**), it is suggested that responsivity changes as a function of the thickness, obeys mainly to changes in J_{ph} as a function of wavelength rather than changes in the extracted value of R_S, R_P and/or R_P/R_S. This effect, a.k.a. charge collection narrowing (CCN) effect [121], has been reported for systems different than the ones based on PCE10:$PC_{71}BM$ and it has been exploited for the fabrication of narrowband OPDs [122].

4.2.2.2 Responsivity at High Optical Powers under Relevant Reverse Bias Conditions

Under biased conditions (V = -0.1 V, -0.5 V, -1 V, -1.5 V), measurements of normalized (with respect to the responsivity values at unbiased conditions) responsivity values as a function of wavelength of PCE10:$PC_{71}BM$ OPDs with PAL thicknesses of 700 nm and 1150 nm are presented in **Figure 53** and **Figure 54**, respectively.

Figure 53 shows that for OPDs (PAL thickness of 700 nm) biased with a low applied voltage, V = -0.1 V, the responsivity can increase by a 10% with respect to the value under the unbiased condition for most of the visible range, and it drops to 5% for NIR wavelength values (740 nm < λ < 850 nm). For the next applied voltage, V = -0.5 V, the responsivity increases to a 40% of its value under unbiased conditions in the visible region, whereas in the NIR region (740 nm < λ < 850 nm), the responsivity attains a 20% increment. For an applied voltage V = -1 V, the responsivity in the visible range increases to 70% of its value under unbiased conditions, and to 40% in the NIR region (740 nm < λ < 850 nm). Finally, for an applied voltage V = -1.5 V, the responsivity values in the visible

region double the ones under an unbiased condition, and it attains 60% in the NIR region (740 nm < λ < 850 nm).

As per the narrowband feature of **Figure 54**, analysis will be limited to the wavelength λ values between 700 nm and 850 nm as the responsivity in the visible region of the electromagnetic spectrum is lower than 50 mA/W for all the biased conditions. Special attention is paid to the wavelength, λ = 765 nm, at which the responsivity attains a maximum value of 76 mA/W under an unbiased condition. This value increases by 14% at V = -0.1 V, 40% at V = -0.5 V, 68% at V = -1 V, and 91% at V = -1.5 V.

So far, the approach of increasing the PAL thickness has been able not only to impact positively the J-V characteristic curves (improving repeatability, yield, and R_P/R_S ratio), but also to attain OPDs with narrowband NIR sensitivity. This later feature is at the cost of lower responsivity values (compared to thinner layers), which can be increased through external applied voltages.

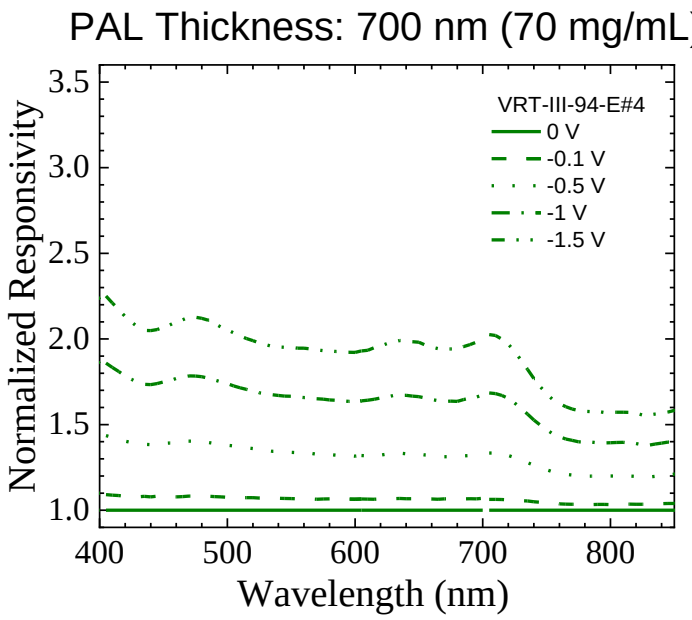

Figure 53. Measured normalized responsivity values (with respect to the unbiased condition) for different applied voltages of PCE10:$PC_{71}BM$ OPDs with PAL thickness of 700 nm. Photoactive area is A = 0.1 cm^2. OPDs were measured in air.

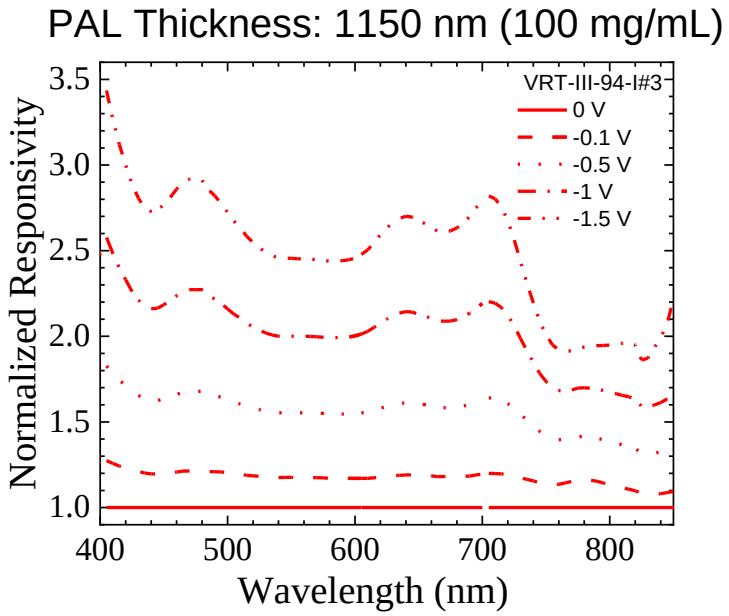

Figure 54. Measured normalized responsivity values (with respect to the unbiased condition) for different applied voltages of PCE10:$PC_{71}BM$ OPDs with PAL thickness of 1150 nm. Photoactive area is A = 0.1 cm^2. OPDs were measured in air.

4.2.3 Noise Measurements on Thick PCE10:$PC_{71}BM$

To attain OPDs with high detectivity values, it is important not only to maximize the responsivity, but also to reduce the noise. In the measurements, the instrument's sampling rate should be monitored. If the sampling rate changes, the measured noise can change. For example, **Figure 55** shows the current residuals for a resistor with a nominal value of 1 GΩ. The background DC current has been removed for each applied voltage condition so al the RMS values will be obtained from the residuals that oscillates around 0 A. It is observed that when the average current is lower than 100 pA, the RMS noise current value remains mostly constant and the bandwidth value is B = 1.5 ± 0.5 Hz. For average DC currents greater than 100 pA (1 nA/cm^2 for an area of 0.1 cm^2), the RMS current amplitude increases and the bandwidth becomes B = 11 Hz. These bandwidth values will be selected according to the levels of DC currents when OPDs are measured.

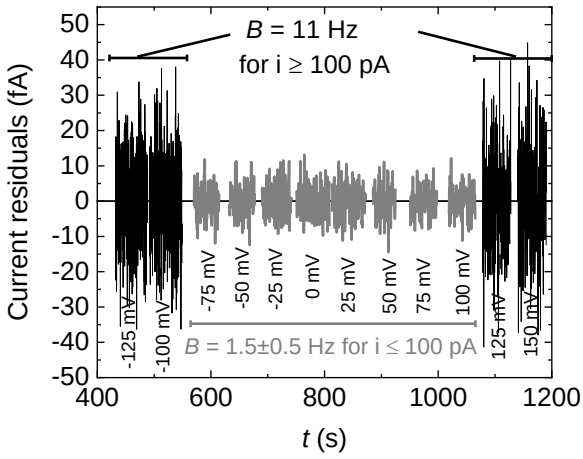

Figure 55. Measured noise for a resistor with nominal value of 1 GΩ. Current residuals are obtained after removing DC current components from the measurements in time. Measurements were done at the Georgia Institute of Technology by Dr. Canek Fuentes-Hernandez.

4.2.3.1 Noise Measurements under Unbiased Conditions – Thick Devices

Noise measurements can be quantified through the RMS value of the current [71]. First, the bandwidth range should be first verified according to the discussion in the previous section and measurements in **Figure 55**. This bandwidth in our measurements is determined by the levels of DC current as it will be 1.5 Hz if the average current is lower than 100 pA, and 11 Hz if the average current if the current is higher than 100 pA. As shown in **Figure 56**, DC current in PCE10:$PC_{71}BM$ OPDs with thicknesses of 700 nm and 1150 nm are lower than 100 pA and then B = 1.5 Hz.

It is important to note that, theoretically, the DC current under unbiased conditions is expected to be zero. However, according to the measurements displayed in **Figure 56,** the currents for seven PCE10:$PC_{71}BM$ OPDs oscillate between 1 pA and 4 pA for both PAL thicknesses (700 nm and 1150 nm). Many sources can contribute to generate this current: background illumination that cannot be eliminated during the measurement, thermal generated carriers that flow due to the contrast of WF in the OPDs, and/or small electrical offsets of the measurement system.

On the other hand, **Figure 57** displays statistical information of the measured I_{rms} for PCE10:$PC_{71}BM$ OPDs with both PAL thicknesses (700 nm and 1150 nm). Measured I_{rms} values are comparable (values between 10 fA and 100 fA). Measured I_{rms} values contrast with the white noise $I_{rms.white}$ predicted by the Prince model [80] which are summarized in **Table 10**. The one to two orders of magnitude difference between I_{rms} and $I_{rms.white}$ suggest that for the experimental condition (e.g., sampling of the measurement instrument), other sources of noise are dominant, presumably, Flicker noise.

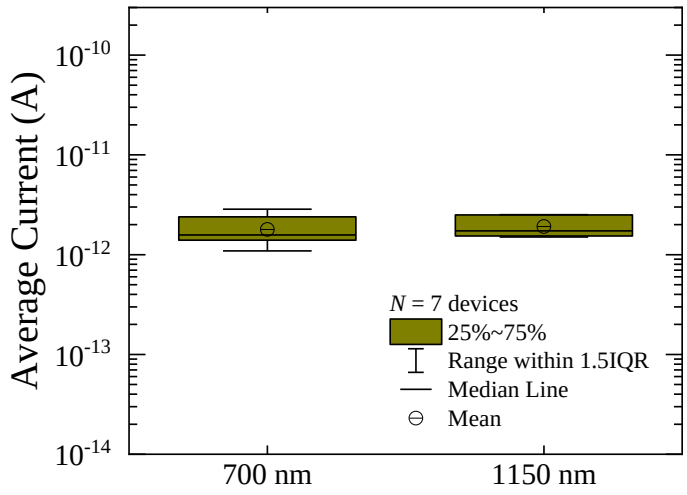

Figure 56. Measured average current under unbiased conditions of PCE10:$PC_{71}BM$ OPDs with PAL thickness of 700 nm and 1150 nm. Green and red symbols on the left of the boxes represent the individual measurements for seven OPDs. Photoactive area is A = 0.1 cm^2. OPDs were measured under an unbiased condition in a N_2-filled box.

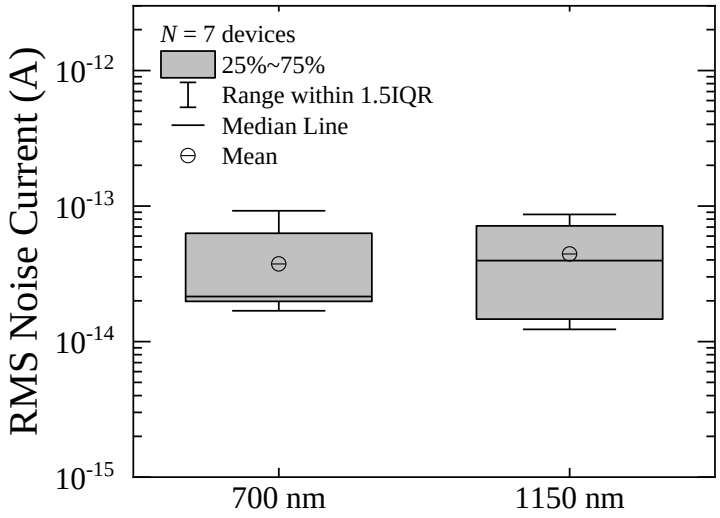

Figure 57. Measured RMS current under unbiased conditions of PCE10:$PC_{71}BM$ OPDs with PAL thickness of 700 nm and 1150 nm. Green and red symbols on the left of the boxes represent the individual measurements for seven OPDs. Photoactive area is A = 0.1 cm^2. OPDs were measured under an unbiased condition in a N_2-filled box.

Table 10. Calculated RMS noise current values based on the electrical parameters obtained from the Prince model [80] for approach 1. For the calculations: T = 25 °C. A: 0.1 cm^2.

Thickness (nm)	Shot RMS Noise Current $I_{rms,shot}$ (fA)	Thermal RMS Noise Current $I_{rms,thermal}$ (fA)			White RMS Noise Current $I_{rms,white}$ (fA)		
		Min.	Med.	Max.	Min.	Med.	Max.
700	4.3	1.6	2.2	3.7	4.6	4.8	5.6
1150		0.8	1.6	1.9	4.3	4.6	4.7

4.2.3.2 Noise Measurements under Relevant Bias Conditions – Thick Devices

Next**,** the RMS noise currents for seven PCE10:$PC_{71}BM$ OPDs for PAL thicknesses of 700 nm (**Figure 58**) and 1150 nm (**Figure 59**) are evaluated from different reverse bias conditions. A dashed line has been traced to mark the change of bandwidth in the measurements. Measurements below this line will have an associated bandwidth of B = 1.5 Hz, while measurements about the line will have an associated bandwidth of B = 11 Hz. For the PAL thickness of 700 nm (**Figure 58**), measurements of the average current determine that at the bias condition of -0.1 V, B = 1.5 Hz. When the bias condition is -1.0 V and -1.5 V (and increment of the responsivity is the largest), B = 11 Hz. For the bias condition of -0.5 V, most of the measurements will have B = 11 Hz as the per the median of the measurements. Some outliers for voltages at -1 V and -1.5 V are observed. On the other hand, for the PAL thickness of 1150 nm (**Figure 59**), measurements of the average current determine that at the bias condition of -0.1 V and -0.5 V, B = 1.5 Hz. For bias conditions of -1 V and -1.5 V, most of the measurements are done at B = 11 Hz as the per the median of the measurements. These B values are important to explain potential differences in measurements of RMS noise currents. No outliers were registered.

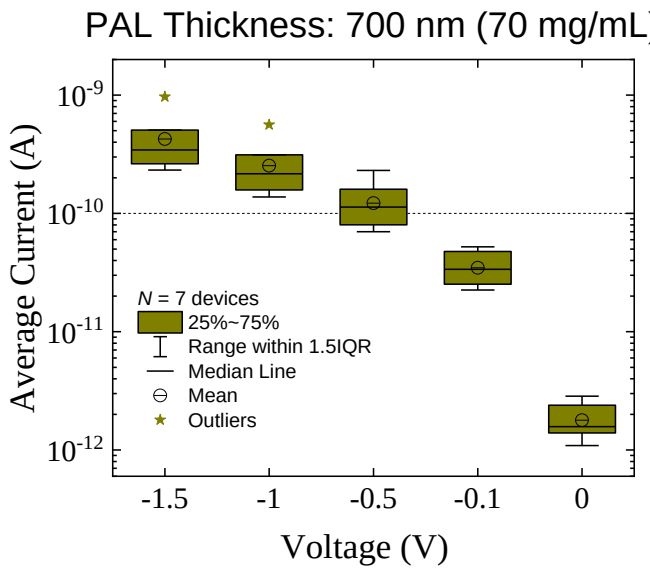

Figure 58. Measured average currents measured under unbiased and biased conditions of PCE10:$PC_{71}BM$ OPDs with PAL thickness of 1100 nm. Green symbols on the left of the boxes represent the individual measurements. Photoactive area is *A* = 0.1 cm^2. Seven OPDs were measured in a N_2-filled box.

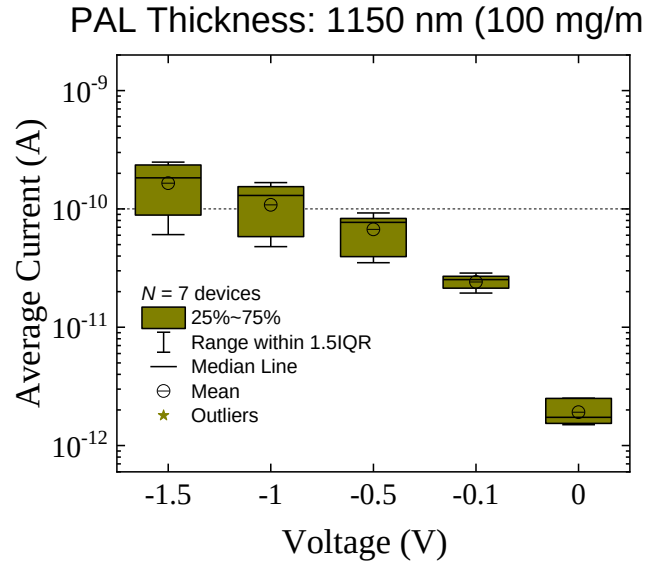

Figure 59. Measured average currents measured under unbiased and biased conditions of PCE10:$PC_{71}BM$ OPDs with PAL thickness of 1150 nm. Red symbols on the left of the boxes represent the individual measurements. Photoactive area is *A* = 0.1 cm^2. Seven OPDs were measured in a N_2-filled box.

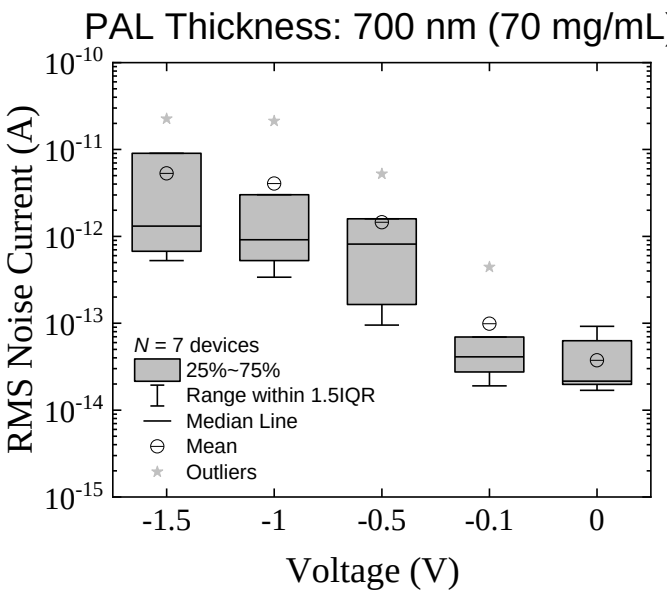

Figure 60. Measured RMS noise currents measured under unbiased and biased conditions of PCE10:$PC_{71}BM$ OPDs with PAL thickness of 700 nm. Green symbols on the left of the boxes represent the individual measurements for seven OPDs. Photoactive area is A = 0.1 cm^2. OPDs were measured in a N_2-filled box.

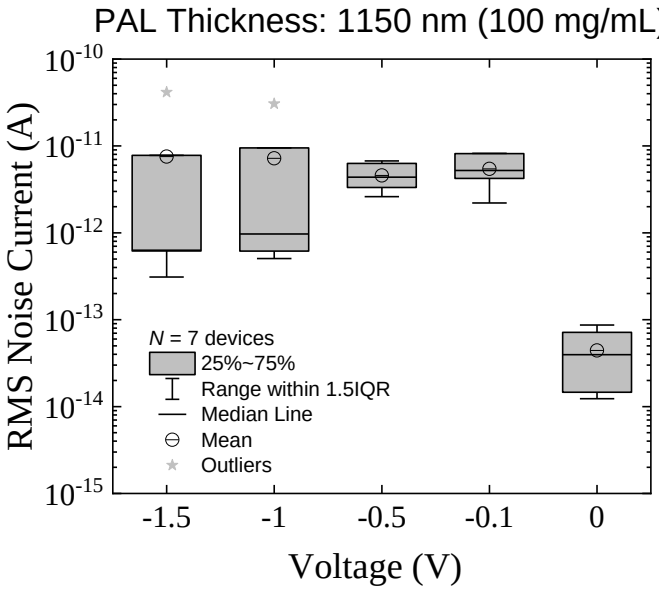

Figure 61. Measured RMS noise currents measured under unbiased and biased conditions of PCE10:$PC_{71}BM$ OPDs with PAL thickness of 1150 nm. Red symbols on the left of the boxes represent the individual measurements for seven OPDs. Photoactive area is A = 0.1 cm^2. OPDs were measured in a N_2-filled box.

Once the bandwidth has been established, the RMS noise current values at various bias conditions are extracted from the temporal response of the current measured under dark condition. PCE10:$PC_{71}BM$ OPDs with PAL thickness of 700 nm and 1150 nm are shown in **Figure 60** and **Figure 61**, respectively,

For PCE10:$PC_{71}BM$ OPDs with PAL thickness of 700 nm (**Figure 60**), the distribution of measurements is relatively narrow for 0 V and -0.1 V with respect to the rest of the reverse bias conditions. An increment of the RMS noise current (median value) from 20 fA at 0 V to 40 fA at -0.1 V is registered and the bandwidth for these measurements is B = 1.5 Hz. At -0.5 V, -1 V, and -1.5 V, the RMS noise current (median) values are in the order of 800 fA, 900 fA, and 1 pA, respectively, and most of these measurements have a bandwidth of B = 11 Hz, which can explain at some extent the increment of the RMS noise current values. Few of the measurements at -0.5 V are taken by the instrument at a bandwidth B = 1.5 Hz.

For PCE10:$PC_{71}BM$ OPDs with PAL thickness of 1150 nm (**Figure 61**), the distribution of measurements is relatively narrow for 0 V, -0.1 V, and -0.5 V. All these measurements are taken for a bandwidth B = 1.5 Hz. The RMS noise current (median) values increment from 40 fA at 0 V, to 5 pA at -0.1 V and 4 pA at -0.5 V. At bias -1 V and -1.5 V, the RMS noise current (median) values are in the order of 1 pA and 0.6 pA, respectively. For the latest bias conditions (-1 V and -1.5 V), some of the measurements are measured at a bandwidth of B = 1.5 Hz, and the remaining at a bandwidth B = 11 Hz. This explains the higher data dispersion of data.

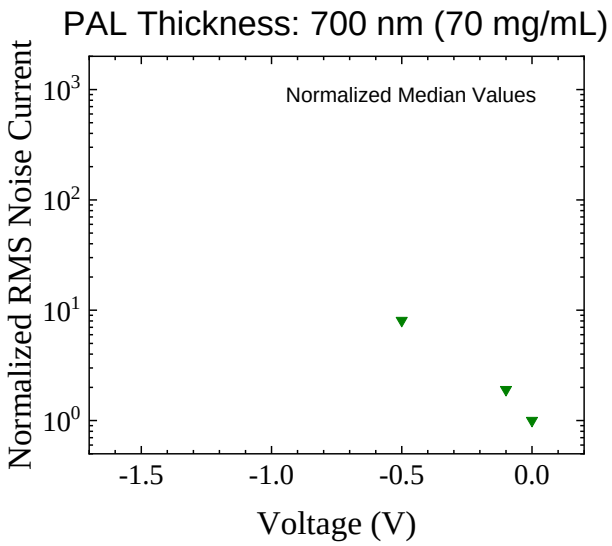

Figure 62. Measured normalized RMS noise current (median values) of PCE10:$PC_{71}BM$ OPDs with PAL thickness of 700 nm as a function of a reverse bias. Normalization is done with respect to the RMS noise current (median value) of the unbiased condition. Only devices with a bandwidth B = 1.5 Hz were considered. Photoactive area is A = 0.1 cm^2. OPDs were measured in a N_2-filled box.

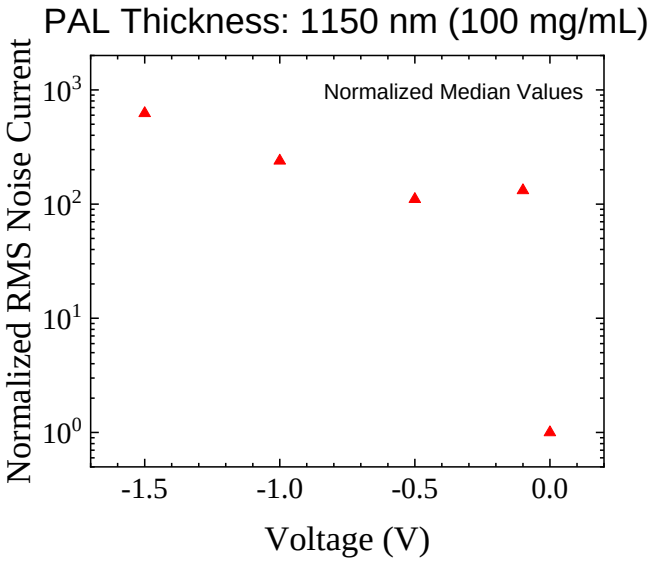

Figure 63. Measured normalized RMS noise current (median values) of PCE10:$PC_{71}BM$ OPDs with PAL thickness of 1150 nm as a function of a reverse bias. Normalization is done with respect to the RMS noise current (median value) of the unbiased condition. Only devices with a bandwidth B = 1.5 Hz were considered. Photoactive area is A = 0.1 cm^2. OPDs were measured in a N_2-filled box.

In order to make a fair comparison, only data taken at a bandwidth B = 1.5 Hz is displayed in **Figure 62** and **Figure 63** for PCE10:$PC_{71}BM$ OPDs with PAL thicknesses of 700 nm and 1150 nm, respectively. The RMS noise current (median) values at the reverse bias conditions were normalized with respect to the unbiased condition.

For PCE10:$PC_{71}BM$ OPDs with PAL thicknesses of 700 nm (**Figure 62**), normalized RMS noise values at B = 1.5 Hz were obtained only for -0.1 V and -0.5 V. For these voltages, normalized RMS values increment, with up to 10 approximately times (at -0.5 V) with respect to the unbiased condition. This contrasts with the slower increment of the responsivity which is approximately 1.5 times at -0.5 V (see **Figure 53**).

On the other hand, for PCE10:$PC_{71}BM$ OPDs with PAL thicknesses of 1150 nm (**Figure 63**), normalized RMS noise current values were obtained for all the reverse bias conditions. Note that the normalized RMS noise current increments faster than for OPDs with PAL thicknesses of 700 nm. Increments are in the between 100 and 600 times for all the reverse bias conditions. This increment contrasts with the slower increment of responsivity which is approximated 2 times (see **Figure 54**) for the wavelengths of interest (700 nm – 800 nm).

Although it has been shown that responsivity can depend on the light intensity, this variation can both amplify or attenuate the values of the responsivity in OPDs [5]. Then, it is not ensured that an applied external voltage improves overall the detectivity of the OPD. Therefore, only the unbiased condition, in which the RMS noise current is at its lowest value, will be evaluated.

4.2.4 Light-Intensity Experiments on Thick PCE10:$PC_{71}BM$ OPDs

PCE10:$PC_{71}BM$ OPDs with two different PAL thicknesses (700 nm and1150 nm), show that the predicted (**Table 10**) and the measured (**Figure 57**) RMS noise current values under unbiased conditions are comparable. Median values of RMS noise currents are slightly lower for PCE10:$PC_{71}BM$ OPDs with a PAL thickness of 700 nm with respect to the ones with a PAL thickness of 1150 mm. The ratio between the shunt and series resistances values R_P/R_S is approximately one order of magnitude higher for PCE10:$PC_{71}BM$ OPDs with a PAL thickness of 700 nm with respect to the ones with a PAL thickness of 1150 nm.

Finally, the NIR optical source available is at a wavelength of λ = 735 nm. At this wavelength, the responsivity at high optical power intensities in PCE10:$PC_{71}BM$ OPDs with a PAL thickness of 700 nm is higher (140 mA/W) than for a PAL thickness of 1150 nm (28 mA/W). Then, only the former case will be further characterized to establish the limits of detection at low optical power intensities of broadband PCE10:$PC_{71}BM$ OPDs. This decision is made despite acknowledging that for monochromatic detection, narrowband PCE10:$PC_{71}BM$ OPDs can be a better choice to avoid noise associated to other sources of light (e.g., background illumination) at wavelengths different than the signal's one.

4.2.4.1 RMS Noise Current and Signal-to-Noise Ratio (SNR) as a Function of Light Intensity – Thick OPDs

The RMS noise current under a unbiased condition is measured as a function of the illumination and shown in **Figure 64**. All the values are measured at a bandwidth B = 1.5 Hz. For this specific device, the RMS has variations around 12 fA. This value is not far from the RMS noise current value obtained from 7 replicas with a median value of 21 fA under dark condition. No increasing or decreasing trends for the RMS noise current values were observed within the evaluated optical power range (1 fW – 10 pW) in **Figure 64**.

Next, the signal-to-noise ratio for the current ($SNR_{current}$) is obtained from the ratio between the measured photogenerated current (which is obtained after the subtraction of the dark current from the photocurrent), and the RMS noise current for each illumination condition. The results of these measurements are displayed in **Figure 65**.

4.2.4.2 Noise Equivalent Power (*NEP*) and Specific Detectivity (*D**) – Thin OPDs

An extrapolation of the approximately linear behavior of *SNR* as a function of the optical power would indicate that the noise equivalent power (*NEP*), which is the optical power in which *SNR* = 1, would be *NEP* = 55 fW, approximately. While this method can be handy when *SNR* is known as a function of optical power, more statistical information is required to be involved.

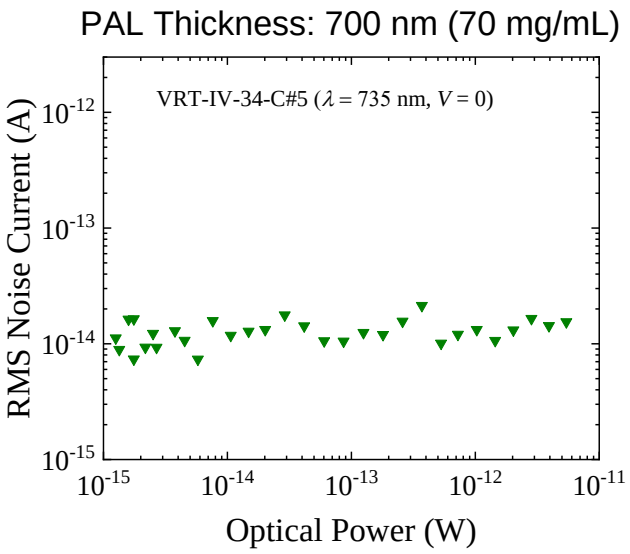

Figure 64. Measured RMS noise current as a function of optical power of a PCE10:$PC_{71}BM$ OPD with PAL thickness of 700 nm. Photoactive area is A = 0.1 cm^2. OPDs were measured under unbiased condition in a N_2-filled box. Optical source is an LED at λ = 735 nm.

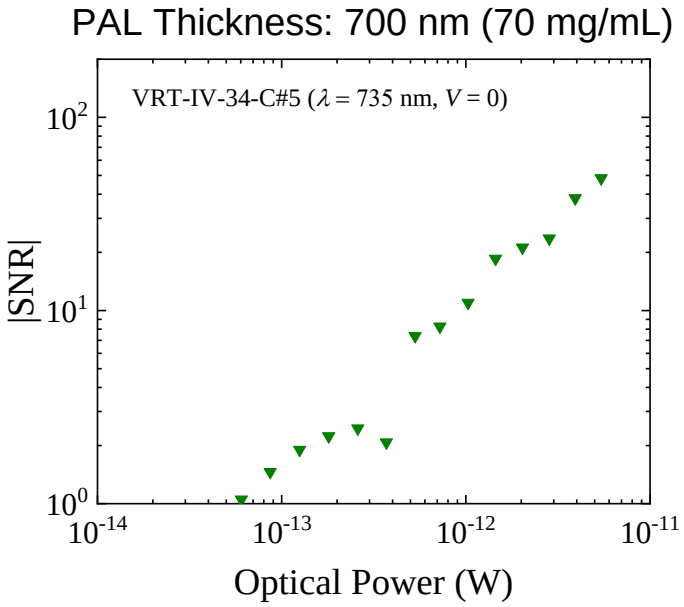

Figure 65. Measured SNR for different optical power values of a thick PCE10:$PC_{71}BM$ OPD with PAL thickness of 700 nm. Photoactive area is A = 0.1 cm^2. OPDs were measured under unbiased condition in a N_2-filled box. Optical source is an LED at λ = 735 nm.

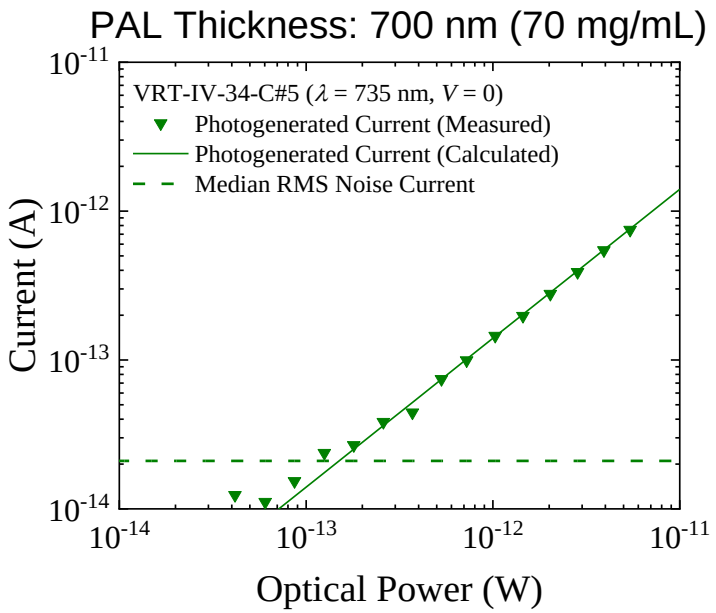

Figure 66. Measured and calculated photogenerated current as a function of optical power of a thick PCE10:$PC_{71}BM$ OPD with PAL thickness of 700 nm. Photoactive area is A = 0.1 cm^2. OPDs were measured under an unbiased condition in a N_2-filled box. Optical source is an LED at λ = 735 nm.

Table 11. Measured and calculated *NEP* and *D for a thick PCE10:$PC_{71}BM$ OPD (PAL thickness of 700 nm) under an unbiased condition for λ = 735 nm. Photoactive area is A = 0.1 cm^2. Measurement bandwidth is B = 1.5 Hz.**

	Calculated Φ-Independent $\Re$ = 0.14 A/W	**Measured Φ-Dependent $\Re$ in Figure 66**
Calculated (median) $I_{rms,white}$ = 5 fA	D^* = 10.8 x 10^{12} cm $Hz^{0.5}$/W (NEP = 36 fW)	Measurement out of range
Measured (median) $I_{rms,white}$ = 20 fA	D^* = 2.58 x 10^{12} cm $Hz^{0.5}$/W (NEP = 150 fW)	D^*= 3.10 x 10^{12} cm $Hz^{0.5}$/W (NEP = 125 fW)

On the other hand, when the measured photogenerated current I_{ph} (see **Figure 66**) of an OPD matches the median value of the measured RMS noise current I_{rms} obtained from different devices under dark condition (assumption: light-independent RMS noise current), the result might be slightly different. From this type of characterization, the obtained *NEP* = 125 fW. This value diverges from the assumption that the responsivity is independent of the light intensity, in which case *NEP* = 150 fW.

All the discussed *NEP* values considered other sources of noise different than the white noise. When the dominant noise source is the white noise (calculated from the Prince model), the *NEP* = 36 fW. A summary of the different *NEP* values with their respective specific detectivities *D** is presented in **Table 11**.

The *NEP* and *D** values in **Table 11** show the relevance of the proper measurement of the noise that is actually present in the OPDs as well as the dependence of the responsivity on the light intensity. Neglecting sources of noise beyond the white noise might overestimate performance parameters such as *NEP* and *D** of OPDs up to one order of magnitude. While a more extensive statistical study can improve the accuracy of the performance parameters, the values presented illustrate the importance of establishing correct protocols that enable to compare different photodetection technologies.

4.2.5 Summary of Results for Approach 1 and Benchmark with State-of-the-Art OPDs

The approach based on the increment of the PAL thickness (approach 1) has successfully yield PCE10:$PC_{71}BM$ OPDs with calculated RMS white noise $I_{rms,white}$ = 5 – 6 fA (at a bandwidth B = 1.5 Hz) and a measured RMS noise current I_{rms} in the tens of fA for different PAL thicknesses (700 nm and 1150 nm) and same ECE and HCE. Furthermore, approach 1 has yield not only broadband PCE10:$PC_{71}BM$ OPDs with sensitivity in the visible and the NIR regions (up to λ = 850 nm), but also narrowband PCE10:$PC_{71}BM$ OPDs with sensitivity in the NIR only (up to λ = 850 nm). By using the Prince model [80], it is found that approach 1 yield broadband and narrowband NIR OPDs with improved R_P (up to the order of GΩ) and higher R_S (up to the order tens of kΩ) values with respect to PCE10:$PC_{71}BM$ OPDs with thinner PAL, while preserving high ratios of $R_P/R_S > 10^5$. Applied external voltages increased I_{rms} at a higher rate than $\Re$ so higher performance is attained for unbiased conditions. It was shown that D^* can be overestimated (up to four times) when assumptions on the noise and the responsivity values are taken instead of their measurements.

Figure 67 summarizes the median values of the responsivity of PCE10:$PC_{71}BM$ OPDs (PAL thicknesses of 700 nm and 1150 nm) and contrast them with those of state-of-the-art P3HT:ICBA OPDs [5]. Although responsivity values of P3HT:ICBA OPDs are at least twice higher than PCE10:PC71BM OPDs in most part of the visible region of the electromagnetic spectrum (400 nm < λ < 620 nm), it is evident the advantage of PCE10:$PC_{71}BM$ OPDs in the NIR region (up to λ = 850 nm): For PCE10:$PC_{71}BM$ OPDs with PAL thicknesses of 700 nm, responsivity values are superior to those of P3HT:ICBA

OPDs for λ > 650 nm; for PCE10:PC71BM OPDs with PAL thicknesses of 1150 nm, responsivity displays a narrowband feature and higher values than P3HT:ICBA OPDs for λ > 720 nm.

Under unbiased condition, the attained noise levels of PCE10:PC71BM OPDs under approach 1 are comparable to those P3HT:ICBA OPDs in the order of tens of fA [5]. Then D^* is measured through *NEP* (B = 1.5 Hz, A = 0.1 cm^2, λ = 735 nm, V = 0) and light intensity experiments obtaining comparable values in the order of 3 x 10^{12} Jones (best performing device) for the PAL thickness of 700 to P3HT:ICBA OPDs (median value) [5] (see **Figure 68**). No measurements were done on the PCE10:PC71BM OPDs with a thickness of 1150 nm because of limitations of the optical sources available which would need to be monochromatic with a central wavelength λ = 760 nm. No other examples of PCE10:PC71BM OPDs measured under unbiased conditions and with PAL thicknesses comparable to the ones used in this dissertation (700 and 1150 nm) were found in the literature (see **Table 3**).

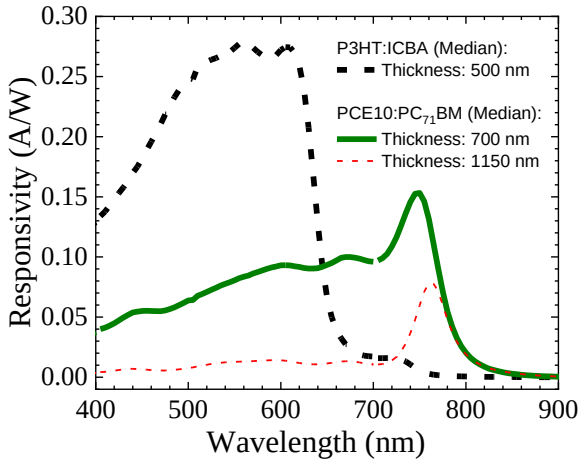

Figure 67. Measured responsivity (median values) of P3HT:ICBA OPDs (3 devices) consistent with [5], and PCE10:PC$_{71}$BM OPDs with PAL thickness of 700 nm (70 mg/mL in solution – 4 devices) and 1150 nm (100 mg/mL in solution – 3 devices). Photoactive area is A = 0.1 cm^2. OPDs were measured at 0 V in air.

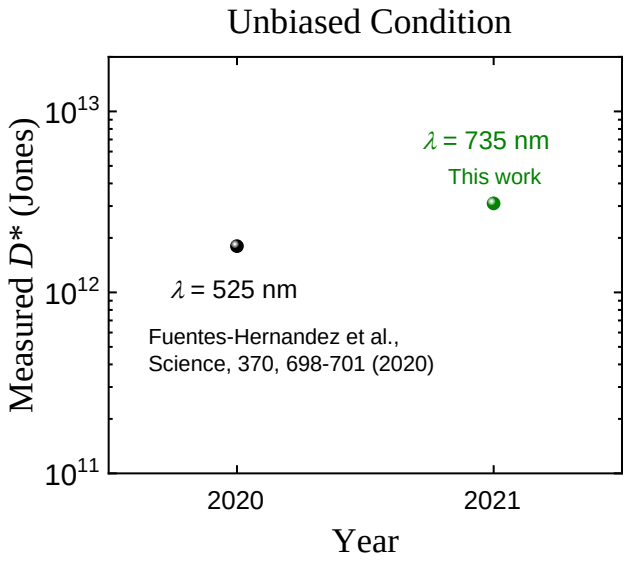

Figure 68. Measured D^* of P3HT:ICBA OPDs (median) consistent with [5] and PCE10:PC$_{71}$BM OPDs (best performing device) with PAL thickness of 700 nm (70 mg/mL in solution). Photoactive area is A = 0.1 cm^2. OPDs were measured at 0 V in air at B = 0, λ = 735 nm (LED source), and V = 0.

4.3 Approach 2: PCE10:$PC_{71}BM$-Based Organic Photodiodes (OPDs) with a Thin Photo-Active Layer (PAL) and ALD-based Passivation

The approach 1 has shown that the increment of the PAL thickness can reduce the RMS noise current (I_{rms}) values at the expense of the reduction of the responsivity ($\Re$). This feature enables the fabrication of narrowband OPDs. However, when broadband PCE10:$PC_{71}BM$ OPDs with high responsivity values are desired, a different approach is needed. As an alternative approach, the passivation of the interface between the PAL (PCE10:$PC_{71}BM$) and the HCE (MoO_x/Ag) is explored for OPDs with high responsivity and low RMS noise current values. In contrast to previous passivation approaches which use organic layers [38, 46], the proposed passivation in this research is done through the atomic layer deposition (ALD) of trimethylaluminum (TMA) and water (H_2O). OPDs with a thinner PAL of 170 nm are passivated. Performance of reference and passivated thin OPDs are compared in this section. The device structure is in is presented **Figure 69**.

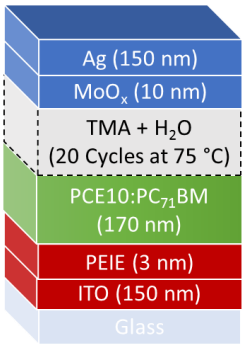

Figure 69. Device structure used in approach 2. The type of the PAL (PCE10:$PC_{71}BM$ with thickness of 170 nm) is a bulk heterojunction (BHJ) which can be exposed (passivated devices) or not (reference devices) to the atomic layer deposition (ALD) of TMA and H_2O precursors. ECE: ITO (150 nm) / PEIE (3 nm). HCE: MoO_x(10 nm)/Ag (150 nm).

4.3.1 J-V Curves under Dark Condition of Reference and Passivated Thin PCE10:$PC_{71}BM$ OPDs

The *J-V* curves under dark condition for reference and passivated PCE10:PC71BM OPDs (PAL thickness of 170 nm) are shown in **Figure 70 – Top** and **Figure 70 – Bottom**, respectively. As it can be observed, the passivation improves the shunt resistance of the *J-V* curves and increases the series resistance. By using the V_{OC}-J_{SC} curve (**Figure 71**) and the Prince model, the electrical parameters are obtained and summarized in **Table 12**.

The *J-V* curves generated by the Prince model with the electrical parameters in **Table 12** are shown in **Figure 72 – Top** and **Figure 72 – Bottom** for reference and passivated PCE10:$PC_{71}BM$ OPDs, respectively. From **Table 12**, the assumption in which the ideality factor n and reverse saturation current J_0 are the same for reference an passivated devices is used.

From **Table 12** the effect of the passivation on the series (R_S) and shunt (R_P) resistance values can be observed. The passivation improves the shunt resistance for at least one order of magnitude with respect references PCE10:$PC_{71}BM$ OPDs. All the obtained values of shunt resistance (R_P) for the passivated devices are higher than 1 GΩ. On the other hand, the series resistance values are increased as well in passivated devices. The increment is less than one order of magnitude with respect to reference devices. The highest value of the series resistance is R_S = 200 Ω.

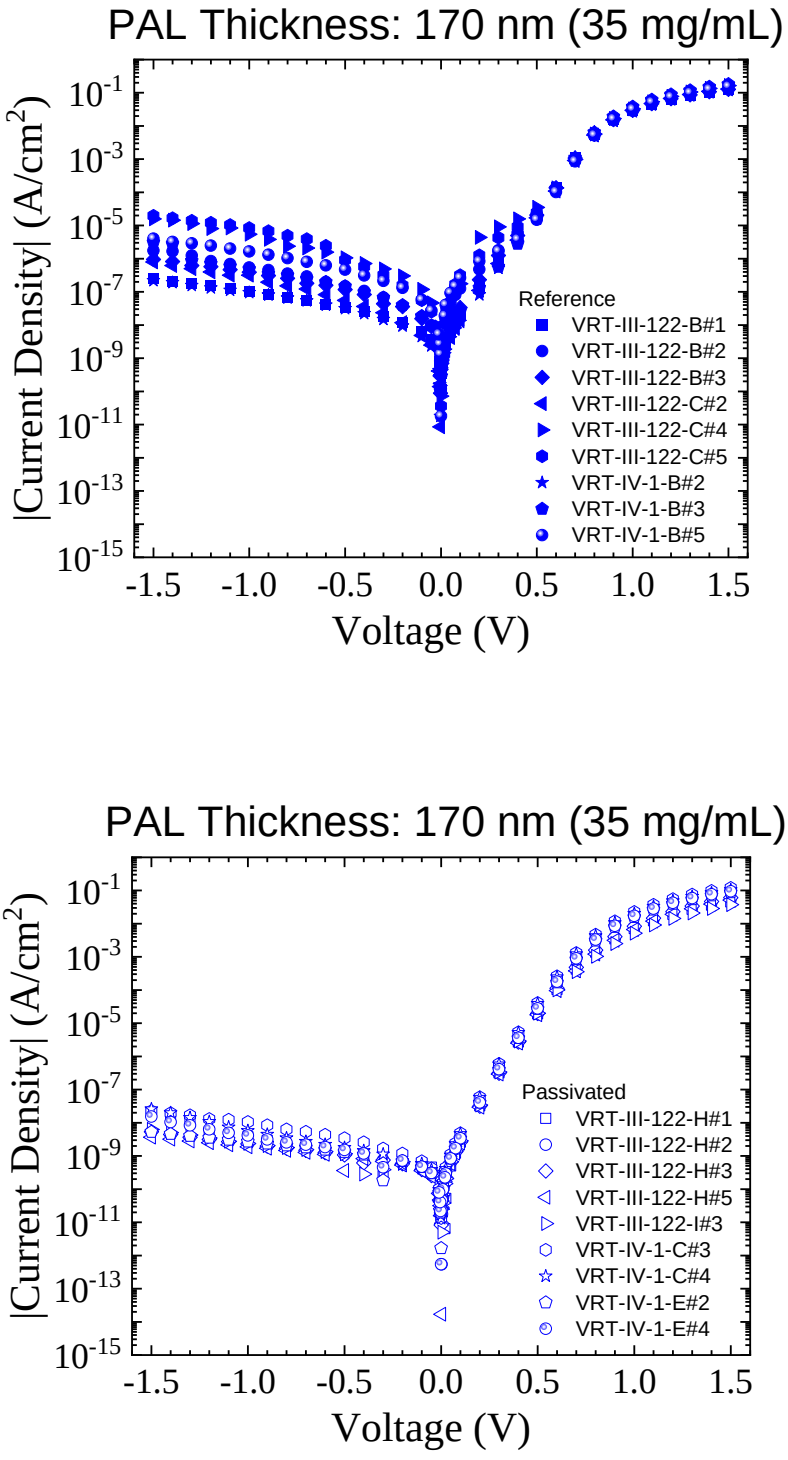

Figure 70. Measured *J-V* curves for PCE10:$PC_{71}BM$ NIR OPDs with relatively thin PAL thicknesses: 170 nm (35 mg/mL in solution). Top: Reference. Bottom: Passivated. Photoactive area is A = 0.1 cm^2. Measured in a N_2-filled GB.

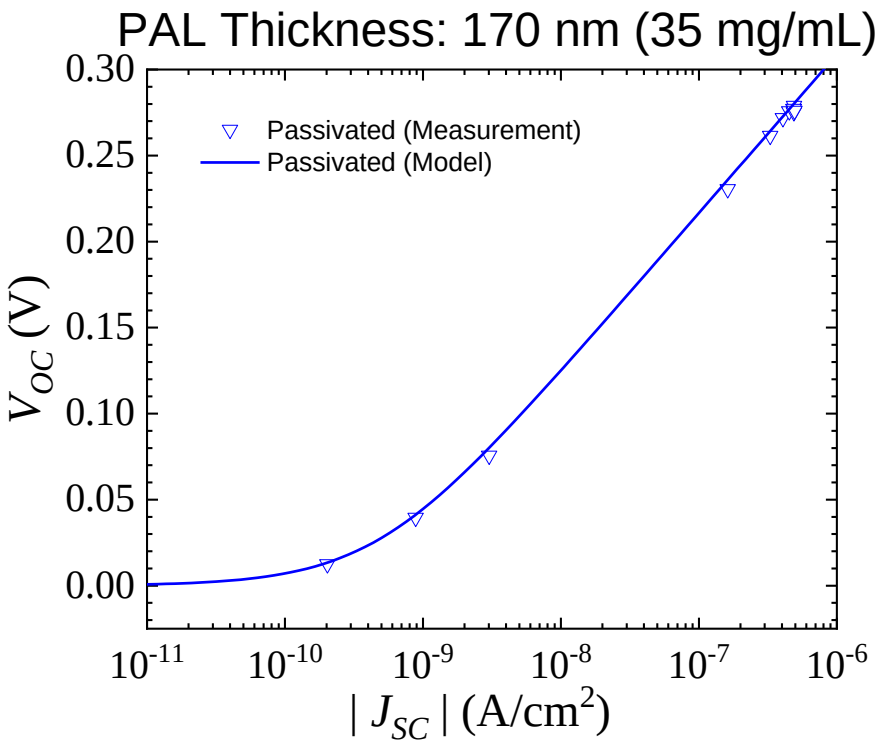

Figure 71. Measured V_{OC}-J_{SC} for a NIR light source (λ = 653 nm) for a PCE10:PC$_{71}$BM OPD with PAL thickness of 170 nm (35 mg/mL in solution). Photoactive area is A = 0.1 cm^2. Measured in a N$_2$-filled glovebox.

Table 12. Electrical parameters obtained from the Prince model [80] for PCE10:PC$_{71}$BM OPDs with thicknesses of 170 nm. Photoactive area is A = 0.1 cm^2.

Device	n	J_0 (pA/cm^2)	R_S (Ω)			R_P (Ω)		
			Min.	Med.	Max.	Min.	Med.	Max.
Reference	1.56	450	55	50	40	0.2 x 10^9	0.05 x 10^9	0.007 x 10^9
Passivated			200	100	60	6 x 10^9	5 x 10^9	2 x 10^9

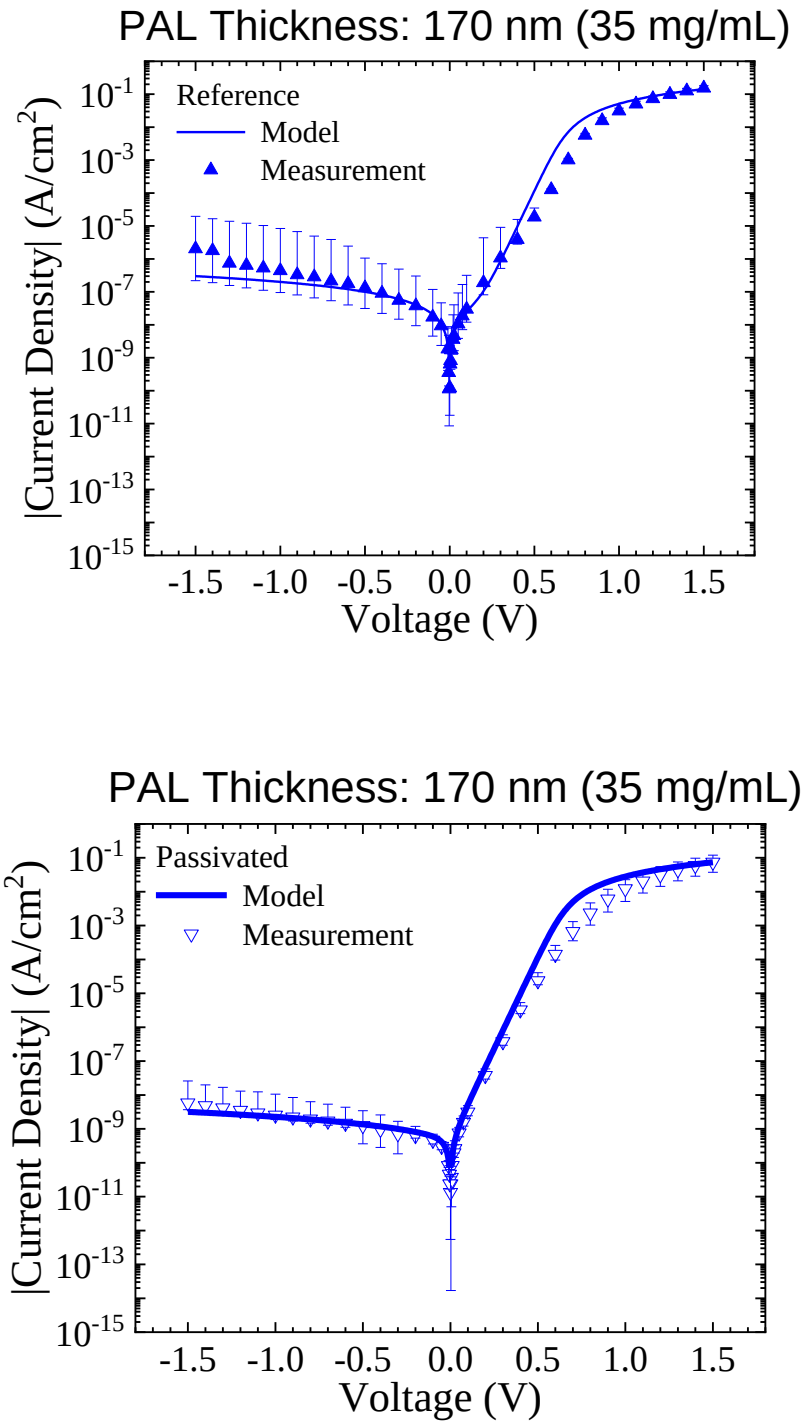

Figure 72. *J-V* curves (median of 7 devices) for PCE10:$PC_{71}BM$ OPDs (PAL thickness of 170 nm) and their respective simulated *J-V* curves with the Prince model. Top: Reference. Bottom: Passivated. Photoactive area is $A = 0.1$ cm^2. Measured in a N_2-filled glovebox.

Table 13. The ratio between the shunt resistance R_P and the series resistance R_S for reference and passivated PCE10:PC$_{71}$BM OPDs (PAL thicknesses of 170 nm).

Device	R_P / R_S		
	Minimum	Median	Maximum
Reference	4 x 10^6	1 x 10^6	0.2 x 10^6
Passivated	30 x 10^6	50 x 10^6	33 x 10^6

Table 13 evaluates the ratio of the shunt and series resistance values (R_P/R_S). The passivated devices show an improvement with respect to reference ones of almost one order of magnitude. The minimum ratio value of passivated devices is R_P/R_S = 30 x 10^6. This shows that despite the increment of R_S because of the passivation, the improvement of R_P is more significant.

4.3.2 Responsivity as a Function of Wavelength of Passivated PCE10:PC71BM NIR OPDs

The responsivity of passivated PCE10:PC$_{71}$BM OPDs at high optical power intensities (> 1 μW) for PAL thicknesses of 170 nm is evaluated for unbiased and biased conditions. Reference PCE10:PC$_{71}$BM OPDs will not be extensively characterized because of the lack of repeatability in their *J-V* curves under dark condition and their high noise as it will be show in the next sections. The optical source used is a LASER with a central wavelength value λ = 653 nm.

4.3.2.1 Responsivity at Optical Power under Unbiased Condition

The responsivity under unbiased conditions for passivated PCE10:$PC_{71}BM$ OPDs (located in different substrates) with PAL thicknesses of 170 nm are presented in **Figure 73**. The responsivity peak is 288 mA/W at λ = 700 nm and the calculated *EQE* value at this wavelength is 51%. At λ = 653 nm (testing LASER source), the responsivity value is 264 mA/W and the *EQE* value is 50%. At λ = 735 nm (testing LED source), the responsivity value is 240 mA/W and the *EQE* value is 40%.

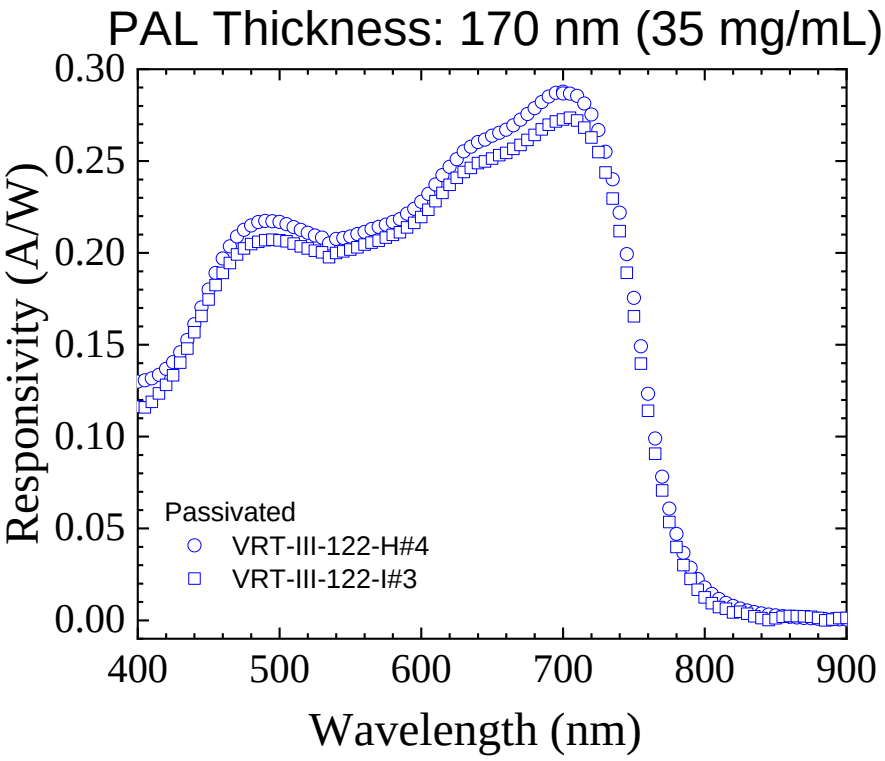

Figure 73. Measured responsivity of passivated PCE10:$PC_{71}BM$ OPDs with PAL thickness of 170 nm (35 mg/mL in solution). Photoactive area is A = 0.1 cm^2. OPDs were measured at 0 V in air.

4.3.2.2 Responsivity at Optical Power under Relevant Reverse Bias Conditions

Under biased conditions (V = -0.1 V, -0.5 V, -1 V), measurements of normalized (with respect to the responsivity values at the unbiased condition) responsivity values as a function of wavelength of passivated PCE10:$PC_{71}BM$ OPDs (PAL thicknesses of 170 nm) are presented in **Figure 74**. For the tested voltages, the increment in responsivity values do not reach the 30%. For an applied voltage V = -1.5 V the device has broken presumably due to the high electric field generated through the PAL combined with the previous stress during the *J-V* measurements, the photogenerated carriers and the exposure of the device to air.

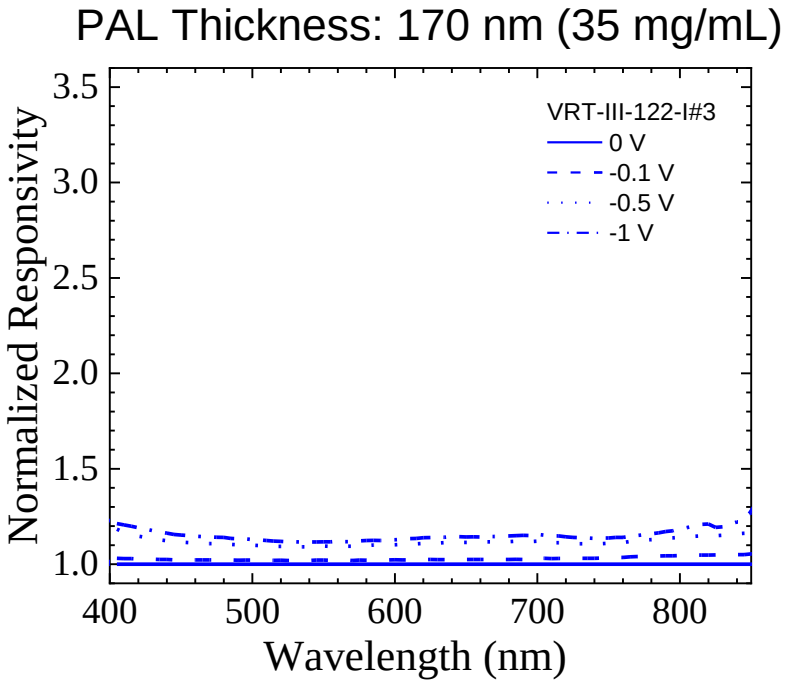

Figure 74. Measured normalized responsivity values (with respect to the unbiased condition) for different applied voltages of PCE10:$PC_{71}BM$ OPDs with PAL thickness of 170 nm. Photoactive area is A = 0.1 cm^2. OPDs were measured in air.

4.3.3 Noise Measurements on Thin PCE10:$PC_{71}BM$ OPDs

In this section, the measurements of RMS noise current values for reference and passivated PCE10:$PC_{71}BM$ OPDs (PAL thickness of 170 nm) are presented. Both unbiased and biased conditions are evaluated.

4.3.3.1 Noise Measurements under Unbiased Conditions – Thin Devices

As discussed earlier, the bandwidth B range should be first verified through the average current measurements (**Figure 75**). For reference OPDs, the average current ranges values between 2 pA and 70 pA; for passivated OPDs, the range is between 55 fA and 3 pA. Although this current should be ideally zero, experimental conditions can generate small currents (background illumination, thermal effects, etc.). Since the average current is lower than 100 pA for all the measurements, B = 1.5 Hz.

On the other hand, the RMS noise current values for reference and passivated PCE10:$PC_{71}BM$ OPDs are shown in **Figure 76**. For the reference OPDs, the RMS noise current I_{rms} values measured are between 40 fA and 430 fA (an outlier was observed at 930 fA) with a median value of 230 fA; for passivated OPDs, the RMS noise current I_{rms} values are between 20 fA and 50 fA (an outlier was observed at 280 fA) with a median value of 37 fA. Then the passivation reduces I_{rms} about 6 times with respect to reference devices.

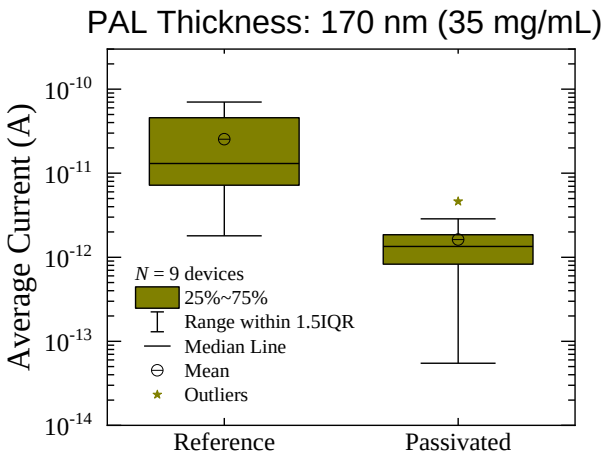

Figure 75. Measured average current under unbiased conditions of PCE10:$PC_{71}BM$ OPDs with PAL thickness of 170 nm. Closed and blue symbols on the left of the boxes represent the individual measurements of reference and passivated devices, respectively. Photoactive area is A = 0.1 cm^2. Nine OPDs for each condition were measured in a N_2-filled box.

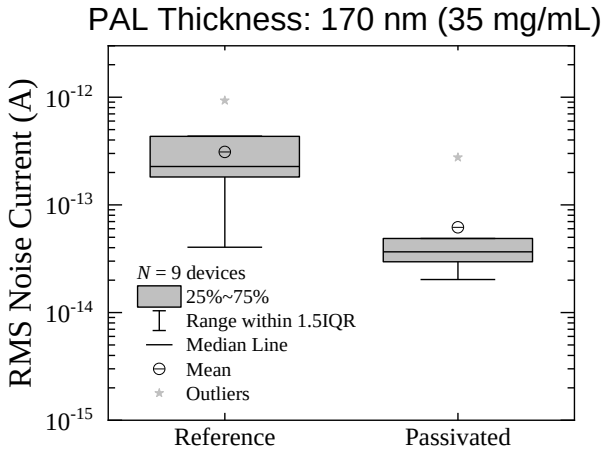

Figure 76. Measured RMS current under unbiased conditions of PCE10:$PC_{71}BM$ OPDs with PAL thickness of 170 nm. Closed and blue symbols on the left of the boxes represent the individual measurements of reference and passivated devices, respectively. Photoactive area is A = 0.1 cm^2. Nine OPDs for each condition were measured in a N_2-filled box.

Table 14. RMS noise current obtained from the Prince model [80] for approach 2. For the calculations: T = 25 °C. A: 0.1 cm^2.

Device	Shot RMS Noise Current $I_{rms,shot}$ (fA)	Thermal RMS Noise Current $I_{rms,thermal}$ (fA)			White RMS Noise Current $I_{rms,white}$ (fA)		
		Min.	Med.	Max.	Min.	Med.	Max.
Reference	7	11	22	59	13	23	60
Passivated		2	2	4	7	7	8

These measured RMS noise current I_{rms} values contrast with the RMS white noise current $I_{rms,white}$ values predicted by the Prince model (**Table 14).** It is assumed that both reference and passivated OPDs have the same calculated shot RMS noise current $I_{rms,shot}$ = 7 fA. Reference OPDs have a calculated $I_{rms,white}$ = 23 fA (median), suggesting that the calculated white noise is dominated by the thermal noise $I_{rms,thermal}$ = 22 fA (median). However, other sources of noise are present and show their dominant role as I_{rms} = 229 A, approximately. Passivated OPDs have a calculated $I_{rms,white}$ = 7 fA (median), suggesting that the calculated white noise is dominated by the shot noise of the same value. Nevertheless, in passivated OPDs, I_{rms} = 36 fA (median), and it is five times higher than its $I_{rms,white}$. This suggests that other sources of noise are also dominant.

Then, the passivation is expected not only to reduce effectively with respect to reference OPDs i) the calculated RMS thermal noise current $I_{rms,thermal}$ by one order of magnitude because of the the improvement of R_P, and ii) other sources of noise ($I_{rms,others}$), presumably Flicker noise, by six times approximately because of the potential reduction of defects at the PAL/HCE interface. Interfaces have been an optimization path for OPDs with low noise [38, 46].

4.3.3.2 Noise Measurements under Relevant Bias Conditions – Passivated Devices

Reference OPDs have shown a lower shunt resistance, higher RMS white noise current values, and higher measured RMS noise current values than passivated OPDs. Therefore, only passivated OPDs will be further characterized. Average and RMS noise currents under unbiased (0 V) and reverse bias conditions (-1.5 V, -1 V, -0.5 V, -0.1 V) are shown in **Figure 77** and **Figure 78**, respectively.

Measurements of the average current of passivated OPDs (**Figure 77**) determine that at the bias condition of -0.1 V, the measurement of the bandwidth is B = 1.5 Hz. When the bias condition is -0.5 V, -1.0 V and -1.5 V, the bandwidth is B = 11 Hz. For the bias condition of -0.5 V, most of the measurements will have associated a bandwidth of B = 11 Hz as the per the median of the measurements. These bandwidth values are important to explain potential differences in measurements of RMS noise currents and compare fairly RMS noise current values at different bias conditions. Some outliers for voltages at -0.5V, -1 V and -1.5 V are observed.

Measurements of the RMS current of passivated OPDs (**Figure 78**) show an increment of the RMS noise current (median value) from 37 fA at 0 V to 162 fA at -0.1 V The bandwidth for these measurements is B = 1.5 Hz. On the other hand, at -0.5 V, -1 V, and -1.5 V (the bandwidth is B = 11 Hz), the respective RMS noise current values are 0.8 pA, 3.6 pA, and 19 pA.

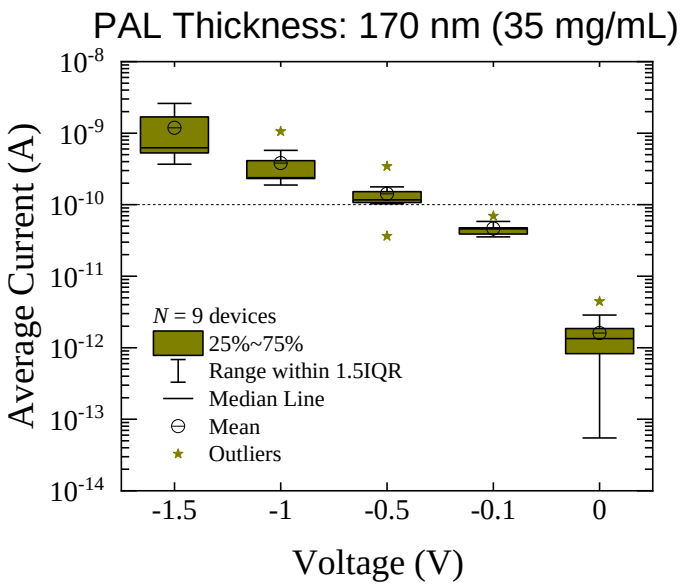

Figure 77. Measured average current values measured under unbiased and biased conditions of passivated PCE10:$PC_{71}BM$ OPDs with PAL thickness of 170 nm. Blue symbols on the left of the boxes represent the individual measurements. Photoactive area is A = 0.1 cm^2. Nine OPDs were measured in a N_2-filled box.

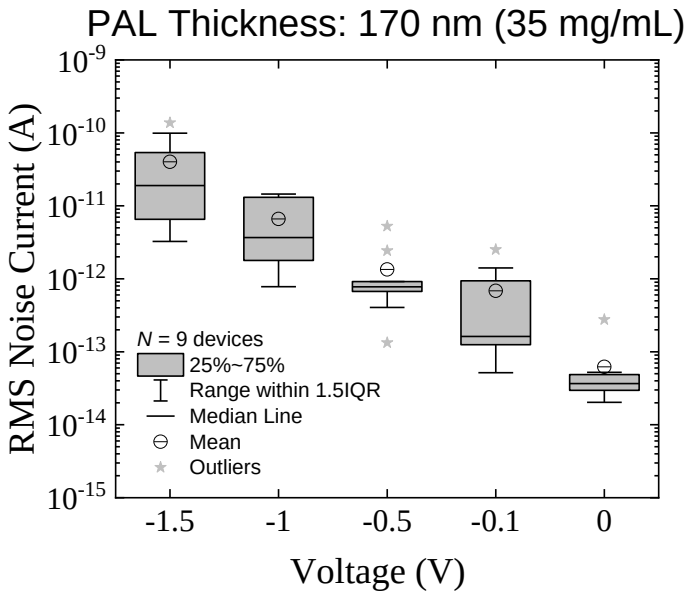

Figure 78. Measured RMS noise current values measured under unbiased and biased conditions of passivated PCE10:$PC_{71}BM$ OPDs with PAL thickness of 170 nm. Blue symbols on the left of the boxes represent the individual measurements. Photoactive area is A = 0.1 cm^2. Nine OPDs were measured in a N_2-filled box.

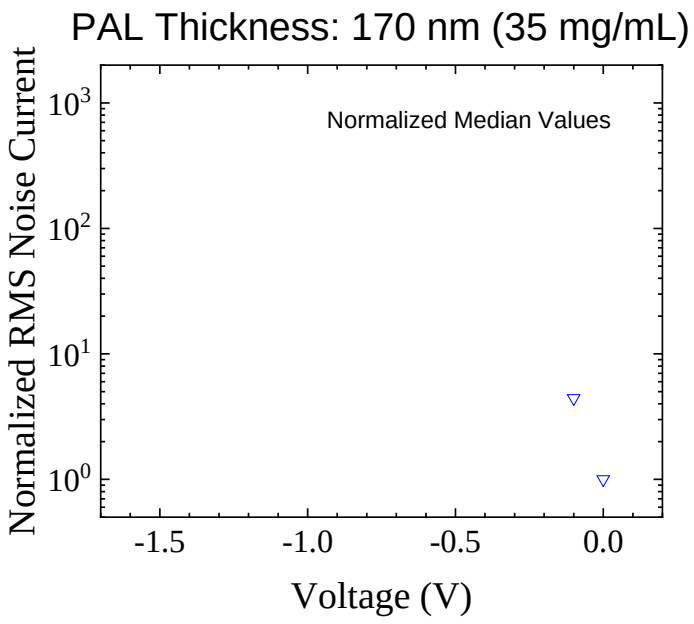

Figure 79. Measured normalized RMS noise current (median values) of PCE10:$PC_{71}BM$ OPDs with PAL thickness of 170 nm as a function of a reverse bias. Normalization is done with respect to the RMS noise current (median value) of the unbiased condition. Only devices with a bandwidth B = 1.5 Hz were considered. Photoactive area is A = 0.1 cm^2. OPDs were measured in a N_2-filled box.

For the bandwidth B = 1.5 Hz, the increment of the RMS noise current value is four times (**Figure 79**) at -0.1 V with respect to the unbiased condition (other reverse bias conditions have been omitted because they have a different bandwidth associated). The increment of the RMS noise current value is faster than the responsivity at high optical power intensities (>1 μW). Although the responsivity's dependence on light intensity might be different at low optical power intensities compared to high power intensities, this dependence can not only increase, but also decrease the responsivity value [5]. Therefore, to show the potential of the passivated PCE10:$PC_{71}BM$ OPDs, further characterization will be done at unbiased conditions only.

4.3.4 Light-Intensity Experiments on Passivated PCE10:$PC_{71}BM$ OPDs

The optical source used in this characterization is a LASER at a wavelength of λ = 653 nm. At this wavelength, the responsivity at high optical power intensities (>1 μW) of passivated PCE10:$PC_{71}BM$ OPDs with a PAL thickness of 170 nm is 254 mA/W. Then, the limits of detection at low optical power intensities for these devices will be assessed.

4.3.4.1 RMS Noise Current and Signal-to-Noise Ratio (SNR) as a Function of Light Intensity – Passivated OPDs

The RMS noise current under an unbiased condition is measured as a function of the illumination and shown in **Figure 80**. All the values are measured at a bandwidth B = 1.5 Hz. The RMS noise current value varies around 50 fA, which is in the same order of magnitude of the RMS noise current value obtained from 7 replicas with a median value of 37 fA under dark condition. A slightly increment trend of the RMS noise current values were observed within the evaluated optical power range (> 1 pW) in **Figure 80**.

As for the approach 1, the signal-to-noise ratio for the current ($SNR_{current}$) is obtained from the ratio between the measured photogenerated current (which is obtained after the subtraction of the dark current from the photocurrent), and the RMS noise current for each illumination condition. The results of these measurements are displayed in **Figure 81**.

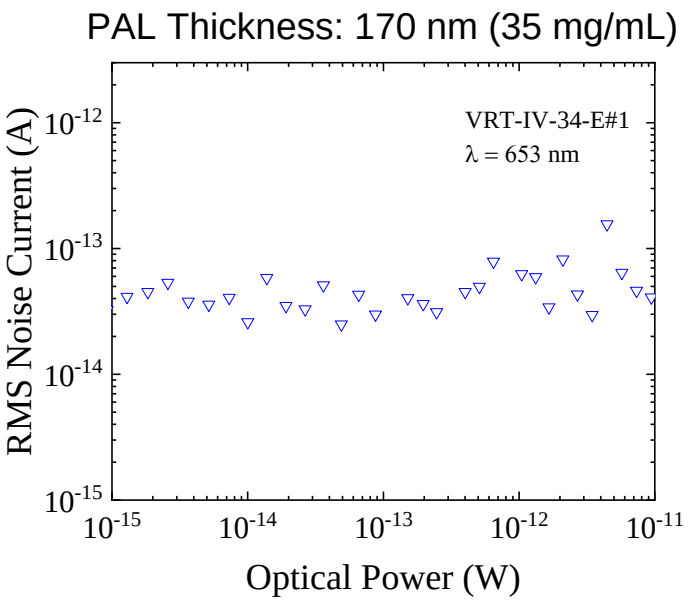

Figure 80. Measured RMS noise current as a function of optical power of a passivated PCE10:$PC_{71}BM$ OPD with a PAL thickness of 170 nm. Photoactive area is A = 0.1 cm^2. OPDs were measured in a N_2-filled box. External applied voltage V = 0.

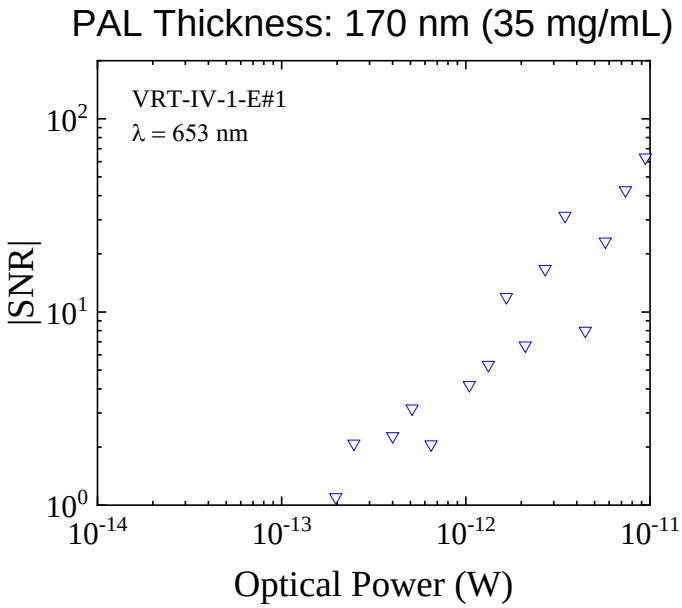

Figure 81. Measured SNR for different optical power values of a passivated PCE10:$PC_{71}BM$ OPD with PAL a thickness of 170 nm. Photoactive area is A = 0.1 cm^2. OPDs were measured in a N_2-filled box. External applied voltage V = 0.

4.3.4.2 Noise Equivalent Power (NEP) and Specific Detectivity (D*) – Passivated OPDs

An extrapolation of *SNR* as a function of the optical power to the condition in which *SNR* = 1 would indicate that the noise equivalent power (*NEP*) is *NEP* = 200 fW approximately. However, as discussed before, some statistics is required for a more appropriate characterization. Alternatively, the measured photogenerated current (see **Figure 82**) can be used along with the median RMS noise current value (obtained from different replicas of passivated devices under dark condition) to find the *NEP*. For this method, *NEP* = 197 fW and it is close to the value extracted from *SNR* curve with respect to the light intensity. This measured *NEP* value differs from the calculated ones typically reported in the literature under the assumption that the white noise is the dominant source of noise in the device and that the responsivity is constant for any light intensity. For example, under this assumption *NEP* would be 27 fA, nearly one order of magnitude lower than the value extracted from light intensity experiments. Even when RMS noise current values are measured and contain other sources of noise beyond white noise, an underestimation of the *NEP* values can take place when the dependence of the responsivity on the light intensity is not considered. In this scenario, for passivated PCE10:$PC_{71}BM$ OPDs, the calculated *NEP* is 142 fW. The different *NEP* values and their respective detectivity values *D** are summarized in **Table 15**.

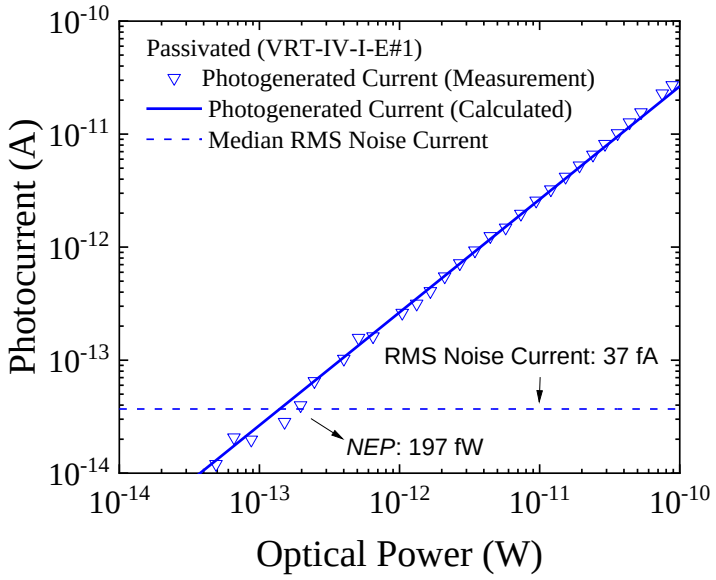

Figure 82. Measured and calculated photogenerated current as a function of optical power of a passivated PCE10:$PC_{71}BM$ OPD with a PAL thickness of 170 nm. Photoactive area is A = 0.1 cm^2. The OPD was measured in a N_2-filled box.

Table 15. Measured and calculated *NEP* and *D for a passivated PCE10:$PC_{71}BM$ OPD (PAL thickness of 170 nm) under unbiased conditions for λ = 653 nm. Photoactive area is A = 0.1 cm^2. Measurement bandwidth is B = 1.5 Hz.**

	Calculated Φ-Independent $\Re$ = 0.26 A/W	**Measured Φ-Dependent $\Re$ in Figure 82**
Calculated (median) $I_{rms,white}$ = 7 fA	D^* = 14.3 x 10^{12} cm $Hz^{0.5}$/W (*NEP* = 27 fW)	Measurement out of range
Measured (median) $I_{rms,white}$ = 37 fA	*NEP* = 142 fW D^* = 2.73 x 10^{12} cm $Hz^{0.5}$/W	*NEP* = 197 fW D^* = 1.97 x 10^{12} cm $Hz^{0.5}$/W

4.3.5 Summary of Results for Approach 2 and Benchmark with State-of-the-Art OPDs

The proposed passivation (approach 2) increased R_P (from MΩ to GΩ) and R_S (by tens of Ω) with respect to R_S, while preserved high ratios of $R_P/R_S > 10^6$. Calculated white noise ($I_{rms,white}$) in reference OPDs are dominated by thermal noise ($I_{rms,thermal}$ = 22 fA) and in passivated OPDs are dominated by shot noise ($I_{rms,shot}$ = 7 fA). On the other hand, measured noise (I_{rms}) is reduced from hundreds of fA in reference OPDs to tens of fA in passivated OPDs, suggesting that the noise is dominated by other noise sources (e.g., Flicker). Applied external voltages increased I_{rms} at a higher rate than $\mathfrak{R}$. When assumptions are made instead of direct measurements of noise and responsivity, D^* can be overestimated (up to seven times).

Figure 83 shows a comparison of the responsivity at high optical power values as a function of wavelength for the best passivated PCE10:PC_{71}BM OPD against the best P3HT:ICBA OPD consistent with [5]. It is noted that for wavelength values higher than 625 nm (up to 850 nm), the responsivity of the passivated PCE10:PC_{71}BM OPD is higher. Peak values are comparable in magnitude to the P3HT:ICBA OPD, but for PCE10:PC_{71}BM OPDs, this is located at the beginning of the NIR region (λ = 700 nm). PCE10:PC_{71}BM OPDs with organic interlayers as strategy to reduce noise and increase D^* between the PAL and HCE have been reported with $\mathfrak{R}(\lambda = 700\text{ nm}) = 0.15$ A/W [38], and comparable peak values at λ = 700 nm have reached at a reverse bias V = -0.5 V [46]. The superior responsivity of passivated PCE10:PC_{71}BM OPDs which is equal or higher that values reported in the literature is related to the fact that organic interlayers used to reduce the noise and improve R_P can absorb light without necessarily dissociate the exciton.

Under unbiased condition, the attained noise levels of PCE10:PC71BM OPDs under approach 1 are comparable to those P3HT:ICBA OPDs in the order of tens of fA [5]. Then D^* is measured through *NEP* (B = 1.5 Hz, A = 0.1 cm^2, λ = 653 nm, V = 0) and light intensity experiments obtaining comparable values in the order of 2 x 10^{12} Jones (best performing device) for the PAL thickness of 700 to P3HT:ICBA OPDs (median value) [5] (see **Figure 84**). Previously reported D^* values are either calculated or measured with a modulated light and/or and external bias [38], [46] (see **Table 3**), preventing a direct comparison, but giving an advantage to passivated PCE10:PC_{71}BM OPDs as its high values are measured under unbiased condition and using an optical source that is not modulated.

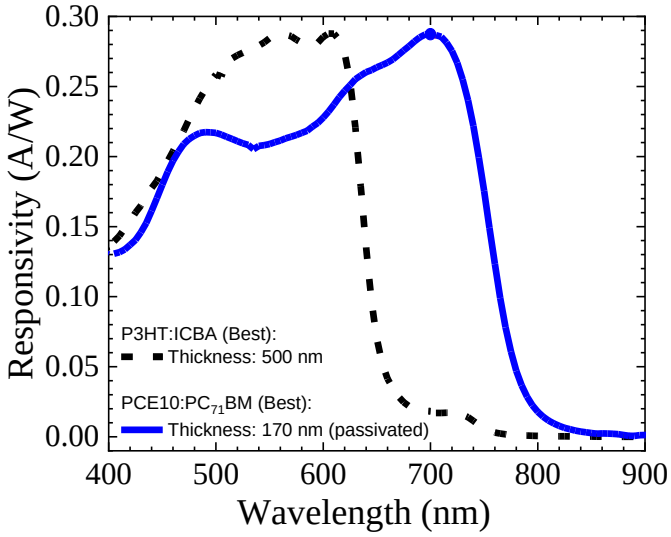

Figure 83. Measured and responsivity of a P3HT:ICBA OPD (best device) with PAL thickness of 500 nm consistent with [5] and a passivated PCE10:PC_{71}BM OPD (best device) with PAL thickness of 170 nm (35 mg/mL in solution). Photoactive area is A = 0.1 cm^2. OPDs were measured at 0 V in air.

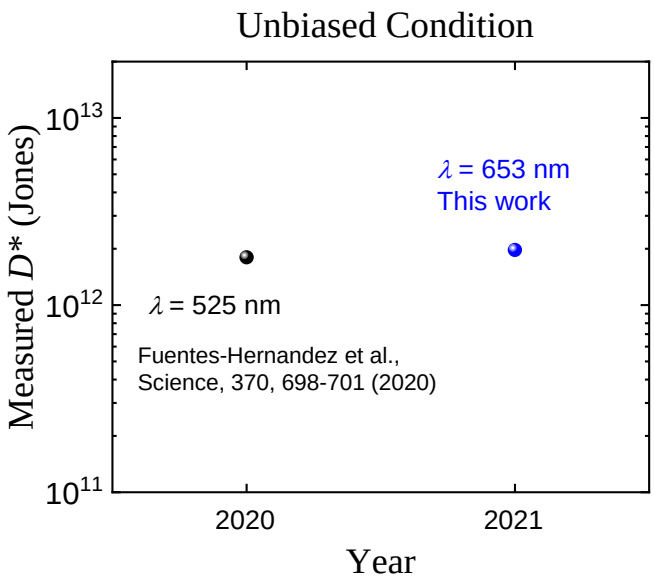

Figure 84. Measured *D of P3HT:ICBA OPDs (median) consistent with [5] and passivated PCE10:$PC_{71}BM$ OPDs (best performing device) with PAL thickness of 170 nm (35 mg/mL in solution). Photoactive area is A = 0.1 cm^2. OPDs were measured at 0 V in air at B = 0, λ = 653 nm (LASER source), and V = 0.**

CHAPTER 5. CONCLUSIONS AND FUTURE WORK

5.1 Summary of Key Findings

This dissertation provided a comprehensive characterization of OPDs with NIR sensitivity (based on the polymer PCE10 and the fullerene $PC_{71}BM$) through the direct measurement of the RMS noise current and by considering the responsivity's dependence on the light intensity.

Specific results and lessons learned:

1. The noise equivalent power (*NEP*) and the specific detectivity (*D**) were measured in PCE10:$PC_{71}BM$ OPDs with a thick PAL (approach 1 – PAL thicknesses of 700 nm and 1150 nm) and a thin passivated PAL (approach 2 – PAL thickness of 170 nm). Measured RMS noise current values in the order of the tens of fA under dark and unbiased conditions. Measured *NEP* values for both approaches are in the order of few hundreds of fW (< 200 fW), whereas *D** values varied between 2 x 10^{12} Jones and 3 x 10^{12} Jones. These values are contrasted to calculated ones under typical assumptions taken in the literature: 1) white noise as the only (or dominant) source of noise, and 2) constant value of the responsivity for any optical power. These assumptions can overestimate by nearly one order of magnitude the *NEP* and *D** values. The results of this dissertation suggest the need of a more accurate characterization of NIR OPDs by measuring the RMS noise current and considering the possible dependences of the responsivity on the light intensity.

2. Simulations presented in this dissertation have shown that photodiodes (photoactive area A = 1 cm^2) can operate as an optical sensor in short-circuit condition with high internal series resistance (R_S) values (e.g., R_S in the order of 100 Ω, 1 kΩ, and 1 MΩ) at relatively low light intensities (e.g., modeled through photogenerated current densities J_{ph} in the order of 100 pA/cm^2, 100 fA/cm^2). This high-series-resistance photodiode can efficiently transfer J_{ph} to the output in the form of short-circuit current density (J_{SC}), namely $J_{ph} \approx J_{SC}$, if the ratio between the shunt and the series resistance (R_P/R_S) values is high enough (e.g., $R_P/R_S \geq 10^3$). This contrasts with simulations of photodiodes (photoactive area A = 1 cm^2) operating as solar cells at high light intensities (e.g., J_{ph} = 100 mA/cm^2) [80] in which J_{SC} decreases drastically with R_S values around tens of ohms.

3. The flexibility in the photodiodes' series resistance R_S values allows the practical implementation of the proposed approaches in OPDs (photoactive area A = 0.1 cm^2). In addition to increase R_S, these approaches are also expected to increase the shunt resistance R_P value at a higher proportion because:
    a. In approach 1, the carriers must cross a thicker PAL (400 Ω ≤ R_S ≤ 40 kΩ), whereas the shunt paths are reduced ($0.5 \times 10^6 \leq R_P / R_S \leq 9 \times 10^6$).
    b. In approach 2, the passivation is done with materials whose electrical properties are insulating (60 Ω ≤ R_S ≤ 200 Ω), while presumably reducing defects and recombination at the organic/electrode interfaces ($30 \times 10^6 \leq R_P / R_S \leq 50 \times 10^6$).

4. While the electrical parameters derived from the Prince model and the measured *J-V* and V_{OC}-J_{SC} curves have guided the design of OPDs through the proposed approaches, the Prince model, as described and used in this dissertation, does not capture noise sources beyond the white noise. Other sources of noise, presumably Flicker noise, are dominant under the experimental conditions in which the PCE10:$PC_{71}BM$ OPDs were measured. Therefore, the reduction of RMS noise current values measured is explained not only by the reduction of the white noise, but also by the reduction of other sources of noise (e.g., Flicker noise). For the illumination conditions in which OPDs' *NEP* and *D** were measured, no significant changes were observed in the measured noise as a function of the illumination intensities.

5. The application of an external voltage yielded an increment in the responsivity values of both approaches, but also increased the RMS noise current values. The increase of the RMS noise current is significatively higher than that in responsivity. Therefore, only further characterization of OPDs (*NEP* and *D**) under unbiased conditions was done in which the RMS noise is the lowest.

5.2 Impact of the Findings

Two approaches were proposed to design and fabricate PCE10:$PC_{71}BM$ OPDs with NIR sensitivity. The RMS noise current values for PCE10:$PC_{71}BM$ OPDs in both approaches are comparable to state-of-the-art OPDs (based on the polymer P3HT and the fullerene ICBA), which only have sensitivity in the visible region (up to 650 nm) of the

electromagnetic spectrum [5]. The NIR sensitivity of PCE10:$PC_{71}BM$ OPDs can extend the current use P3HT:ICBA OPDs in sensing of faint light for optical sources beyond the visible range up to λ = 800 nm. The optical sensors with visible and NIR sensitivity proposed in this research can have an important impact on the biomedical fields, night vision, autonomous driving, etc. Furthermore, measured *D** values of PCE10:PC71BM OPDs under unbiased condition suggest their use in the context of self-powered sensors and the internet of things.

In addition to the NIR sensitivity, the proposed approaches for PCE10:$PC_{71}BM$ OPDs offer the possibility to have both narrowband (NIR only) and broadband (visible and NIR) sensitivity and similar levels of RMS noise current, *NEP*, and ultimately *D**. This might simplify the fabrication of photodetection platforms that require both spectral features because materials used in PAL, ECE, and HCE are the same. Narrowband PCE10:$PC_{71}BM$ OPDs (approach 1 - thick PAL) can be designed through the preparation of the PAL solution (i.e., concentration) or by modifying parameters in the deposition methods (e.g., speed of the spin coater, speed of the blade coater, etc.). Broadband PCE10:$PC_{71}BM$ OPDs (approach 2 – thin passivated PAL) are possible through the inclusion of the ALD method, which has been proven to be scalable and compatible with mass production of devices in other technologies (e.g. memories).

In contrast to optimized PH3HT:ICBA OPDs whose PAL require a thermal treatment at a temperature of 150 °C, processing of the PAL for PCE10:PC71BM OPDs require half of this temperature (i.e., 75 °C) reducing the energetic demand during the fabrication of the device. Furthermore, PCE10:PC71BM OPDs can be used to test other

optimization approaches to maximize D^* which do not require high temperatures (> 75 °C).

5.3 Suggestions for Future Work

Important remaining questions and potential future work:

1. The inclusion of non-fullerene acceptors of NFA (e.g., ITIC and its derivatives) have boosted the power conversion efficiencies (PCEs) of organic solar cells. These materials are characterized by its absorption in the NIR region of the electromagnetic spectrum and their photogeneration of carriers. A potential step in this research is to implement and evaluate the proposed approaches in NFA OPDs with NIR sensitivity.

2. Characterization methods that allow the identification of noise sources beyond white noise are desirable as a strategy to improve the performance of NIR OPDs and understand more clearly the effect of the proposed approach on those other sources of noise.

3. Approaches 1 and 2 have enabled not only to reduce the RMS noise current values, but also to increase the repeatability of the dark *J-V* curves in a logarithmic scale. This might have an important impact on the stability/reliability of the devices under different operation conditions (e.g., temperature, applied voltage, etc.).

4. As the proposed approaches attain comparable RMS noise current levels, the possibility of combining OPDs with different types of responsivity in form of arrays might create asymmetries that can be exploited for the detection of position of objects.

5. While it is expected that the response time of OPDs is lower than photodetection technologies with high crystallinity orders, the impact of the proposed approaches on the response time is of relevance when a specific application is targeted.

REFERENCES

[1] Hamamatsu, "Si Photodiodes," Model S1087/S1133 Series, 2014, https://www.hamamatsu.com/resources/pdf/ssd/s1087_etc_kspd1039e.pdf

[2] Hamamatsu, "Si photodiodes," Model S2386 Series, 2017, https://www.hamamatsu.com/resources/pdf/ssd/s2386_series_kspd1035e.pdf

[3] Hamamatsu, "Characteristics and Use of IR detectors," Model SD-12, 2011, https://mmrc.caltech.edu/FTIR/Literature/General/Hamamatus%20IR%20dectors.pdf

[4] F. P. G. de Arquer, A. Armin, P. Meredith, and E. H. Sargent, "Solution-processed semiconductors for next-generation photodetectors," *Nat. Rev. Mater.*, vol. 2, no. 3, p. 17, Mar. 2017.

[5] C. Fuentes-Hernandez, W. F. Chou, T. M. Khan, L. Diniz, J. Lukens, F. A. Larrain, V. A. Rodriguez-Toro, and B. Kippelen, "Large-area low-noise flexible organic photodiodes for detecting faint visible light," *Science*, vol. 370, no. 6517, pp. 698-701, Nov. 6, 2020.

[6] V. Coropceanu, X.-K. Chen, T. Wang, Z. Zheng, and J.-L. Brédas, "Charge-transfer electronic states in organic solar cells," *Nat. Rev. Mater.*, vol. 4, no. 11, pp. 689–707, Sep. 3, 2019.

[7] Isorg SA, Grenoble, France, http://www.isorg.fr/.

[8] Flexenable Limited, Cambridge, England, http://www.flexenable.com.

[9] NikkoIA SAS, Moirans, France, www.nikkoia.com.

[10] Orthogonal, Inc, Rochester, United States, https://orthogonalinc.com/.

[11] K. J. Baeg, M. Binda, D. Natali, M. Caironi, and Y. Y. Noh, "Organic light detectors: Photodiodes and phototransistors," *Adv. Mater.*, vol. 25, no. 31, pp. 4267-4295, Aug. 21, 2013.

[12] X. D. Liu, Y. W. Lin, Y. J. Liao, J. Z. Wu, and Y. H. Zheng, "Recent advances in organic near-infrared photodiodes," *J. Mater. Chem. C*, vol. 6, no. 14, pp. 3499-3513, Apr. 14, 2018.

[13] Q. Y. Li, Y. L. Guo, and Y. Q. Liu, "Exploration of near-infrared organic photodetectors," *Chem. Mater.*, vol. 31, no. 17, pp. 6359-6379, Sep. 10, 2019.

[14] Y. Yao, Y. Y. Liang, V. Shrotriya, S. Q. Xiao, L. P. Yu, and Y. Yang, "Plastic near-infrared photodetectors utilizing low band gap polymer," *Adv. Mater.*, vol. 19, no. 22, pp. 3979-3983, Nov. 19, 2007.

[15] E. Perzon, F. Zhang, M. Andersson, W. Mammo, O. Inganas, and M. R. Andersson, "A conjugated polymer for near infrared optoelectronic applications," *Adv. Mater.*, vol. 19, no. 20, pp. 3308-3311, Oct. 19, 2007.

[16] X. Gong, M. H. Tong, Y. J. Xia, W. Z. Cai, J. S. Moon, Y. Cao, G. Yu, C. L. Shieh, B. Nilsson, and A. J. Heeger, "High-detectivity polymer photodetectors with spectral response from 300 nm to 1450 nm," *Science*, vol. 325, no. 5948, pp. 1665-1667, Sep. 25, 2009.

[17] T. B. Yang, K. Sun, X. L. Liu, W. Wei, T. Z. Yu, X. Gong, D. L. Wang, and Y. Cao, "Zinc Oxide nanowire as an electron-extraction layer for broadband polymer photodetectors with an inverted device structure," *J. Phys. Chem. C*, vol. 116, no. 25, pp. 13650-13653, Jun. 28, 2012.

[18] E.-C. Chen, S.-R. Tseng, Y.-C. Chao, H.-F. Meng, C.-F. Wang, W.-C. Chen, C.-S. Hsu, and S.-F. Horng, "Polymer infrared photo-detector with high sensitivity up to 1100 nm," *Synth. Met.*, vol. 161, no. 15-16, pp. 1618-1622, Aug. 2011.

[19] G. Qian, J. Qi, and Z. Y. Wang, "Synthesis and study of low-bandgap polymers containing the diazapentalene and diketopyrrolopyrrole chromophores for potential use in solar cells and near-infrared photodetectors," *Journal of Materials Chemistry*, vol. 22, no. 25, pp. 12867-12873, Apr. 2012.

[20] X. Liu, H. Wang, T. Yang, W. Zhang, I. F. Hsieh, S. Z. D. Cheng, and X. Gong, "Solution-processed near-infrared polymer photodetectors with an inverted device structure," *Org. Electron.*, vol. 13, no. 12, pp. 2929-2934, Dec. 2012.

[21] X. Liu, J. Zhou, J. Zheng, M. L. Becker, and X. Gong, "Water-soluble CdTe quantum dots as an anode interlayer for solution-processed near infrared polymer photodetectors," *Nanoscale*, vol. 5, no. 24, pp. 12474-12479, Oct. 2013.

[22] F. Arca, M. Sramek, S. F. Tedde, P. Lugli, and O. Hayden, "Near-infrared organic photodiodes," *IEEE J. Quantum Electron.*, vol. 49, no. 12, pp. 1016-1025, Dec. 2013.

[23] E. Saracco, B. Bouthinon, J. M. Verilhac, C. Celle, N. Chevalier, D. Mariolle, O. Dhez, and J. P. Simonato, "Work function tuning for high-performance solution-processed organic photodetectors with inverted structure," *Adv. Mater.*, vol. 25, no. 45, pp. 6534-6538, Dec. 2013.

[24] X. W. Hu, K. Wang, C. Liu, T. Y. Meng, Y. Dong, S. J. Liu, F. Huang, X. Gong, and Y. Cao, "High-detectivity inverted near-infrared polymer photodetectors using cross-linkable conjugated polyfluorene as an electron extraction layer," *J. Mater. Chem. C*, vol. 2, no. 45, pp. 9592-9598, Sep. 2014.

[25] X. W. Hu, Y. Dong, F. Huang, X. Gong, and Y. Cao, "Solution-processed high-detectivity near-infrared polymer photodetectors fabricated by a novel low-bandgap semiconducting polymer," *J. Phys. Chem. C,* vol. 117, no. 13, pp. 6537-6543, Apr. 4, 2013.

[26] J. Qi, X. K. Zhou, D. Z. Yang, W. Q. Qiao, D. G. Ma, and Z. Y. Wang, "Optimization of solubility, film morphology and photodetector performance by molecular side-chain engineering of low-bandgap Thienothiadiazole-based polymers," *Adv. Funct. Mater.,* vol. 24, no. 48, pp. 7605-7612, Dec. 23, 2014.

[27] L. Z. Zhang, T. B. Yang, L. Shen, Y. J. Fang, L. Dang, N. J. Zhou, X. G. Guo, Z. R. Hong, Y. Yang, H. B. Wu, J. S. Huang, and Y. Y. Liang, "Toward highly sensitive polymer photodetectors by molecular engineering," *Adv. Mater.,* vol. 27, no. 41, pp. 6496-6503, Nov. 4, 2015.

[28] J. Qi, J. F. Han, X. K. Zhou, D. Z. Yang, J. D. Zhang, W. Q. Qiao, D. G. Ma, and Z. Y. Wang, "Optimization of broad-response and high-detectivity polymer photodetectors by bandgap engineering of weak donor-strong acceptor polymers," *Macromolecules,* vol. 48, no. 12, pp. 3941-3948, Jun. 23, 2015.

[29] W. B. Wang, F. J. Zhang, L. L. Li, M. Zhang, Q. S. An, J. Wang, and Q. Q. Sun, "Highly sensitive polymer photodetectors with a broad spectral response range from UV light to the near infrared region," *J. Mater. Chem. C,* vol. 3, no. 28, pp. 7386-7393, June 2015.

[30] L. Shen, Y. Zhang, Y. Bai, X. Zheng, Q. Wang, and J. Huang, "A filterless, visible-blind, narrow-band, and near-infrared photodetector with a gain," *Nanoscale,* vol. 8, no. 26, pp. 12990-12997, May 2016.

[31] S. P. Wu, B. A. Xiao, B. F. Zhao, Z. C. He, H. B. Wu, and Y. Cao, "High sensitivity polymer visible-near infrared photodetectors via an inverted device structure and manipulation of injection barrier height," *Small,* vol. 12, no. 25, pp. 3374-3380, Jul. 6, 2016.

[32] Z. H. Wu, W. C. Yao, A. E. London, J. D. Azoulay, and T. N. Ng, "Temperature-dependent detectivity of near-infrared organic bulk heterojunction photodiodes," *ACS Appl. Mater. Inter.,* vol. 9, no. 2, pp. 1654-1660, Jan. 18, 2017.

[33] S. X. Xiong, J. H. Tong, L. Mao, Z. F. Li, F. Qin, F. Y. Jiang, W. Meng, T. F. Liu, W. W. Li, and Y. H. Zhou, "Double-side responsive polymer near-infrared photodetectors with transfer-printed electrode," *J. Mater. Chem. C,* vol. 4, no. 7, pp. 1414-1419, Jan. 2016.

[34] J. Han, J. Qi, X. Zheng, Y. Wang, L. Hu, C. Guo, Y. Wang, Y. Li, D. Ma, W. Qiao, and Z. Y. Wang, "Low-bandgap donor-acceptor polymers for photodetectors with photoresponsivity from 300 nm to 1600 nm," *J. Mater. Chem. C,* vol. 5, no. 1, pp. 159-165, Jan. 7, 2017.

[35] R. M. Nie, X. Y. Deng, L. Feng, G. G. Hu, Y. Y. Wang, G. Yu, and J. B. Xu, "Highly sensitive and broadband organic photodetectors with fast speed gain and large linear dynamic range at low forward bias," *Small,* vol. 13, no. 24, pp. 1603260-1--1603260-10, June 27, 2017.

[36] A. E. London, L. F. Huang, B. A. Zhang, M. B. Oviedo, J. Tropp, W. C. Yao, Z. H. Wu, B. M. Wong, T. N. Ng, and J. D. Azoulay, "Donor-acceptor polymers with tunable infrared photoresponse," *Polym. Chem.,* vol. 8, no. 19, pp. 2922-2930, May 2017.

[37] M. L. Gao, W. B. Wang, L. L. Li, J. L. Miao, and F. J. Zhang, "Highly sensitive polymer photodetectors with a wide spectral response range," *Chinese Phys. B,* vol. 26, no. 1, pp. 018201-1--018201-7, Jan. 2017.

[38] S. X. Xiong, L. L. Li, F. Qn, L. Mao, B. W. Luo, Y. Y. Jiang, Z. F. Li, J. S. Huang, and Y. H. Zhou, "Universal strategy to reduce noise current for sensitive organic photodetectors," *ACS Appl. Mater. Inter.,* vol. 9, no. 10, pp. 9176-9183, Mar. 15, 2017.

[39] L. Y. Zheng, T. Zhu, W. Z. Xu, L. Liu, J. Zheng, X. Gong, and F. Wudl, "Solution-processed broadband polymer photodetectors with a spectral response of up to 2.5 um by a low bandgap donor-acceptor conjugated copolymer," *J. Mater. Chem. C,* vol. 6, no. 14, pp. 3634-3641, Apr. 14, 2018.

[40] F. Verstraeten, S. Gielen, P. Verstappen, J. Kesters, E. Georgitzikis, J. Raymakers, D. Cheyns, P. Malinowski, M. Daenen, L. Lutsen, K. Vandewal, and W. Maes, "Near-infrared organic photodetectors based on bay-annulated indigo showing broadband absorption and high detectivities up to 1.1 mu m," *J. Mater. Chem. C,* vol. 6, no. 43, pp. 11645-11650, Nov. 21, 2018.

[41] J. Han, D. Yang, D. Ma, W. Qiao, and Z. Y. Wang, "Low-bandgap polymers for high-performance photodiodes with maximal EQE near 1200 nm and broad spectral response from 300 to 1700 nm," *Adv. Opt. Mater.,* vol. 6, no. 15, pp. 1800038-1--1800038-7, Aug. 6, 2018.

[42] S. Park, K. Fukuda, M. Wang, C. Lee, T. Yokota, H. Jin, H. Jinno, H. Kimura, P. Zalar, N. Matsuhisa, S. Umezu, G. C. Bazan, and T. Someya, "Ultraflexible near-infrared organic photodetectors for conformal photoplethysmogram sensors," *Adv. Mater.,* vol. 30, no. 34, pp. 1802359-1--1802359-8, Aug. 23, 2018.

[43] Z. Wu, W. Yao, A. E. London, J. D. Azoulay, and T. N. Ng, "Elucidating the detectivity limits in shortwave infrared organic photodiodes," *Adv. Funct. Mater.,* vol. 28, no. 18, pp. 1800391-1--1800391-9, May 4, 2018.

[44] C. M. Benavides, S. Rechberger, E. Spiecker, M. Berlinghof, T. Unruh, M. Biele, O. Schmidt, C. J. Brabec, and S. F. Tedde, "Improving spray coated organic photodetectors performance by using 1,8-diiodooctane as processing additive," *Org. Electron.,* vol. 54, pp. 21-26, Mar. 2018.

[45] J. L. Miao, F. J. Zhang, M. D. Du, W. B. Wang, and Y. Fang, "Photomultiplication type organic photodetectors with broadband and narrowband response ability," *Adv. Opt. Mater.*, vol. 6, no. 8, pp. 1800001-1--1800001-7, Apr. 19, 2018.

[46] H. Kim, B. Song, K. Lee, J. Kim, and J. Kanicki, "High-performance PBT7-Th:PC70BM polymer photodiode with transferred charge blocking layers," *Org. Electron.*, vol. 62, pp. 566-571, Nov. 2018.

[47] W. Yao, Z. Wu, E. Huang, L. Huang, A. E. London, Z. Liu, J. D. Azoulay, and T. N. Ng, "Organic bulk heterojunction infrared photodiodes for imaging out to 1300 nm," *ACS Appl. Electron. Mater.*, vol. 1, no. 5, pp. 660-666, May 28, 2019.

[48] Z. M. Y. Zeng, Z. M. Zhong, W. K. Zhong, J. X. Zhang, L. Ying, G. Yu, F. Huang, and Y. Cao, "High-detectivity organic photodetectors based on a thick-film photoactive layer using a conjugated polymer containing a naphtho 1,2-c:5,6-c bis 1,2,5 thiadiazole unit," *J. Mater. Chem. C*, vol. 7, no. 20, pp. 6070-6076, May 2019.

[49] G. Pace, A. Grimoldi, Z. Rengert, G. C. Bazan, D. Natali, and M. Caironi, "Inkjet printed organic detectors with flat responsivity up to the NIR and inherent UV optical filtering," *Synth. Met.*, vol. 254, pp. 92-96, Aug. 2019.

[50] T. Hamid, S. D. Yambem, and A. K. Pandey, "Photodetection efficiency enhancement of IR sensitive organic photodetectors via triplet energy transfer," *Synth. Met.*, vol. 256, pp. 116117-1--116117-6, Oct. 2019.

[51] Z. Wu, N. Li, N. Eedugurala, J. D. Azoulay, D.-S. Leem, and T. N. Ng, "Noise and detectivity limits in organic shortwave infrared photodiodes with low disorder," *npj Flexible Electronics*, vol. 4, no. 1, pp. 1-6, Apr. 2020.

[52] Y. J. Fang, A. Armin, P. Meredith, and J. S. Huang, "Accurate characterization of next-generation thin-film photodetectors," *Nat. Photonics*, vol. 13, no. 1, pp. 1-4, Jan. 2019.

[53] Ossila Ltd, Sheffield, United Kingdom, www.ossila.com.

[54] 1-Material Inc., Dorval, Canada, www.1-material.com.

[55] Alfa Aesar (Thermo Fisher Scientific Chemicals, Inc.), M. Tewksbury, United States, www.alfa.com.

[56] Luminescence Technology Corp. , N. T. City, Taiwan, www.lumtec.com.tw.

[57] Sigma-Aldrich Corporation, M. St. Louis, United States, www.sigmaaldrich.com.

[58] Solarmer Energy, Inc. , C. El Monte, United States, www.solarmer.com.

[59] P. Cheng, G. Li, X. W. Zhan, and Y. Yang, "Next-generation organic photovoltaics based on non-fullerene acceptors," *Nat. Photonics,* vol. 12, no. 3, pp. 131-142, Mar 2018.

[60] L. Ye, S. Q. Zhang, W. C. Zhao, H. F. Yao, and J. H. Hou, "Highly Efficient 2D-Conjugated Benzodithiophene-Based Photovoltaic Polymer with Linear Alkylthio Side Chain," *Chem. Mater.,* vol. 26, no. 12, pp. 3603-3605, Jun 2014.

[61] S. H. Liao, H. J. Jhuo, Y. S. Cheng, and S. A. Chen, "Fullerene derivative-doped Zinc Oxide nanofilm as the cathode of inverted polymer solar cells with low-bandgap polymer (PTB7-Th) for high performance," *Adv. Mater.,* vol. 25, no. 34, pp. 4766-4771, Sep. 14, 2013.

[62] S. Q. Zhang, L. Ye, W. C. Zhao, D. L. Liu, H. F. Yao, and J. H. Hou, "Side Chain Selection for Designing Highly Efficient Photovoltaic Polymers with 2D-Conjugated Structure," *Macromolecules,* vol. 47, no. 14, pp. 4653-4659, Jul 2014.

[63] Z. C. He, B. Xiao, F. Liu, H. B. Wu, Y. L. Yang, S. Xiao, C. Wang, T. P. Russell, and Y. Cao, "Single-junction polymer solar cells with high efficiency and photovoltage," *Nat. Photonics,* vol. 9, no. 3, pp. 174-179, Mar 2015.

[64] Q. Wan, X. Guo, Z. Y. Wang, W. B. Li, B. Guo, W. Ma, M. J. Zhang, and Y. F. Li, "10.8% Efficiency Polymer Solar Cells Based on PTB7-Th and PC71BM via Binary Solvent Additives Treatment," *Adv. Funct. Mater.,* vol. 26, no. 36, pp. 6635-6640, Sep 2016.

[65] L. K. Jagadamma, M. T. Sajjad, V. Savikhin, M. F. Toney, and I. D. W. Samuel, "Correlating photovoltaic properties of a PTB7-Th:PC71BM blend to photophysics and microstructure as a function of thermal annealing," *J. Mater. Chem. A,* vol. 5, no. 28, pp. 14646-14657, Jul. 28, 2017.

[66] C. Fuentes-Hernandez, "Charge transport and photogeneration in organic semiconductors: Photorefractives and beyond," in *Photorefractive Organic Materials and Applications*, vol. 240, P. A. Blanche, Ed. (Springer Series in Materials Science, Cham: Springer Int Publishing Ag, 2016, pp. 65-127.

[67] J. L. Bredas, "Mind the gap!," *Mater. Horiz.,* vol. 1, no. 1, pp. 17-19, Jan. 2014.

[68] I. N. Levine, D. H. Busch, and H. Shull, *Quantum chemistry*. Pearson Prentice Hall Upper Saddle River, NJ, 2009.

[69] M. Fahlman, S. Fabiano, V. Gueskine, D. Simon, M. Berggren, and X. Crispin, "Interfaces in organic electronics," *Nat. Rev. Mater.,* vol. 4, no. 10, pp. 627–650, July 25, 2019.

[70] K. Akaike, M. Oehzelt, G. Heimel, and N. Koch, "A comprehensive and unified picture of energy-level alignment at interfaces with organic semiconductors," in *Organic Light Emitting Materials and Devices XX*, 2016, vol. 9941.

[71] C. Fuentes-Hernandez, W. Chou, V. Rodriguez-Toro, F. Larrain, and B. Kippelen, "On the characterization and modeling of the current characteristics of organic photodiodes," in *2019 IEEE Research and Applications of Photonics in Defense Conference (RAPID)*, 2019, pp. 1-3.

[72] R. D. Jansen-van Vuuren, A. Armin, A. K. Pandey, P. L. Burn, and P. Meredith, "Organic photodiodes: The future of full color detection and image sensing," *Adv. Mater.*, vol. 28, no. 24, pp. 4766-4802, Apr. 25, 2016.

[73] A. De Sanctis, G. F. Jones, D. J. Wehenkel, F. Bezares, F. H. L. Koppens, M. F. Craciun, and S. Russo, "Extraordinary linear dynamic range in laser-defined functionalized graphene photodetectors," *Sci. Adv.*, vol. 3, no. 5, pp. e1602617-1--e1602617-8, May 26, 2017.

[74] J. C. Zhou and J. Huang, "Photodetectors based on organic-inorganic hybrid Lead halide perovskites," *Adv. Sci.*, vol. 5, no. 1, pp. 1700256-1--1700256-24, Jan. 2018.

[75] H. Wang and D. H. Kim, "Perovskite-based photodetectors: Materials and devices," *Chem. Soc. Rev.*, vol. 46, no. 17, pp. 5204-5236, Sep. 7, 2017.

[76] S. L. Chuang, *Physics of Optoelectronic Devices*. New York: Wiley Series in Pure and Applied Optics, 1995.

[77] G. Keiser, *Optical Fiber Communications*. New York: Wiley Encyclopedia of Telecommunications, 2003.

[78] P. Bhattacharya, *Semiconductor Optoelectronic Devices*. Upper Saddle River, NJ: Prentice Hall, 1997.

[79] B. Kippelen and J. L. Bredas, "Organic photovoltaics," *Energy Environ. Sci.*, vol. 2, no. 3, pp. 251-261, Jan. 2009.

[80] M. B. Prince, "Silicon solar energy converters," *J. Appl. Phys.*, vol. 26, no. 5, pp. 534-540, 1955.

[81] W. Shockley, "The theory of p-n junction in semiconductors and p-n junction transistors," *Bcl] Syst. Tech. J.*, vol. 28, no. 3, pp. 435-489, 1949.

[82] M. J. Buckingham, *Noise in Electronic Devices and Systems*. Amsterdam. The Netherlands: Ellis Horwood Pub, 1983.

[83] C. D. Motchenbacher and J. A. Connelly, *Low-Noise Electronic System Design*. New York: Wiley, 1993.

[84] H. W. Ott, *Noise Reduction Techniques in Electronic Systems*. New York: Wiley, 1988.

[85] T. Grasser, *Noise in Nanoscale Semiconductor Devices*. Cham, Switzerland: Springer, 2020.

[86] J. A. Woollam, "Spectroscopic Ellipsometer," Model M-2000, 2010, https://www.jawoollam.com/products/m-2000-ellipsometer

[87] T. Vo-Van and N. Le-quang, "Ellipsometry as a characterization technique," in *Materials Characterization and Optical Probe Techniques: A Critical Review*, , USA, 1997, vol. 10291, pp. 398-422: SPIE.

[88] J. A. Woollam, B. D. Johs, C. M. Herzinger, J. N. Hilfiker, R. A. Synowicki, and C. L. Bungay, "Overview of variable-angle spectroscopic ellipsometry (VASE): I. Basic theory and typical applications," in *Optical Metrology: A Critical Review, 18-23 July 1999*, USA, 2017, vol. 10294, p. 1029402 (26 pp.): SPIE.

[89] B. Johs, J. A. Woollam, C. M. Herzinger, J. N. Hilfiker, R. A. Synowicki, and C. L. Bungay, "Overview of variable-angle spectroscopic ellipsometry (VASE): II. Advanced applications," in *Optical Metrology: A Critical Review, 18-23 July 1999*, USA, 2017, vol. 10294, p. 1029404 (30 pp.): SPIE.

[90] Veeco, "Veeco Dektak 6M Profilometer," Model Detktak 150, 2004, https://ir.veeco.com/

[91] M. Conroy and J. Armstrong, "A comparison of surface metrology techniques," in *Conference on Optical Micro- and Nanometrology in Microsystems Technology*, Strasbourg, FRANCE, 2006, vol. 6188, BELLINGHAM: Spie-Int Soc Optical Engineering, 2006.

[92] M. Conroy and J. Armstrong, "A comparison of surface metrology techniques," in *7th International Symposium on Measurement Technology and Intelligent Instruments*, Bristol, 2005, vol. 13, pp. 458-465: Iop Publishing Ltd.

[93] Besocke Delta Phi, "Instruction Manual," Model Kelvin Probe S / Kelvin Probe S compact and Kelvin Control 07, http://www.besocke-delta-phi.de/index.htm

[94] SPI Supplies, W. Chester, United States, 2spi.com.

[95] Branson, "Ultrasonic Cleaners," Model 1510, 2007, https://www.emerson.com/en-us

[96] Laurell, "Standard Operating Procedure," Model WS-400B-6NPP-Lite, 2007, http://www.laurell.com/

[97] VWR International, LLC, Radnor, United States, www.vwr.com.

[98] Mse Supplies, LLC, Tucson, United States https://www.msesupplies.com/.

[99] Y. Zhou, C. Fuentes-Hernandez, J. Shim, J. Meyer, A. J. Giordano, H. Li, P. Winget, T. Papadopoulos, H. Cheun, J. Kim, M. Fenoll, A. Dindar, W. Haske, E. Najafabadi, T. M. Khan, H. Sojoudi, S. Barlow, S. Graham, J.-L. Brédas, S. R. Marder, A. Kahn, and B. Kippelen, "A universal method to produce low–work function electrodes for organic electronics," *Science*, vol. 336, no. 6079, pp. 327-332, Apr. 20, 2012.

[100] Headway Research Inc, Dallas, United States, https://www.headwayresearch.com/.

[101] Solenne B.V. , Groningen, Netherlands, www.solennebv.com.

[102] Veeco Instruments Inc. / Ultratech, Inc. / CambridgeNanotechALD, Plainview, United States, https://www.veeco.com/.

[103] Kurt J Lesker Co Vacuum, Pittsburgh, United States, www.lesker.com.

[104] Kurt J Lasker, "Arizona University Spectros Deposition System," Model TUR033, 2002, www.lesker.com

[105] Mbraun Inc, Boston, United States, mbraun.com.

[106] National Instruments Corp, Austin, United States, www.ni.com.

[107] Hamamatsu Photonics K.K., Hamamatsu, Japan, www.hamamatsu.com.

[108] Keithley, "Sub-Femtoamp Remote SourceMeter," Model 6430, 2008, https://www.tek.com/specialty-instruments/keithley-high-resistance-low-current-electrom-manual/6430-901-01

[109] Keysight Technologies, "The Parametric Measurement Handbook," Model Parametric Measurement Instruments, 2020, https://www.keysight.com/us/en/assets/7018-05884/application-notes/5992-2508.pdf

[110] Energetiq, "LDLS™ Laser-Driven Light Source. Operation and Maintenance Manual," Model EQ-99X, 2015, https://mountainphotonics.de/wp-content/uploads/2018/12/EQ99X_rev2_manual.pdf

[111] CVI Spectral Products - Digikrom, "CM 110 1/8m monochromator," Model CM110, 2006, https://www.spectralproducts.com/CM110/1812

[112] Newport Corp, Irvine, USA, mksinst.com.

[113] Keithley, "User's Manual," Model 6517A, 1998, https://www.tek.com/manual/model-6517a-electrometer-high-resistance-meter-getting-started-manual-rev-b

[114] Keithley, "User's Manual," Model 2400, 1998, https://www.tek.com/keithley-source-measure-units/keithley-smu-2400-standard-series-sourcemeter

[115] Ophir Photonics - Newport, "Laser Power/Energy Meter - User Manual," Model NOVA II, 2011, www.ophiropt.com/photonics

[116] THORLABS, Model M735L3, 2015, https://www.thorlabs.com/thorproduct.cfm?partnumber=M375L3

[117] Agilent Technologies, "Dual Output DC Power Supplies - User's and Service Guide," Model E364xA, 2013, https://www.agilent.com/

[118] J. D. Servaites, S. Yeganeh, T. J. Marks, and M. A. Ratner, "Efficiency Enhancement in Organic Photovoltaic Cells: Consequences of Optimizing Series Resistance," *Adv. Funct. Mater.*, vol. 20, no. 1, pp. 97-104, Jan 2010.

[119] C. W. Tang, "Two-layer organic photovoltaic cell," *Appl. Phys. Lett.*, vol. 48, no. 2, pp. 183-5, 01/13 1986.

[120] A. Armin, M. Hambsch, I. K. Kim, P. L. Burn, P. Meredith, and E. B. Namdas, "Thick junction broadband organic photodiodes," *Laser Photon. Rev.*, vol. 8, no. 6, pp. 924-932, Nov. 2014.

[121] A. Armin, R. D. Jansen-van Vuuren, N. Kopidakis, P. L. Burn, and P. Meredith, "Narrowband light detection via internal quantum efficiency manipulation of organic photodiodes," *Nat. Commun.*, vol. 6, pp. 6343-1--6343-8, Feb. 2015.

[122] V. Pecunia, "Efficiency and spectral performance of narrowband organic and perovskite photodetectors: a cross-sectional review," *J. Phys-Mater.*, vol. 2, no. 4, pp. 042001-1--042001-36, Oct. 2019.

[123] J. Vanderspikken, W. Maes, and K. Vandewal, "Wavelength-Selective Organic Photodetectors," *Adv. Funct. Mater.*, 2021, Art. no. 2104060.